# Numerical modelling of stresses and deformation in Zagros-Iranian plateau region

Srishti Singh[1] and Radheshyam Yadav[2]

[1]National Geophysical Research Institute
[2]CSIR-National Geophysical Research Institute

December 13, 2022

## Abstract

Zagros Orogeny System resulted due to collision of the Arabian with Eurasia. The region has the ocean-continent subduction and continent-continent collision; and convergence velocity shows variation from east to west. Therefore, this region shows the complex tectonic stress and a wide range of diffuse or localized deformation between both plates. The in-situ stress and GPS data are very limited in this region, therefore, we performed a numerical simulation of the stresses causing deformation in the Zagros-Iran region. The deviatoric stresses resulting from the variations in lithospheric density and thickness; and those from shear tractions at the base of lithosphere due to mantle convection were computed using thin-sheet approximation. Surface observations of strain rates, SHmax, plate velocities etc. are explained using the joint models of lithosphere and mantle, suggesting a good coupling between lithosphere and mantle in most parts of Zagros and Iran. However, the deformation in east of Iran is caused primarily by lithospheric stresses. Plate motion of Arabian plate is found to vary along the Zagros belt from north-northeast in south-east of Zagros, north in central Zagros to slight northwest in northwestern Zagros. The output of this study can be used in seismic hazards estimations.

## Hosted file

951506_0_supp_10509334_rmmmvz.docx available at https://authorea.com/users/565840/articles/612713-numerical-modelling-of-stresses-and-deformation-in-zagros-iranian-plateau-region

# Supporting Information for "Numerical modelling of stresses and deformation in Zagros-Iranian plateau region"

Srishti Singh[1], Radheshyam Yadav[1]

[1]CSIR-National Geophysical Research Institute, Hyderabad, India-500007

**Contents of this file**

1. Figures S1 to S2
2. Tables S1

**Additional Supporting Information (Files uploaded separately)**

1. Figure S1: (Left Panel) GPS (blue) and predicted (red) plate velocities with respect to a fixed Eurasian plate. Right Panel shows plot of FPDs in red and $SH_{max}$ in blue.

2. Figure S2: Plot of lithospheric viscosity in the study region that is used in finite element models.

3. Tables S1: Summary of quantitative comparison of predicted results of various models with observed data.

---

December 6, 2022, 4:25pm

# Numerical modelling of stresses and deformation in Zagros-Iranian plateau region

Srishti Singh[1] and Radheshyam Yadav[1]

[1]*CSIR-National Geophysical Research Institute, Hyderabad, India-500007*

## Key Points

- We have computed stresses and deformation of Zagros-Iran region with finite element modelling.
- Lithospheric stresses play an important role in the east of Iran.
- The joint models of lithosphere and mantle convection are able to explain various deformation indicators in the study area.

**Abstract**

Zagros Orogeny System resulted due to collision of the Arabian with Eurasia. The region has the ocean-continent subduction and continent-continent collision; and convergence velocity shows variation from east to west. Therefore, this region shows the complex tectonic stress and a wide range of diffuse or localized deformation between both plates. The in-situ stress and GPS data are very limited in this region, therefore, we performed a numerical simulation of the stresses causing deformation in the Zagros-Iran region. The deviatoric stresses resulting from the variations in lithospheric density and thickness; and those from shear tractions at the base of lithosphere due to mantle convection were computed using thin-sheet approximation. Surface observations of strain rates, $SH_{max}$, plate velocities etc. are explained using the joint models of lithosphere and mantle, suggesting a good coupling between lithosphere and mantle in most parts of Zagros and Iran. However, the deformation in east of Iran is caused primarily by lithospheric stresses. Plate motion of Arabian plate is found to vary along the Zagros belt from north-northeast in south-east of Zagros, north in central Zagros to slight northwest in northwestern Zagros. The out put of this study can be used in seismic hazards estimations.

***Keywords-*** Stress field, Gravitational Potential Energy, Mantle convection, Zagros, collision

# Plain Language Summary

We used numerical models to study the stresses causing deformation in the Zagros-Iran region. The stresses are generated due to variations in the density and topography of the lithosphere, which were computed through Gravitational potential energy (GPE) difference. Mantle convection produces shear tractions that are also an important source of stresses causing deformation. Different models of crustal structure and density of lithosphere give varying GPE, thus leading to different interpretations of the type of deformation in the study area. On the other hand, all mantle convection models in our study predicted consistent deviatoric stresses and were able to explain most observations of $SH_{max}$, plate velocities, and strain rates. Despite this, the lithosphere plays an important role in driving deformation, especially in the east of Iran. Overall, the lithospheric stresses when combined with those from mantle convection gave the best fit to the observed data.

# 1 Introduction

Zagros mountains are a part of Alpine-Himalayan belts that originated due to Arabian plate colliding with southern boundary of Eurasia. This collision resulted in closing of the Neotethys Ocean. The Zagros mountains extend from the eastern part of the Anatolia for over 1500 km in the NW-SE direction till the Makran subduction zone, showing large-scale diffuse deformation. Though there has been an increase in the influx of various studies trying to constrain the active deformation and kinematics of Zagros orogen (Allen et al., 2011; Reilinger et al., 2010; Le Dortz et al., 2009; Vernant et al., 2004; Walker, 2006), there are debates about various processes in this region, e.g. the timing of collision. Various authors (Jolivet & Faccenna, 2000; Agard et al., 2005; Vincent et al., 2005; Ballato et al., 2011) have suggested that collision onset time to be in Late Eocene to Oligocene; however, Ghalamghash et al. (2009); Mazhari et al. (2009) have argued Late Palaeocene or Early Eocene for the onset of collision. The Zagros and its foreland area have a great source of natural resources like petroleum. The study area consists of the ocean-continent subduction as well as the continental collisions. The convergence rate of the Arabian plate relative to the Eurasia varies from east to west. These complex structures and convergence velocity variation made the variable tectonic stress and deformation. The geophysical, geological and geodesy studies show that these areas are seismic active based on the earthquake data, fault slip rates and GPS velocities, which is related to the complex stress field in this region. Therefore, the world stress map (WSM) provides in-situ stress measurement and the compilation from the focal mechanism, hydrofracturing, and borehole breakout. However, the in-situ stress (WSM) and GPS velocity data (ArRajehi et al., 2010; Bayer et al., 2006; Frohling & Szeliga, 2016; Khorrami et al., 2019; Masson et al., 2006, 2007; Raeesi et al., 2017; Reilinger & McClusky, 2011; Vernant et al., 2004) are

very limited and sparsely distributed in this region; therefore, there is need for a numerical simulation study to comprehend the knowledge.

Although numerical modelling of tectonic stress and deformation was conducted in two approaches (1) using 2D and 3D geometrical structure, plate boundary forces like ridge push, slab pull and continents collision forces and rheological properties like Young's modulus, Poisson's ratio, viscosity, density etc. (Dyksterhuis & Müller, 2008; Coblentz et al., 1994; Koptev & Ershov, 2010; Richardson et al., 1976; Yadav & Tiwari, 2018), and, (2) considering Gravitational Potential energy and shear tractions from mantle convection with thin sheet approximation (Bird, 1998; Lithgow-Bertelloni & Guynn, 2004; Flesch et al., 2001; Ghosh & Holt, 2012; Singh & Ghosh, 2020). Stress studies showed that it's classified by the first, second and third order on the spatial scale (Zoback, 1992; Heidbach et al., 2007). The first-order stresses are originated due to the plate boundaries force like ridge push, slab pull and continental collisional; and second order stress by the rifting, isostasy and deglaciation. Moreover, third-order stress are caused by local sources like interaction faults systems, topography and density heterogeneity.

There are numerical studies conducted for tectonic stresses and deformation in Zagro-Iranian region (Austermann & Iaffaldano, 2013; Md & Ryuichi, 2010; François et al., 2014; Khodaverdian et al., 2015; Vernant & Chéry, 2006; Yamato et al., 2011). Md & Ryuichi (2010) modelled the maximum horizontal compressive stress ($SH_{max}$) orientations and showed N-S/NNE-SSW oriented $SH_{max}$ in Lurestan and eastern Zagros Simple Folded Belt, whereas they were aligned in NW-SE directions around Main Recent fault (MRF) and in northern High Zagros Faults (HZF). Sobouti & Arkani-Hamed (1996) reproduced observed faulting patterns by considering highly rigid central Iran and South Caspian Sea using a viscous thin-sheet approximation. Further, the kinematic model by Khodaverdian et al. (2015) procided constraints on fault slip rates, plate velocities and seismicity of the Iranian Plateau. The previous models did not include the mantle convections derived shear tractions for computation of deformation and stress in the Zagros-Iran regions.

In this study, we investigate the stress and deformation in Zagros-Iranian Plateau region to constrain the forces acting in this region with gravitational potential energy (GPE) and shear traction of mantle tractions. We will use a thin viscous sheet model based on Flesch et al. (2001) to compute various deformation parameters such as deviatoric stresses, strain rates, most compressive principal stress (SHmax), and plate velocities within the Zagros-Iran region.

# 2 Tectonic and Geology

The rise of Zagros mountain belt is a direct consequence of continental collision between Arabia and Eurasia. Zagros are located at the northeastern margin of the Arabian plate, trending in southwest

direction (Figure 1). It is bounded by the Main Zagros thrust (MZT) in northeast, while it joins the Tauras mountains in southern Turkey in the northwest. In the southeast, N-S trending Minab-Zandan fault zone separates Zagros from the Makran range. Outer Zagros are the young folded mountains in the southwest parts of the orogeny (Falcon, 1974; Sattarzadeh et al., 2002). High Zagros fault (HZF) separates highly deformed metamorphic rocks of inner Zagros from Simply folded mountains of outer Zagros (Hatzfeld & Molnar, 2010; Hatzfeld et al., 2010). Inner Zagros are bounded by MZT in northeast and are dominated by thrust faulting, possibly due to compression during the Late Cretaceous (Alavi, 1980). The northwestern Zagros are separated from central Zagros by a north-south trending strike-slip zone of deformation, known as Kazerun Fault System (KFS) (Authemayou et al., 2005).

Zagros mountains were formed between 35 and 23 Ma due to the convergence of Arabian platform beneath central Iranian crust. Arabian plate moves towards Eurasia with a plate velocity of 22-35 mm/yr (DeMets et al., 1990; McClusky et al., 2000; Jackson et al., 2002; Reilinger et al., 2006) in N-S to NNE direction. Zagros muntain belt is also accompanied by a zone of widespread deformation in the form of the high plateaus of Iran. Numerous earthquakes occur in these high terrains due to sustained tectonic activities; hence, these areas are prone to large seismic hazards.

During the last few decades, various geophysical surveys (receiver functions, deep seismic, GPS and tomographic studies) have been carried out in the Zagros-Iran region to investigate the deformation in this region. The southeastern Zagros accomodate the convergence between Arabia and Eurasia by pure shortening occuring through high-angle ($30^\circ - 60^\circ$) reverse faults that are prependicular to the belt (Hessami et al., 2006; Irandoust et al., 2022; Walpersdorf et al., 2006). On the other hand, oblique convergence in central and northern Zagros is partitioned into a strike-slip component that is accomodated on MRF and shortening occuring across the belt (Jackson et al., 2002; Talebian & Jackson, 2002). Zagros is separated from Makran subduction zone (MSZ) by Minab-Zendan-Palami (MZP) fault ($54^\circ - 58^\circ E$), which is a right-lateral strike-slip fault (Bayer et al., 2006). East of MZP shows significant shortening that is accomodated through the subduction in MSZ. Due to the difference between convergence rates, a shearing occurs in eastern Iran which is accomodated by the N-S trending faults bounding the Lut block. In northern Iran, fold and thrust belt of Alborz accomodates a quarter of Arabia-Eurasia convergence Irandoust et al. (2022). The oblique convergence in eastern Alborz is also partitioned into shortening at the southern boundary and a left-lateral component across the mountain belt (Irandoust et al., 2022; Khorrami et al., 2019; Tatar & Hatzfeld, 2009). Alborz mountains extend into Talesh in west which show thrust faulting on nearly flat faults. Kopeh-Dagh range in northeast accomodates the Arabia-Eurasia convergence through N-S shortening on major thrust faults in south.

# 3 Modelling

## 3.1 Equations

To model the stresses causing deformation in the Zagros-Iranian plateau due to Arabia-Eurasia collision, we solve three-dimensional (3D) force balance equations, considering the thin sheet approximation.

$$\frac{\partial \sigma_{ij}}{\partial x_j} + \rho g_i = 0 \tag{1}$$

Here $\sigma_{ij}$, $x_j$, $\rho$, and $g_i$ indicate the $ij^{th}$ component of the total stress tensor, $j^{th}$ coordinate axis, density and acceleration due to gravity respectively (England & Molnar, 1997; Ghosh et al., 2013b).

In the above equation, total stress, $\sigma_{ij}$ is substituted by deviatoric stress using the following relation:

$$\tau_{ij} = \sigma_{ij} - \frac{1}{3}\sigma_{kk}\delta_{ij} \tag{2}$$

In the above equation, the Kronecker delta and mean stress are denoted by $\delta_{ij}$ and $\frac{1}{3}\sigma_{kk}$ respectively. The force balance equation (1) is integrated up to the base of lithospheric sheet (L), resulting in following full horizontal force balance equations:

$$\frac{\partial \overline{\tau}_{xx}}{\partial x} - \frac{\partial \overline{\tau}_{zz}}{\partial x} + \frac{\partial \overline{\tau}_{xy}}{\partial y} = -\frac{\partial \overline{\sigma}_{zz}}{\partial x} + \tau_{xz}(L) \tag{3}$$

$$\frac{\partial \overline{\tau}_{yx}}{\partial x} + \frac{\partial \overline{\tau}_{yy}}{\partial y} - \frac{\partial \overline{\tau}_{zz}}{\partial y} = -\frac{\partial \overline{\sigma}_{zz}}{\partial y} + \tau_{yz}(L) \tag{4}$$

In equation (3) and (4), the over bars indicate integration over depth. Both equations (3 and 4) contain the first term representing horizontal gradients of GPE per unit area in right hand side. On the other hand, the shear tractions at the lithosphere base ($L$) arising due to mantle convection are denoted by $\tau_{xz}(L)$ and $\tau_{yz}(L)$ (Ghosh et al., 2009).

Both of the force balance equations (3 & 4) were solved using finite element technique (Flesch et al., 2001; Ghosh et al., 2009, 2013b; Singh & Ghosh, 2019, 2020). After solving these equations, we obtained the horizontal deviatoric stresses, $SH_{max}$, strain rates as well as plate velocities and compared them with observations.

The quantitative comparison between predicted and observed $SH_{max}$ axes (Figure 3a) was performed by computing the misfit given by $sin\theta(1+R)$ (Ghosh et al., 2013a; Singh & Ghosh, 2019, 2020), where R represents the quantitative difference between stress regimes of observed and predicted $SH_{max}$, while $\theta$ denotes the angular difference between both. Hence, this misfit accounts for both the angular and regime misfits with values lying between 0 and 3.

The correlation between predicted deviatoric stresses and GSRM strain rates (Figure 3b) (Flesch et al., 2007; Ghosh et al., 2013b; Singh & Ghosh, 2019, 2020) is given by following equation:

$$-1 \leq \sum_{areas} (\varepsilon.\tau)\Delta S / \left( \sqrt{\sum_{areas} (E^2)\Delta S} * \sqrt{\sum_{areas} (T^2)\Delta S} \right) \leq 1 \quad (5)$$

where $E = \sqrt{\dot{\varepsilon}_{\phi\phi}^2 + \dot{\varepsilon}_{\theta\theta}^2 + \dot{\varepsilon}_{rr}^2 + \dot{\varepsilon}_{\phi\theta}^2 + \dot{\varepsilon}_{\theta\phi}^2} = \sqrt{2\dot{\varepsilon}_{\phi\phi}^2 + 2\dot{\varepsilon}_{\phi\phi}\dot{\varepsilon}_{\theta\theta} + 2\dot{\varepsilon}_{\theta\theta}^2 + 2\dot{\varepsilon}_{\phi\theta}^2}$, $T = \sqrt{\tau_{\phi\phi}^2 + \tau_{\theta\theta}^2 + \tau_{rr}^2 + \tau_{\phi\theta}^2 + \tau_{\theta\phi}^2} = \sqrt{2\tau_{\phi\phi}^2 + 2\tau_{\phi\phi}\tau_{\theta\theta} + 2\tau_{\theta\theta}^2 + 2\tau_{\phi\theta}^2}$, and $\varepsilon.\tau = 2\dot{\varepsilon}_{\phi\phi}\tau_{\phi\phi} + \dot{\varepsilon}_{\phi\phi}\tau_{\theta\theta} + \dot{\varepsilon}_{\theta\theta}\tau_{\phi\phi} + 2\dot{\varepsilon}_{\theta\theta}\tau_{\theta\theta} + 2\dot{\varepsilon}_{\phi\theta}\tau_{\phi\theta}$. In the above equation, the second invariants of the strain rate and stress tensors are denoted by $E$ and $T$. GSRM strain rates, area and predicted deviatoric stresses are represented by $\dot{\varepsilon}_{ij}$, $\Delta S$, and $\tau_{ij}$ respectively. To constrain the plate valocities, we compute RMS as well as angular misfit between observed and predicted plate velcoities.

## 3.2 Crustal Models

In the right hand side of equations (3 & 4), the first term represents the vertically integrated vertical stress. It is computed and integrated from the top of variable topography up to depth L (100 km) (England & Molnar, 1997; Flesch et al., 2001; Ghosh et al., 2013b; Singh & Ghosh, 2019, 2020) using following relation:

$$\overline{\sigma}_{zz} = -\int_{-h}^{L} \left[ \int_{-h}^{z} \rho(z') g dz' \right] dz = -\int_{-h}^{L} (L - z)\rho(z) g dz \quad (6)$$

where $\rho(z)$, $L$ and $h$ denote density, the depth to the lithosphere base (100 km) and topographic elevation respectively. $z$ & $z'$ are variables of integration and $g$ represents the acceleration due to gravity.

The right hand side of equation 6 is given by negative of GPE per unit area. To calculate GPE and the stresses associated with it, we used three different global crustal models, CRUST2.0, CRUST1.0 and LITHO1.0. The upper crust thickness lies within 15-20 km in the Zagros-Iran region for CRUST2 model (Figure 2a). However, the thickness of the upper crust in the Zagros-Iranian region is much higher for CRUST1 and LITHO ($>$ 25 km) (Figure 2b & c). The Zagros-Iran region has a thicker middle crust ($>$ 20 km) in case of both CRUST2 and LITHO models (Figure 2d & f), while CRUST1 shows a much thinner middle crust ($<$ 12 km) in this region (Figure 2e). The lower crust in the Zagros-Iran region is found to be very thin ($<$ 10 km) for all three models (Figure 2g-i).

The density variations in the study area are minimal for CRUST2 model. CRUST2 also shows the highest average density in all three layers ($>$2.7 $g/cm^3$) (Figure 2j,m,p). CRUST1 also indicates an average density of $\sim 2.72/cm^3$ in the Zagros-Iran region for the upper crust (Figure 2k). The middle and lower crustal layers of CRUST1 show average densities of $2.80 g/cm^3$ and $\sim 2.85 g/cm^3$, respectively (Figure 2n,q). LITHO model shows the lowest average density in the study area for all three layers

(Figure 2l,o,r). The upper crust of LITHO models shows an average density of $2.65 g/cm^3$. Central Iran block has relatively denser upper crust ($\sim 2.75 g/cm^3$), while the density decreases to $\sim 2.62 - 2.64 g/cm^3$ near Zagros region. Similar patterns of density variations are observed in the middle and lower crust of LITHO model ((Figure 2o,r). Such differences in thickness and density data lead to varying GPE values, and hence subsequently, different stresses.

## 3.3 Mantle Convection

We ran mantle convection models using HC (Hager & O'Connell, 1981). HC is a semi-analytical mantle convection code that uses density anomalies derived from seismic tomography models and radial viscosity as inputs. Here, we considered four global mantle convection models, S40RTS (Ritsema et al., 2011), SAW642AN (Mégnin & Romanowicz, 2000), 3D2018_S40RTS and S2.9_S362 to infer the mantle density anomalies. 3D2018_S40RTS is a merged model of SV wave upper mantle tomography model, 3D2018_Sv given by Debayle et al. (2016), and S40RTS. S2.9 is a global tomography model of upper mantle with higher resolution which is given by Kustowski et al. (2008b). We merged this model with the global shear wave velocity model, S362ANI (Kustowski et al., 2008a) to obtain merged tomography model of S2.9_S362. The radial viscosity model, GHW13 which is the best viscosity structure given by Ghosh et al. (2013b) was used in our study to run mantle convection models.

## 3.4 Data

To have better constraints on our models, we also estimated $SH_{max}$(most compressive horizontal principal axes) orientations as well as plate velocities. Various deformation indicators such as $SH_{max}$ orientations from the World Stress Map (WSM) (Heidbach et al., 2016), strain rates and plate velocities from Global Strain Rate Model (Kreemer et al., 2014) were used to perform a quatitative comparison with our predicted results (Figure 3).

WSM data is a global database of the crustal stress field obtained from various sources such as focal mechanism; geophysical logs of borehole breakouts and drilled induced fractures; engineering methods such as hydraulic fractures and overcoring; and geological indicators that are obtained from fault slip analysis and volcanic alignments. These data have been assigned quality ranks from A to E based on the accuracy range. A-type data suggests that the standard deviations of $SH_{max}$ orientations are within $\pm 15^\circ$ range, $\pm 20^\circ$ for B-type, $\pm 25^\circ$ for C-type and $\pm 40^\circ$ for D-type. However, E-type indicates the data records are either incomplete or from non-reliable sources or the accuracy is $> \pm 40^\circ$. Our study uses A-C quality stress data records (Figure 3a). Observed $SH_{max}$ axes are aligned in NNE-SSW directions in Zagros with dominant thrust faulting. NW and Central Iran shows some strike-slip mode of deformation

with NE-SW compressional directions.

The strain rates and plate velocities are taken from GSRM v2.1 model (Kreemer et al., 2014) (Figure 3b). GSRM v2.1 provides a global data set of strain rates and plate motions that are determined using $\sim 22,500$ geodetic plate velocities. Higher strain rates are observed along simple folded mountains ($\sim 40-100\times10^{-9}/yr$). Most of Iran shows strain rates in between $4-10\times10^{-9}/yr$. The plate motions used in our study for comparing with predicted velocities are given in a no-net-rotation (NNR) frame interpolated on a $1^{\circ}\times1^{\circ}$ grid. The velocity vectors show an eastward motion in the study area, which becomes nearly E-W in Afghan Block (Figure 3b).

# 4 Results

## 4.1 Stress and deformation due to GPE

Three crustal models (CRUST1.0, CRUST2.0 and LITHO1.0) were used to compute GPE within the study region. The second invariant of stress computed using GPE lies within $\sim$10-12 MPa along the Zagros for CRUST2 and CRUST1 models (Figure 4a,c). LITHO model predicts larger stress magnitudes along Zagros (Figure 4e). NE-SW compressional stresses are observed along the frontal faults of Zagros (MFF) (Figure 1a,c). The central part of Zagros thrust faults (MZT) shows the strike-slip mode of faulting for nearly all three models (Figure 4 & 4b,d & f). The strike-slip regime further extends into Sanandaj-Sirjan Zone (SSZ) while lies north of MZT for CRUST2 and LITHO model (Figure 4b,f), while it transitions to thrust type of deformation in the north of MZT for CRUST1 (Figure 4d). The Urmia-Dokhtar Magmatic Arc (UDMA) and central Iran also show strike-slip mode of faulting for CRUST2 and LITHO. The north of MRF shows tension for CRUST2 model, while CRUST1 predicts this area to be predominantly strike-slip. On the other hand, the entire region shows significant compression for LITHO model.

We compared predicted $SH_{max}$ from our three GPE only models to observed $SH_{max}$ orientations and type obtained from WSM (Heidbach et al., 2016) by computing Regime misfit (Figure 5, left panel). The average misfit is lowest for LITHO model with a value of 0.59 (Figure 5g), while CRUST2 model shows the highest average misfit of 0.77 (Figure 5a). High misfits ($2-3$) are observed in North of MRF and Tehran for CRUST2, while lowest ($<1$) in case of LITHO, suggesting that the dominant mode of faulting in this area is possibly thrust as opposed to normal deformation predicted by CRUST2. In central Iran, $SH_{max}$ misfit is low ($<1$) when the dominant mode of deformation is strike-slip as predicted LITHO model.

On calculating the correlation between the predicted deviatoric stresses and GSRM strain rates, the LITHO model shows the highest average correlation (0.92) (Figure 5, middle panel). The correlation

is found to be extremely poor ($\sim -1$) for CRUST2 model in the north of MRF (Figure 5b). Such poor correlation suggests that the predicted stresses differ entirely from those causing deformation. For example, anti-correlation in north of MRF suggests that the dominant mode of deformation in this area might be thrust rather than normal faulting. Again, the correlation coefficient is less than 0.2 in the central Iranian Block for CRUST2 and CRUST1 models (Figure 5b,e), while LITHO model shows a better correlation suggesting the strike-slip type of deformation to be more prominent in central Iran (Figure 5h).

We predicted the plate velocities for all three models in the NNR frame and compared them with observed plate velocities obtained from Kreemer et al. (2014) (Figure 5 right panel). CRUST2 gives the least RMS error (7.32 mm/yr) and lowest angular misfit (5.5°) (Figure 5c). LITHO model shows high misfits ($> 20°$) between observed and predicted velocities in the east of the central Iran (i.e. Afghan Block)(Figure 5i). Both CRUST2 and LITHO models predict the plate velocities very close to observed ones in the Zagros mountains, as shown by nearly zero angular misfits along Zagros (Figure 5c & i). CRUST1 performs average in predicting the plate velocities in the study area (Figure 5f).

## 4.2 Stress and deformation due to Mantle Convection

The deviatoric stresses predicted using all four mantle convection models are found to be mostly compressonal along MFF (Figure 6). All models, except for SAW642AN, predict the strike-slip mode of faulting in NW parts of Zagros with nearly E-W oriented extensional axes and N-S compressional axes (Figure 6a,e & g). On the other hand, SAW642AN shows predominant compression within this area (Figure 6e). S40RTS, 3D2018_Sv, and S2.9_S362 show strike-slip deformation in NW parts of SSZ, UDMA and NW Iran. Central Iran is predicted to have mostly compressional stresses by all models except for S40RTS. Thrust type of deformation is predicted in Afghan Block by all models with some intermittent strike-slip deformation. SINGH_SAW model predicts the whole Afghan Block in the strike-slip regime (Figure 6g-h). S40RTS and S2.9_S362 predict higher stress magnitude in NW parts of the Zagros Orogeny system and Central Iran compared to other models.

The misfit between observed and predicted $SH_{max}$ is found to be much lower for mantle convection models (0.54-0.57) (Figure 7 left panel), than those of GPE only models (Figure 5 left panel), evidently showing the importance of mantle flow. The lowest average misfit is observed for SAW642AN (0.54) (Figure 7d). Though the misfit increases in the east, Lut block and, near MSZ. The correlation of predicted deviatoric stresses with GSRM strain rates improves over GPE only models (Figure 7 middle panel), with SAW642AN yielding the highest correlation coefficient (0.91) (Figure 7e). Correlation drops below 0.4 parts of central Iran. S40RTS performs predicts the plate velocities closest to observed one, out of all models, with the least RMS error ( 6.20 mm/yr) between predicted and observed plate

velocities (Figure 7c). On the other hand, SAW642AN and 3D2018_S40RTS models show high misfits (rms error $\sim 10 mm/yr$), as they are unable to match observed plate velocities in Zagros-Iran plateau, both in orientations and magnitude (Figures 7f & i).

As discussed above, mantle convection models perform better in predicting deviatoric stresses in the study area. However, the error in predicting plate velocities is higher than in GPE only models. GPE only models perform slightly better in predicting the orientation and magnitude of velocity vectors. Thus, we add the deviatoric stresses predicted from GPE differences and Mantle convection models to constrain the stress field in Zagros-Iranian plateau that may account for both forces.

## 4.3 Stress and deformation by GPE and Mantle convection

Adding mantle contributions to GPE only models led to significant changes in total deviatoric stresses for all models (Figure 8,9,10). There is a significant increase in total stress magnitude of the entire study area; except for north of MRF and SE of central Iran, which show slightly lower stresses ($<$ 16 MPa) for combined models of CRUST2 and mantle convection (Figure 8). These models show predominant compression in most of Zagros, SSZ, UDMA, NW and central Iran, except for the strike-slip type of deformation in NW parts. The joint models of CRUST1 and mantle convection predict higher stresses ($>$ 25 MPa) in NW Iran and at MFF (Figure 9). Interestingly, the stresses drop below 20 MPa towards the north of HZF, MRF till the south Capsian. The combined models of CRUST1 and mantle convection show compressional stresses are dominant in the study area, with occasional strike-slip faulting in the north-west (Figure 9 right panel). The stresses predicted by combined models of LITHO and mantle convection models are higher in magnitude than other models in the study area ($>$ 25 MPa) (Figure 10). S40RTS+litho and S2.9_S362+litho models show high stresses in Zagros ($>$50 MPa)(Figure 10a,g).

The combined models show a lower misfit between observed and predicted $SH_{max}$ (Figure 11), especially when compared to GPE only models (Figure 5 left panel). SAW642AN+litho showed the lowest average misfit of 0.47 (Figure 11f). Interestingly, SAW642ANcr2 and 3D2018_S40RTScr2 show low misfits in the Zagros-Iranian plateau region, despite not having the lowest average misfit (Figure 11d & g). The higher misfits in NW Iran and SE of the central Iran block observed for GPE only models, get reduced significantly due to the addition of mantle derived stresses, referring to the importance of mantle convection in these areas.

As we look at the correlation between predicted stress tensors and GSRM strain rate tensors, the overall correlation is better for combined models (Figure 12), especially for combined models of LITHO and mantle convection (Figure 12 right panel). A high average correlation coefficient of 0.94 is observed for SAW642AN+litho, 3D2018_S40RTS+litho as well as S2.9_S362+litho (Figures 12f, i & l). Despite an overall improvement in correlation between observed strain tensors and predicted deviatoric stresses,

the correlation is found to be much poor in areas such as NW parts of Zagros and east of central Iranian block, for combined models of mantle convection and GPE only models of CRUST2 & CRUST1 (Figure 12 left and middle panels). In NW Zagros, mantle only models are found to perform much better, as they show better correlation (Figure 7 middle panel), thus suggesting mantle derived stresses are needed to be much higher than those from GPE to explain the observed deformation in these areas.

Again the combined models of GPE and mantle tractions give lower rms errors, when predicted plate velocities are compared to the observed ones. S40RTScr2 shows least rms error (3.28 mm/yr) and least average angular misfit (3.0°) between predicted and observed plate velocities (Figure 13a). Relatively the combined models of S40RTS/S2.9_S362 and GPE perform much better than other models in predicting the orientation and magnitudes of plate velocities. Significant misfits are observed for SAW642ANcr1 and 3D2018_S40RTScr1 models.

# 5 Discussion

The Zagros-Iranian plateau region is formed due to the convergence of Arabian plate towards Eurasia. Zagros mountain belt demarcates the southwestern boundary of the deformation zone, whereas, it is bounded by the Makran subduction zone in the southeast and by Afghan Block in the east. Kopet-Dagh and Arborz act as this region's northeastern and northern boundaries (Irandoust et al., 2022). We modeled the stresses and deformation parameters in the study area by solving the force balance equation using the finite element method for a global grid of $1^\circ \times 1^\circ$ resolutions, considering two primary sources of stresses; GPE and mantle tractions. GPE was calculated using the thickness and density variation from the different global models like CRUST1, CRUST2 and LITHO. The shear tractions were computed from density derived mantle convection model.

The magnitude of stresses due to GPE variations was below 15 MPa in the Iranian plateau for CRUST2 and CRUST1 models (Figure 4a & c). However, LITHO model predicted higher stresses ($> 30$ MPa) with predominant compression in parts of the Zagros-Iran region and Afghan block. Most of the convergence of Arabian and Eurasian plates has been accommodated through shortening across Zagros (Irandoust et al., 2022; Khodaverdian et al., 2015). Walpersdorf et al. (2006); Hessami et al. (2006) suggested nearly pure N-S shortening of $8 \pm 2 mm/yr$ in southeastern Zagros. The convergence occurs perpendicular to the Simply folded mountains and is restricted to the shore of Persian Gulf. Earthquake focal mechanisms also show reverse faulting within this area (Berberian, 1995; Hatzfeld et al., 2010; Hatzfeld & Molnar, 2010; Irandoust et al., 2022). In our study, LITHO model predicts thrust mode of faulting within Zagros, which is consistent with these results. In NW Zagros, Hatzfeld et al. (2010); Hatzfeld & Molnar (2010); Jackson & McKenzie (1984); Khorrami et al. (2019); Talebian & Jackson

(2002) and various others have suggested partitioning of deformation. The oblique shortening is partitioned into strike-slip faulting that is accommodated by MRF, while shortening occurs perpendicular to the the mountain belt (Hatzfeld et al., 2010; Hatzfeld & Molnar, 2010; Jackson & McKenzie, 1984; Khorrami et al., 2019; Talebian & Jackson, 2002). On considering lithospheric models only, we predicted normal mode of faulting to be dominant in this area for CRUST2. On the other hand, CRUST1 model predicted strike-slip components in the northern segment of MRF, while LITHO showed thrust type of deformation in this area. Interestingly, the misfits of predicted parameters with various observations of $SH_{max}$, strain rates and plate velocities were found to be lowest for LITHO model, thus arguing for thrust type of deformation in this area. SSZ in north of MZT consists of various thrust systems (Alavi, 1994). CRUST1 predicts thrust mode of faulting in this region, while CRUST2 and LITHO models show intermittent strike-slip type of faulting. Alborz as well as Kopet Dagh in north has also been subjected to reverse faulting (Allen et al., 2003; Hatzfeld & Molnar, 2010; Hollingsworth et al., 2010; Irandoust et al., 2022; Khodaverdian et al., 2015), which has also been shown by CRUST1 and LITHO models. Models predicting thrust in Talesh mountains show low misfits to observation suggesting thrusting of the mountain range over the basin with slip vectors directed towards the South Caspian Sea (Irandoust et al., 2022). The N-S convergence in Kopeh-Dagh range is predicted by LITHO model considering contribution from lithospheric density and topographic variations only. The shearing between Central Iran and Afghan Block caused due to varying rates of shortening across the Zagros, Alborz and Caucasus, is accommodated by strike-slip faults near Lut block boundaries (Khorrami et al., 2019; Vernant et al., 2004; Walpersdorf et al., 2014). Again, LITHO model predicted similar strike-slip deformation in these areas; however, CRUST2 and CRUST1 failed to do so.

The stresses predicted using basal tractions were mostly compressional in southeastern Zagros owing to the convergence of Arabia-Eurasia (Figure 6). However, all models, except SAW642AN predicted strike-slip type of deformation in the northwestern Zagros (MRF), which concurs with the results from various studies (Hatzfeld et al., 2010; Hatzfeld & Molnar, 2010; Jackson & McKenzie, 1984; Khorrami et al., 2019; Talebian & Jackson, 2002). The mantle derived stress parameters showed a better fit to observables than those from GPE variations (Figures 7 left and middle panel), though the correlation dropped below 0.5 in Central Iran. Here, mantle convection models predicted compressional type of deformation, while Baniadam et al. (2019); Khorrami et al. (2019) suggested that strike-slip faulting along the fault system bounding Lut Block. The velocity misfits were very high for all models except S40RTS (Figure 7 right panel). Although we used four tomography models to compute the mantle-derived stresses, the stress regimes for all models are found to be similar, with varying magnitudes. Such results suggest that nearly all four seismic tomography models are relatively consistent in predicting the stresses in this region.

Adding the GPE derived stresses to those from mantle to obtain the total lithospheric stress field showed a notable improvement in constraining the observed deformation parameters. The final stress regimes also varied significantly depending on particular combinations of GPE and mantle convection models. All joint models of CRUST2 and mantle tractions showed lower magnitudes of stresses ($< 15$ MPa) in north of MRF, Tehran and southern Lut block. The stresses showed an obvious increase in these areas for other models. Significantly higher stresses ($> 30$ MPa) were also observed near the collisional front (MFF) for all models. On comparing with observations, combined models of CRUST2 and mantle tractions showed significant improvement in fit, except in areas north of MRF and Tehran. CRUST1 model when added with mantle contribution, predicted thrust faulting along the faults bounding Lut Block, leading to poor correlation ($< 0.5$). On the other hand, combined LITHO and mantle convection models gave a much better fit in this area, as they predicted strike-slip faulting. The use of different mantle convection models is much less sensitive in the Iran-Zagros region, as most models can match various surface observables reasonably well.

On running various models and comparing the stresses in Zagros-Iran, we try to explain the relative roles of GPE and mantle tractions in causing observed deformation. The contributions from both sources vary significantly among different models. However, these variations arise mainly from GPE only models, which may be due to uncertainties in crustal models of this area. Another interesting observation from this study is that the role of GPE in the study region may not be that significant, as mantle derived stresses were able to explain many of the deformation indicators. To get a quantitative constraint on the best model, we computed a total error as given below:

$$Total\,error = SH_{max}\,error + 1 - C_{strain} + V_{rms} \tag{7}$$

$SH_{max}$ error in the above equation is calculated as mentioned in section 3.4, while $C_{strain}$ is the correlation computed using equation 6. $V_{rms}$ is the rms error between predicted and observed velocities. The total errors calculated using equation 7 have been tabulated in Table S1. S40RTScr2 is found to have lowest error.

We also calculated plate velocities with respect to the Eurasian plate (Figure 14) and compared them with observed GPS velocities relative to Eurasia. The GPS velocities were obtained from various studies conducted in the study area (ArRajehi et al., 2010; Bayer et al., 2006; Frohling & Szeliga, 2016; Khorrami et al., 2019; Masson et al., 2006, 2007; Raeesi et al., 2017; Reilinger & McClusky, 2011; Vernant et al., 2004). GPS measurements show a northward convergence rate of $\sim 22 mm/yr$ for Arabia relative to Eurasia (Reilinger et al., 2006; Vernant et al., 2004), however, it varies significantly along the Zagros. The southeastern Zagros show the highest convergence rates of $\sim 25$ mm/yr oriented in

north-northeast directions. GPS vectors are oriented northward in Central Zagros, which transitions north-northwest in NW parts of Zagros with the lowest convergence rates of $\sim$ 18 mm/yr (Hatzfeld & Molnar, 2010; Hatzfeld et al., 2010; Khorrami et al., 2019). Vernant et al. (2004) suggested that MSZ accommodates most of the shortening ($19.5 \pm 2$ mm/yr) in the east of $58^{\circ}E$, while fold and thrust belts of Zagros, Alborz and Caucasus collectively accomodate the shortening in west of $58^{\circ}E$. GPS velocities in east of Iran (Afghan Block) are very small in magnitude. To the west, velocities increase showing westward rotation of Antolia Khorrami et al. (2019); Reilinger et al. (2006). The northern part of Iran shows that GPS vectors are aligned towards the northeast. We found that the combined model of S40RTS and CRUST2 can approximately match the GPS velocities (Figure 14a). Predicted plate velocities with respect to the fixed Eurasian plate show a northward movement of 2-3 cm/yr in southeastern Zagros. The plate moves in NNE direction east of central Zagros (53° E). On the other hand, west of 53° E shows a movement in NNW direction, becoming much more prominent in the north. However, the convergence rates in east of Iran i.e. Lut Block as well as Afghan Block, is predicted to be much higher ($\sim 1 - 2cm/yr$) than those suggested by various observations. Plate velocities predicted by joint models, S40RTScr1 and S40RTS+litho show nearly N-S contraction of of very high magnitudes (4-5 cm/yr) throughout the region (Figure S1), which suggests much higher rates of deformation than those suggested by above mentioned studies.

We also used shear wave splitting measurements to further study the deformation in the Zagros-Iran region by comparing them with $SH_{max}$ (Figure 14b). The fast polarization directions (FPDs) are the indicators of seismic anisotropy. We consider two primary causes of seismic anisotropy; induced by stress and due to structure of the region (Yang et al., 2018). If the FPDs are parallel to $SH_{max}$ orientations, it suggests that anisotropy is associated with stress. On the other hand, latter kind of anisotropy is related with the alignment of fault, fast axes of minerals that may cause polarization, and sedimentary bedding planes. The FPDs in our study were obtained from Sadeghi-Bagherabadi et al. (2018); Kaviani et al. (2009, 2021). The FPDs are subparallel to $SH_{max}$ orientations in NW Zagros, Arabian plate, northern Iran and MSZ. Such a correlation between both indicates that anisotropy in this region may be stress induced. In NW Zagros, Sadeghi-Bagherabadi et al. (2018) also showed FPDs parallel to the strike of the fault, suggesting seismic anisotropy mainly reflect the deformation in the lithospheric mantle. Again, FPDs are subparallel to the strike of range in northeastern Iran, eastern Kopeh Dagh and central Alborz indicating structure-induced anisotropy caused by strong shearing along the strike-slip faults (Gao et al., 2022; Kaviani et al., 2021).

To explore the relative roles of lithospheric and mantle derived stresses, we compared the deviatoric stresses from CRUST2 to those from S40RTS. We performed a correlation between both stresses by using equation 5 and found a high correlation ($> 0.5$) near MSZ and central Zagros (Figure 14c).

The correlation degrades north of the simply folded mountains and NW Iran. The stresses are anti-correlated in parts of northwestern parts of higher Zagros, north of MRF and Tehran, as CRUST2 predicted NNE-SSW tension (Figure 4b) as opposed to the strike-slip faulting predicted by S40RTS (Figure 6b). Lut Block also shows a slight anticorrelation between stresses ($\sim -0.5$), as the stresses predicted by CRUST2 are very low. The log of the ratio of second invariants of deviatoric stresses from GPE variations ($T_1$) to that of mantle tractions ($T_2$) is plotted in Figure 14d. Positive values of logarithmic ratio suggests the dominance of GPE derived stresses over mantle ones, as observed in the south of the collisional boundary (MFF). The ratio is negative in most parts of the Iranian plateau and Zagros, indicating that the magnitude of mantle derived stresses are higher than those from GPE, especially in higher Zagros and central Iran (Figure 14d).

# 6 Conclusion

The Zagros-Iranian plateau region has large deformations along and across the collision zones. Therefore, we conduct numerical simulation studies for stress and deformations. The stresses predicted in this region were primarily compressional, with magnitudes lower than 30 MPa. The southeastern boundary of Zagros to be under high stress which is also reflected by higher convergence rates. Mantle convection models are able to constrain most observations in Iranian plateau. However, the misfits with observations are much larger in east of Iran, when only mantle contributions are considered. The combined models of lithospheric and mantle-derived stresses can give a better fit to surface observables in most of the area, suggesting a good lithosphere-mantle coupling, except for east of Iran. The fit between both predicted and observed data increases after considering mantle derived stresses. The shearing in those areas is predicted by lithospheric models, though variation in lithospheric and density structure given by these models lead to varying degree of misfits. Hence, there is a need for better contraint on lithospheric structure in this area.

The mantle derived stresses were found to be much higher than lithospheric stresses, thus the overall stress regimes predicted by combined models were more biased towards the compressional type of stresses. This caused our combined models to predict thrust mode of faulting in most cases, especially when lithospheric derived stresses were computed from CRUST1 and LITHO models. CRUST2 model predicted more extensional stress in Iranian plateau, which in turn balanced the effect of compressional stresses predicted by mantle convection models; hence leading to prominance of strike-slip model of faulting northwestern parts of study region. The rate of convergence of Arbia relative to a fixed Eurasia was found to vary along the Zagros orogeny in a similar way to GPS measurements.

# Open Research Section

We used three models, namely CRUST1.0, CRUST2.0, and LITHO1.0, for obtaining the data of crustal and lithospheric structure, which are required as inputs in finite element models. We downloaded these three models and the seismic tomography models used in mantle convection codes from the Incorporated Research Institutions for Seismology (IRIS) Earth Model Collaboration repository (`http://ds.iris.edu/ds/products/emc-earthmodels/`). The strain rate model, GSRMv2.1 was obtained from `http://geodesy.unr.edu/GSRM/`. World Stress Map Website (`https://www.world-stress-map.org/`) provides the $SH_{max}$ orientations and type of faulting, which were used to perform a quantitative comparison with predicted results. GPS velocities relative to Eurasia were taken from ArRajehi et al. (2010); Bayer et al. (2006); Frohling & Szeliga (2016); Khorrami et al. (2019); Masson et al. (2006, 2007); Raeesi et al. (2017); Reilinger & McClusky (2011); Vernant et al. (2004). We also used seismic anisotropy data from Sadeghi-Bagherabadi et al. (2018); Kaviani et al. (2009, 2021).

# Acknowledgments

We are grateful to Dr. Attreyee Ghosh for sharing the codes for finite element modelling of stresses. We thank the director CSIR-NGRI for permission to publish this work (Ref. No. NGRI/Lib/2022/ Pub-110). This article is published as a part of MLP-FBR-003(AM) Project. The figures of this article are generated from gmt.

# References

Agard, P., Omrani, J., Jolivet, L., & Mouthereau, F. (2005). Convergence history across Zagros (Iran): constraints from collisional and earlier deformation. *International journal of earth sciences*, *94*(3), 401–419.

Alavi, M. (1980). Tectonostratigraphic evolution of the Zagrosides of Iran. *Geology*, *8*(3), 144–149.

Alavi, M. (1994). Tectonics of the Zagros orogenic belt of Iran: new data and interpretations. *Tectonophysics*, *229*(3-4), 211–238.

Allen, M., Ghassemi, M., Shahrabi, M., & Qorashi, M. (2003). Accommodation of late Cenozoic oblique shortening in the Alborz range, northern Iran. *Journal of structural geology*, *25*(5), 659–672.

Allen, M.B., Kheirkhah, M., Emami, M.H., & Jones, S.J. (2011). Right-lateral shear across Iran and

kinematic change in the Arabia—Eurasia collision zone. *Geophysical Journal International*, *184*(2), 555–574.

ArRajehi, A., McClusky, S., Reilinger, R., Daoud, M., Alchalbi, A., Ergintav, S., Gomez, F., Sholan, J., Bou-Rabee, F., Ogubazghi, G., et al. (2010). Geodetic constraints on present-day motion of the Arabian Plate: Implications for Red Sea and Gulf of Aden rifting. *Tectonics*, *29*(3).

Austermann, J. & Iaffaldano, G. (2013). The role of the Zagros orogeny in slowing down Arabia-Eurasia convergence since˜ 5 Ma. *Tectonics*, *32*(3), 351–363.

Authemayou, C., Bellier, O., Chardon, D., Malekzade, Z., & Abassi, M. (2005). Role of the Kazerun fault system in active deformation of the Zagros fold-and-thrust belt (Iran). *Comptes Rendus Geoscience*, *337*(5), 539–545.

Ballato, P., Uba, C.E., Landgraf, A., Strecker, M.R., Sudo, M., Stockli, D.F., Friedrich, A., & Tabatabaei, S.H. (2011). Arabia-Eurasia continental collision: Insights from late Tertiary foreland-basin evolution in the Alborz Mountains, northern Iran. *Bulletin*, *123*(1-2), 106–131.

Baniadam, F., Shabanian, E., & Bellier, O. (2019). The kinematics of the Dasht-e Bayaz earthquake fault during Pliocene-Quaternary: implications for the tectonics of eastern Central Iran. *Tectonophysics*, *772*, 228218.

Bayer, R., Chery, J., Tatar, M., Vernant, P., Abbassi, M., Masson, F., Nilforoushan, F., Doerflinger, E., Regard, V., & Bellier, O. (2006). Active deformation in Zagros—Makran transition zone inferred from GPS measurements. *Geophysical Journal International*, *165*(1), 373–381.

Berberian, M. (1995). Master "blind" thrust faults hidden under the Zagros folds: active basement tectonics and surface morphotectonics. *Tectonophysics*, *241*(3-4), 193–224.

Bird, P. (1998). Testing hypotheses on plate-driving mechanisms with global lithosphere models including topography, thermal structure, and faults. *Journal of Geophysical Research: Solid Earth*, *103*(B5), 10115–10129.

Coblentz, D., Richardson, R.M., & Sandiford, M. (1994). On the gravitational potential of the Earth's lithosphere. *Tectonics*, *13*(4), 929–945.

Debayle, E., Dubuffet, F., & Durand, S. (2016). An automatically updated S-wave model of the upper mantle and the depth extent of azimuthal anisotropy. *Geophysical Research Letters*, *43*(2), 674–682.

DeMets, C., Gordon, R.G., Argus, D., & Stein, S. (1990). Current plate motions. *Geophysical journal international*, *101*(2), 425–478.

Dyksterhuis, S. & Müller, R. (2008). Cause and evolution of intraplate orogeny in Australia. *Geology*, *36*(6), 495–498.

England, P. & Molnar, P. (1997). Active deformation of Asia: From kinematics to dynamics. *Science*, *278*(5338), 647–650.

Falcon, N.L. (1974). Southern Iran: Zagros Mountains. *Geological Society, London, Special Publications*, *4*(1), 199–211.

Flesch, L.M., Haines, A.J., & Holt, W.E. (2001). Dynamics of the India-Eurasia collision zone. *Journal of Geophysical Research*, *106*(B8), 16435–16460.

Flesch, L.M., Holt, W.E., Haines, A.J., Wen, L., & Shen-Tu, B. (2007). The dynamics of western North America: stress magnitudes and the relative role of gravitational potential energy, plate interaction at the boundary and basal tractions. *Geophysical Journal International*, *169*(3), 866–896.

François, T., Burov, E., Agard, P., & Meyer, B. (2014). Buildup of a dynamically supported orogenic plateau: Numerical modeling of the Zagros/Central Iran case study. *Geochemistry, Geophysics, Geosystems*, *15*(6), 2632–2654.

Frohling, E. & Szeliga, W. (2016). GPS constraints on interplate locking within the Makran subduction zone. *Geophysical Supplements to the Monthly Notices of the Royal Astronomical Society*, *205*(1), 67–76.

Gao, Y., Chen, L., Talebian, M., Wu, Z., Wang, X., Lan, H., Ai, Y., Jiang, M., Hou, G., Khatib, M.M., et al. (2022). Nature and structural heterogeneities of the lithosphere control the continental deformation in the northeastern and eastern Iranian plateau as revealed by shear-wave splitting observations. *Earth and Planetary Science Letters*, *578*, 117284.

Ghalamghash, J., Bouchez, J., Vosoughi-Abedini, M., & Nédélec, A. (2009). The Urumieh Plutonic Complex (NW Iran): Record of the geodynamic evolution of the Sanandaj–Sirjan zone during Cretaceous times–Part II: Magnetic fabrics and plate tectonic reconstruction. *Journal of Asian Earth Sciences*, *36*(4-5), 303–317.

Ghosh, A., Becker, T.W., & Humphreys, E.D. (2013a). Dynamics of the North American continent. *Geophysical Journal International*, *194*(2), 651–669.

Ghosh, A. & Holt, W.E. (2012). Plate motions and stresses from global dynamic models. *Science*, *335*(6070), 838–843.

Ghosh, A., Holt, W.E., & Flesch, L.M. (2009). Contribution of gravitational potential energy differences to the global stress field. *Geophysical Journal International*, *179*(2), 787–812.

Ghosh, A., Holt, W.E., & Wen, L. (2013b). Predicting the lithospheric stress field and plate motions by joint modeling of lithosphere and mantle dynamics. *Journal of Geophysical Research: Solid Earth*, *118*(1), 346–368.

Hager, B.H. & O'Connell, R.J. (1981). A simple global model of plate dynamics and mantle convection. *Journal of Geophysical Research*, *86*(B6), 4843–4867.

Hatzfeld, D., Authemayou, C., van der Beek, P., Bellier, O., Lavé, J., Oveisi, B., Tatar, M., Tavakoli, F., Walpersdorf, A., & Yamini-Fard, F. (2010). The kinematics of the Zagros mountains (Iran). *Geological Society, London, Special Publications*, *330*(1), 19–42.

Hatzfeld, D. & Molnar, P. (2010). Comparisons of the kinematics and deep structures of the Zagros and Himalaya and of the Iranian and Tibetan plateaus and geodynamic implications. *Reviews of Geophysics*, *48*(2).

Heidbach, O., Rajabi, M., Reiter, K., & Ziegler, M. (2016). WSM Team (2016): World Stress Map Database Release 2016. *GFZ Data Services*, doi:http://doi.org/10.5880/WSM.2016.001.

Heidbach, O., Reinecker, J., Tingay, M., Müller, B., Sperner, B., Fuchs, K., & Wenzel, F. (2007). Plate boundary forces are not enough: Second-and third-order stress patterns highlighted in the World Stress Map database. *Tectonics*, *26*(6), doi:10.1029/2007TC002133.

Hessami, K., Nilforoushan, F., & Talbot, C.J. (2006). Active deformation within the Zagros Mountains deduced from GPS measurements. *Journal of the Geological Society*, *163*(1), 143–148.

Hollingsworth, J., Fattahi, M., Walker, R., Talebian, M., Bahroudi, A., Bolourchi, M.J., Jackson, J., & Copley, A. (2010). Oroclinal bending, distributed thrust and strike-slip faulting, and the accommodation of Arabia–Eurasia convergence in NE Iran since the Oligocene. *Geophysical Journal International*, *181*(3), 1214–1246.

Irandoust, M.A., Priestley, K., & Sobouti, F. (2022). High-resolution Lithospheric Structure of the Zagros Collision Zone and Iranian Plateau. *Journal of Geophysical Research: Solid Earth*, *127*(11), e2022JB025009, doi:https://doi.org/10.1029/2022JB025009.

Jackson, J. & McKenzie, D. (1984). Active tectonics of the Alpine—Himalayan Belt between western Turkey and Pakistan. *Geophysical Journal International*, *77*(1), 185–264.

585 Jackson, J., Priestley, K., Allen, M., & Berberian, M. (2002). Active tectonics of the south Caspian
586 basin. *Geophysical Journal International*, *148*(2), 214–245.

587 Jolivet, L. & Faccenna, C. (2000). Mediterranean extension and the Africa-Eurasia collision. *Tectonics*,
588 *19*(6), 1095–1106.

589 Kaviani, A., Hatzfeld, D., Paul, A., Tatar, M., & Priestley, K. (2009). Shear-wave splitting, lithospheric
590 anisotropy, and mantle deformation beneath the Arabia–Eurasia collision zone in Iran. *Earth and*
591 *Planetary Science Letters*, *286*(3-4), 371–378.

592 Kaviani, A., Mahmoodabadi, M., Rümpker, G., Pilia, S., Tatar, M., Nilfouroushan, F., Yamini-Fard,
593 F., Moradi, A., & Ali, M.Y. (2021). Mantle-flow diversion beneath the Iranian plateau induced by
594 Zagros' lithospheric keel. *Scientific reports*, *11*(1), 1–12.

595 Khodaverdian, A., Zafarani, H., & Rahimian, M. (2015). Long term fault slip rates, distributed defor-
596 mation rates and forecast of seismicity in the Iranian Plateau. *Tectonics*, *34*(10), 2190–2220.

597 Khorrami, F., Vernant, P., Masson, F., Nilfouroushan, F., Mousavi, Z., Nankali, H., Saadat, S.A.,
598 Walpersdorf, A., Hosseini, S., Tavakoli, P., et al. (2019). An up-to-date crustal deformation map
599 of Iran using integrated campaign-mode and permanent GPS velocities. *Geophysical Journal Inter-*
600 *national*, *217*(2), 832–843.

601 Koptev, A. & Ershov, A. (2010). The role of the gravitational potential of the lithosphere in the formation
602 of a global stress field. *Izvestiya, Physics of the Solid Earth*, *46*(12), 1080–1094.

603 Kreemer, C., Blewitt, G., & Klein, E.C. (2014). A geodetic plate motion and Global Strain Rate Model.
604 *Geochemistry, Geophysics, Geosystems*, *15*(10), 3849–3889.

605 Kustowski, B., Ekström, G., & Dziewoński, A. (2008a). Anisotropic shear-wave velocity structure of
606 the Earth's mantle: A global model. *Journal of Geophysical Research: Solid Earth*, *113*(B6).

607 Kustowski, B., Ekström, G., & Dziewoński, A. (2008b). The shear-wave velocity structure in the upper
608 mantle beneath Eurasia. *Geophysical Journal International*, *174*(3), 978–992.

609 Le Dortz, K., Meyer, B., Sébrier, M., Nazari, H., Braucher, R., Fattahi, M., Benedetti, L., Foroutan, M.,
610 Siame, L., Bourlès, D., et al. (2009). Holocene right-slip rate determined by cosmogenic and OSL
611 dating on the Anar fault, Central Iran. *Geophysical Journal International*, *179*(2), 700–710.

612 Lithgow-Bertelloni, C. & Guynn, J.H. (2004). Origin of the lithospheric stress field. *Journal of Geo-*
613 *physical Research: Solid Earth*, *109*(B1), doi:10.1029/2003JB002467.

Masson, F., Anvari, M., Djamour, Y., Walpersdorf, A., Tavakoli, F., Daignieres, M., Nankali, H., & Van Gorp, S. (2007). Large-scale velocity field and strain tensor in Iran inferred from GPS measurements: new insight for the present-day deformation pattern within NE Iran. *Geophysical Journal International*, *170*(1), 436–440.

Masson, F., Djamour, Y., Van Gorp, S., Chéry, J., Tatar, M., Tavakoli, F., Nankali, H., & Vernant, P. (2006). Extension in NW Iran driven by the motion of the South Caspian Basin. *Earth and Planetary Science Letters*, *252*(1-2), 180–188.

Mazhari, S., Bea, F., Amini, S., Ghalamghash, J., Molina, J., Montero, P., Scarrow, J., & Williams, I. (2009). The Eocene bimodal Piranshahr massif of the Sanandaj–Sirjan Zone, NW Iran: a marker of the end of the collision in the Zagros orogen. *Journal of the Geological Society*, *166*(1), 53–69.

McClusky, S., Balassanian, S., Barka, A., Demir, C., Ergintav, S., Georgiev, I., Gurkan, O., Hamburger, M., Hurst, K., Kahle, H., et al. (2000). Global Positioning System constraints on plate kinematics and dynamics in the eastern Mediterranean and Caucasus. *Journal of Geophysical Research: Solid Earth*, *105*(B3), 5695–5719.

Md, S.I. & Ryuichi, S. (2010). Neotectonic stress field and deformation pattern within the Zagros and its adjoining area: An approach from finite element modeling. *Journal of Geology and Mining Research*, *2*(7), 170–182.

Mégnin, C. & Romanowicz, B. (2000). The three-dimensional shear velocity structure of the mantle from the inversion of body, surface and higher-mode waveforms. *Geophysical Journal International*, *143*(3), 709–728.

Raeesi, M., Zarifi, Z., Nilfouroushan, F., Boroujeni, S.A., & Tiampo, K. (2017). Quantitative analysis of seismicity in Iran. *Pure and Applied Geophysics*, *174*(3), 793–833.

Reilinger, R. & McClusky, S. (2011). Nubia–Arabia–Eurasia plate motions and the dynamics of Mediterranean and Middle East tectonics. *Geophysical Journal International*, *186*(3), 971–979.

Reilinger, R., McClusky, S., Paradissis, D., Ergintav, S., & Vernant, P. (2010). Geodetic constraints on the tectonic evolution of the Aegean region and strain accumulation along the Hellenic subduction zone. *Tectonophysics*, *488*(1-4), 22–30.

Reilinger, R., McClusky, S., Vernant, P., Lawrence, S., Ergintav, S., Cakmak, R., Ozener, H., Kadirov, F., Guliev, I., Stepanyan, R., Nadariya, M., Hahubia, G., Mahmoud, S., Sakr, K., ArRajehi, A., Paradissis,

643 D., Al-Aydrus, A., Prilepin, M., Guseva, T., Evren, E., Dmitrotsa, A., Filikov, S.V., Gomez, F., Al-
644 Ghazzi, R., & Karamm, G. (2006). GPS constraints on continental deformation in the Africa-Arabia-
645 Eurasia continental collision zone and implications for the dynamics of plate interactions. *Journal of*
646 *Geophysical Research: Solid Earth*, *111*(B5), doi:10.1029/2005JB004051.

647 Richardson, R.M., Solomon, S.C., & Sleep, N.H. (1976). Intraplate stress as an indicator of plate tectonic
648 driving forces. *Journal of geophysical research*, *81*(11), 1847–1856.

649 Ritsema, J., Deuss, A.A., Van Heijst, H.J., & Woodhouse, J.H. (2011). S40RTS: a degree-40 shear-
650 velocity model for the mantle from new Rayleigh wave dispersion, teleseismic traveltime and normal-
651 mode splitting function measurements. *Geophysical Journal International*, *184*(3), 1223–1236.

652 Sadeghi-Bagherabadi, A., Sobouti, F., Ghods, A., Motaghi, K., Talebian, M., Chen, L., Jiang, M., Ai, Y.,
653 & He, Y. (2018). Upper mantle anisotropy and deformation beneath the major thrust-and-fold belts of
654 Zagros and Alborz and the Iranian Plateau. *Geophysical Journal International*, *214*(3), 1913–1918.

655 Sattarzadeh, Y., Cosgrove, J.W., & Vita-Finzi, C. (2002). The geometry of structures in the Zagros cover
656 rocks and its neotectonic implications. *Geological Society, London, Special Publications*, *195*(1),
657 205–217.

658 Singh, S. & Ghosh, A. (2019). Surface motions and continental deformation in the Indian plate and
659 the India-Eurasia collision zone. *Journal of Geophysical Research: Solid Earth*, *124*, doi:10.1029/
660 2018JB017289.

661 Singh, S. & Ghosh, A. (2020). The role of crustal models in the dynamics of the India–Eurasia collision
662 zone. *Geophysical Journal International*, *223*(1), 111–131.

663 Sobouti, F. & Arkani-Hamed, J. (1996). Numerical modelling of the deformation of the Iranian plateau.
664 *Geophysical Journal International*, *126*(3), 805–818.

665 Talebian, M. & Jackson, J. (2002). Offset on the Main Recent Fault of NW Iran and implications for
666 the late Cenozoic tectonics of the Arabia–Eurasia collision zone. *Geophysical Journal International*,
667 *150*(2), 422–439.

668 Tatar, M. & Hatzfeld, D. (2009). Microseismic evidence of slip partitioning for the Rudbar-Tarom earth-
669 quake (Ms 7.7) of 1990 June 20 in NW Iran. *Geophysical Journal International*, *176*(2), 529–541.

670 Vernant, P. & Chéry, J. (2006). Mechanical modelling of oblique convergence in the Zagros, Iran. *Geo-*
671 *physical Journal International*, *165*(3), 991–1002.

Vernant, P., Nilforoushan, F., Hatzfeld, D., Abbassi, M., Vigny, C., Masson, F., Nankali, H., Martinod, J., Ashtiani, A., Bayer, R., et al. (2004). Present-day crustal deformation and plate kinematics in the Middle East constrained by GPS measurements in Iran and northern Oman. *Geophysical Journal International*, *157*(1), 381–398.

Vincent, S.J., Allen, M.B., Ismail-Zadeh, A.D., Flecker, R., Foland, K.A., & Simmons, M.D. (2005). Insights from the Talysh of Azerbaijan into the Paleogene evolution of the South Caspian region. *Geological Society of America Bulletin*, *117*(11-12), 1513–1533.

Walker, R.T. (2006). A remote sensing study of active folding and faulting in southern Kerman province, SE Iran. *Journal of Structural Geology*, *28*(4), 654–668.

Walpersdorf, A., Hatzfeld, D., Nankali, H., Tavakoli, F., Nilforoushan, F., Tatar, M., Vernant, P., Chéry, J., & Masson, F. (2006). Difference in the GPS deformation pattern of North and Central Zagros (Iran). *Geophysical Journal International*, *167*(3), 1077–1088.

Walpersdorf, A., Manighetti, I., Mousavi, Z., Tavakoli, F., Vergnolle, M., Jadidi, A., Hatzfeld, D., Aghamohammadi, A., Bigot, A., Djamour, Y., et al. (2014). Present-day kinematics and fault slip rates in eastern Iran, derived from 11 years of GPS data. *Journal of Geophysical Research: Solid Earth*, *119*(2), 1359–1383.

Yadav, R. & Tiwari, V. (2018). Numerical simulation of present day tectonic stress across the Indian subcontinent. *International Journal of Earth Sciences*, *107*(7), 2449–2462.

Yamato, P., Kaus, B.J., Mouthereau, F., & Castelltort, S. (2011). Dynamic constraints on the crustal-scale rheology of the Zagros fold belt, Iran. *Geology*, *39*(9), 815–818.

Yang, Y., Liang, C., Fang, L., Su, J., & Hua, Q. (2018). A comprehensive analysis on the stress field and seismic anisotropy in eastern Tibet. *Tectonics*, *37*(6), 1648–1657.

Zoback, M.L. (1992). First-and second-order patterns of stress in the lithosphere: The World Stress Map Project. *Journal of Geophysical Research: Solid Earth*, *97*(B8), 11703–11728.

**Figure 1:** Tectonic overview of Central Eurasia. Abbreviations: CF: Chaman Fault; MSZ: Makran Subduction Zone; MZT: Main Zagros Thrust; HZF: High Zagros Fault; MFF: Mountain Front Fault; SSZ: Sanandaj Sirjan Zone; UDMA: Urumieh-Dokhtar Arc; MRF: Main Recent Fault.

**Figure 2:** Thickness and density variations of different crustal layers in all three crustal and lithospheric models.

**Figure 3:** (a) Most compressive horizontal principal axes ($SH_{max}$) from WSM (Heidbach et al., 2016). Red indicates normal fault regime, blue indicates thrust regime, whereas green denotes strike-slip regime, (b) Observed plate velocities in a no-net-rotation frame of reference from Kreemer et al. (2014) plotted on top of second invariant of strain rate tensors obtained from Kreemer et al. (2014) plotted on $1^\circ \times 1^\circ$ grid.

**Figure 4:** (Left Panel) Deviatoric stresses predicted from GPE variations, plotted on top of their second invariants. The compressional stresses are denoted by solid black arrows, while white arrows show tensional stresses. $SH_{max}$ axes predicted from GPE variations are plotted in right panel. Red denotes tensional regime, blue is for thrust and green for strike-slip regime.

**Figure 5:** (Left Panel) Total misfit between observed and predicted $SH_{max}$ from GPE variations. Correlation coefficients between strain rate tensors obtained from Kreemer et al. (2014) and deviatoric stresses predicted using GPE variations are shown in middle panel, with average regional correlation coefficients given on bottom right of each figure. (Right panel) Observed velocities (black) and predicted plate velocities(white) from GPE variations in NNR frame, plotted on the top of angular misfit between both.

**Figure 6:** (Left Panel) Deviatoric stresses predicted using mantle tractions derived from various tomography models for GHW13 viscosity structure, plotted on second invariant of deviatoric stresses. The white arrows denote tensional stresses, and black arrows indicate compressional stresses. $SH_{max}$ predicted from mantle tractions are shown in right panel. Red denotes tensional regime, blue is for thrust and green is for strike-slip regime.

**Figure 7:** Parameters predicted from mantle tractions and their comparisons with observables. (Left panel) Total misfit between $SH_{max}$ obtained from WSM (Heidbach et al., 2016) and those predicted using mantle tractions derived from various tomography models using GHW13 viscosity structure. Correlation coefficients between strain rate tensors obtained from Kreemer et al. (2014) and deviatoric stresses predicted using basal tractions are shown in middle panel, with average regional correlation coefficients given on bottom right of each figure. (Right pannel) Observed velocities (black) and plate velocities predicted using mantle tractions (white) in NNR frame plotted on the top of angular deviation between both.

**Figure 8:** (Left panel) Deviatoric stresses predicted using combined effects of GPE computed from CRUST2 and mantle tractions derived from various tomography models plotted on top of their second invariants. The white arrows denote tensional stresses, and black arrows indicate compressional stresses. The right panel shows $SH_{max}$ predicted from these models. The red lines denote tensional regime, blue is for thrust and green is for strike-slip regime.

**Figure 9:** (Left panel) Deviatoric stresses (a-d) predicted using combined effects of GPE computed from CRUST1 and mantle tractions derived from various tomography models plotted on top of their second invariants. The white arrows denote tensional stresses, and black arrows indicate compressional stresses. The right panel shows $SH_{max}$ predicted from these models. The red lines denote tensional regime, blue is for thrust and green is for strike-slip regime.

**Figure 10:** (Left panel) Deviatoric stresses (a-d) predicted using combined effects of GPE computed from LITHO and mantle tractions derived from various tomography models plotted on top of their second invariants. The white arrows denote tensional stresses, and black arrows indicate compressional stresses. The right panel shows $SH_{max}$ predicted from these models. The red lines denote tensional regime, blue is for thrust and green is for strike-slip regime.

**Figure 11:** Total misfit between observed $SH_{max}$ from WSM (Heidbach et al., 2016) and $SH_{max}$ predicted using combined effects of GPE computed from different crustal models and mantle tractions derived from various tomography models.

**Figure 12:** Correlation coefficients between strain rate tensors from Kreemer et al. (2014) and deviatoric stress tensors predicted using combined effects of GPE computed from different crustal models and mantle tractions derived from various tomography models. Average correlation coefficient is given in right lower corner of the figure.

**Figure 13:** Plate velocities predicted using combined effects of GPE computed from different crustal models and mantle tractions derived from various tomography models plotted on top of angular misfit ($\theta$). Black arrows represent observed NNR velocities (Kreemer et al., 2014) and white ones denote predicted velocities.

**Figure 14:** Predicted parameters of best fit model, S40RTScr2. (a) GPS (blue) and predicted (red) plate velocities with respect to a fixed Eurasian plate, (b) FPDs and $SH_{max}$ are plotted for the best fit model, (c) Correlation between deviatoric stresses predicted from GPE and mantle convection models, and (d) ratio ($T_1/T_2$) of second invariant of deviatoric stresses from GPE ($T_1$) to those from mantle tractions ($T_2$).

**Figures.**

Figure 1:

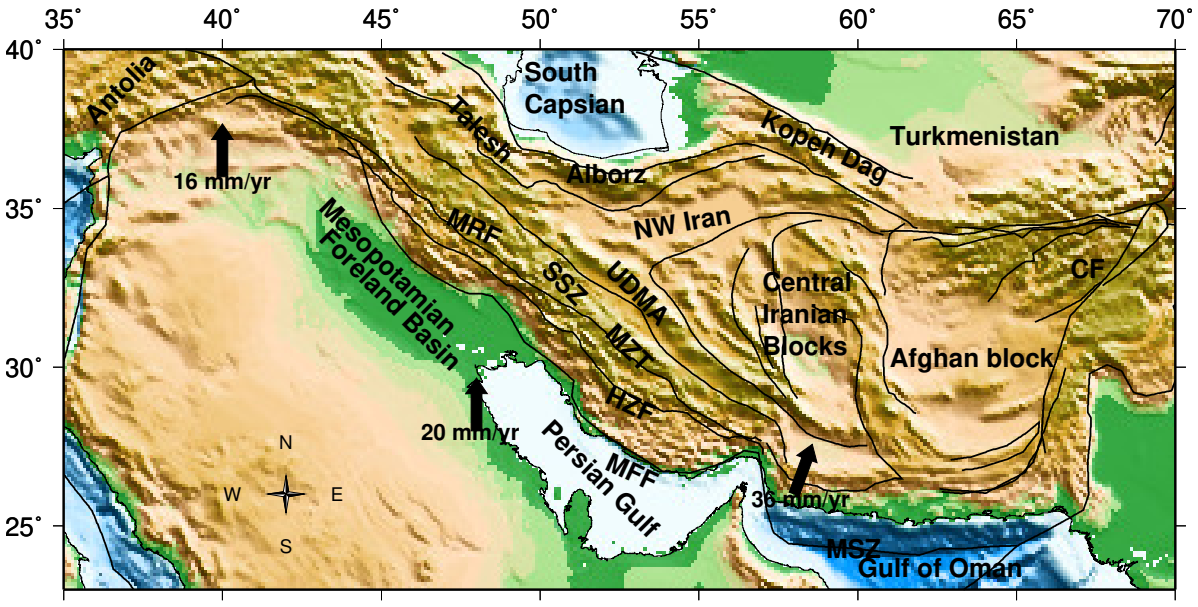
35˚
40˚
45˚
50˚
55˚
60˚
65˚
70˚
40˚
35˚
30˚
25˚
Anatolia
16 mm/yr
Talesh
South
Capsian
Alborz
Kopeh Dag
Turkmenistan
MRF
NW Iran
Mesopotamian
Foreland Basin
SSZ
UDMA
MZT
HZF
CF
Central
Iranian
Blocks
Afghan block
20 mm/yr
Persian Gulf
MFF
36 mm/yr
MSZ
Gulf of Oman
N
W
E
S

Figure 2:

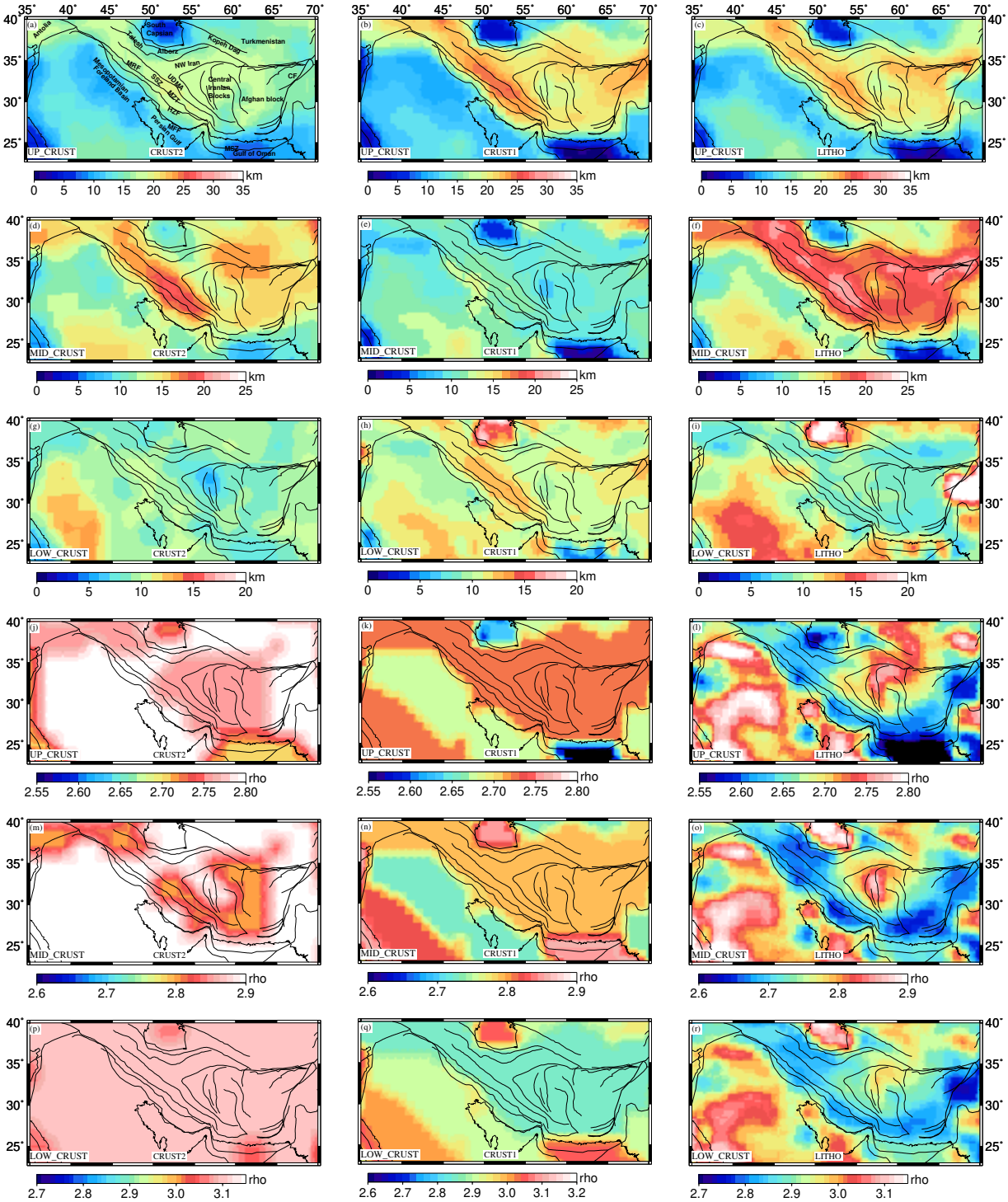
(a)
(b)
(c)
(d)
(e)
(f)
(g)
(h)
(i)
(j)
(k)
(l)
(m)
(n)
(o)
(p)
(q)
(r)
South Caspian
Turkmenistan
Alborz
NW Iran
Central Iranian Blocks
Afghan block
CF
MBF
SSZ
MZT
YDF
Persian Gulf
MSZ
Gulf of Oman
UP_CRUST
MID_CRUST
LOW_CRUST
CRUST1
CRUST2
LITHO
km
rho

Figure 3:

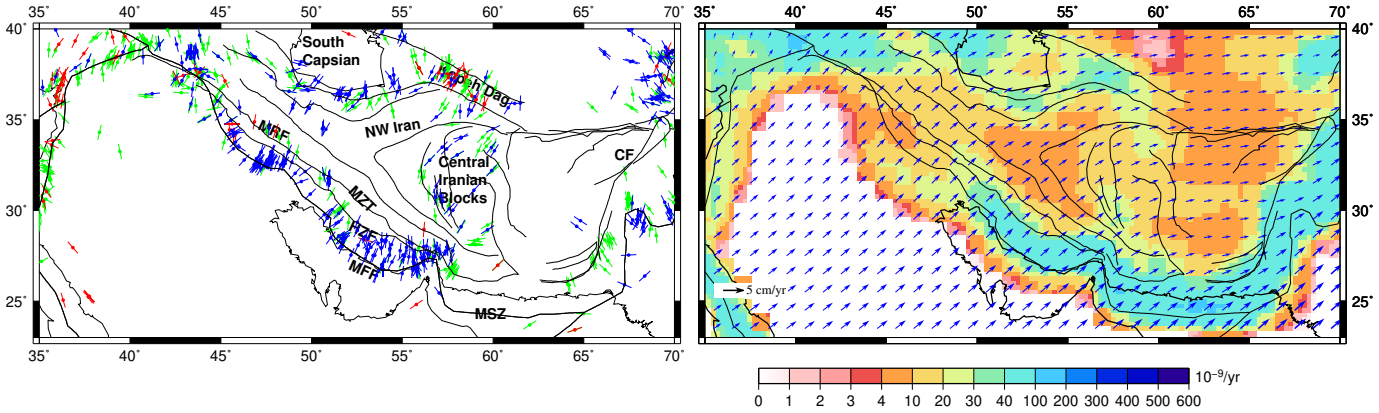
35˚
40˚
45˚
50˚
55˚
60˚
65˚
70˚
25˚
30˚
35˚
40˚
South Capsian
Kopeh Dag
NW Iran
MRF
Central Iranian Blocks
CF
MZT
HZT
MFR
MSZ
5 cm/yr
0 1 2 3 4 10 20 30 40 100 200 300 400 500 600
10⁻⁹/yr

Figure 4:

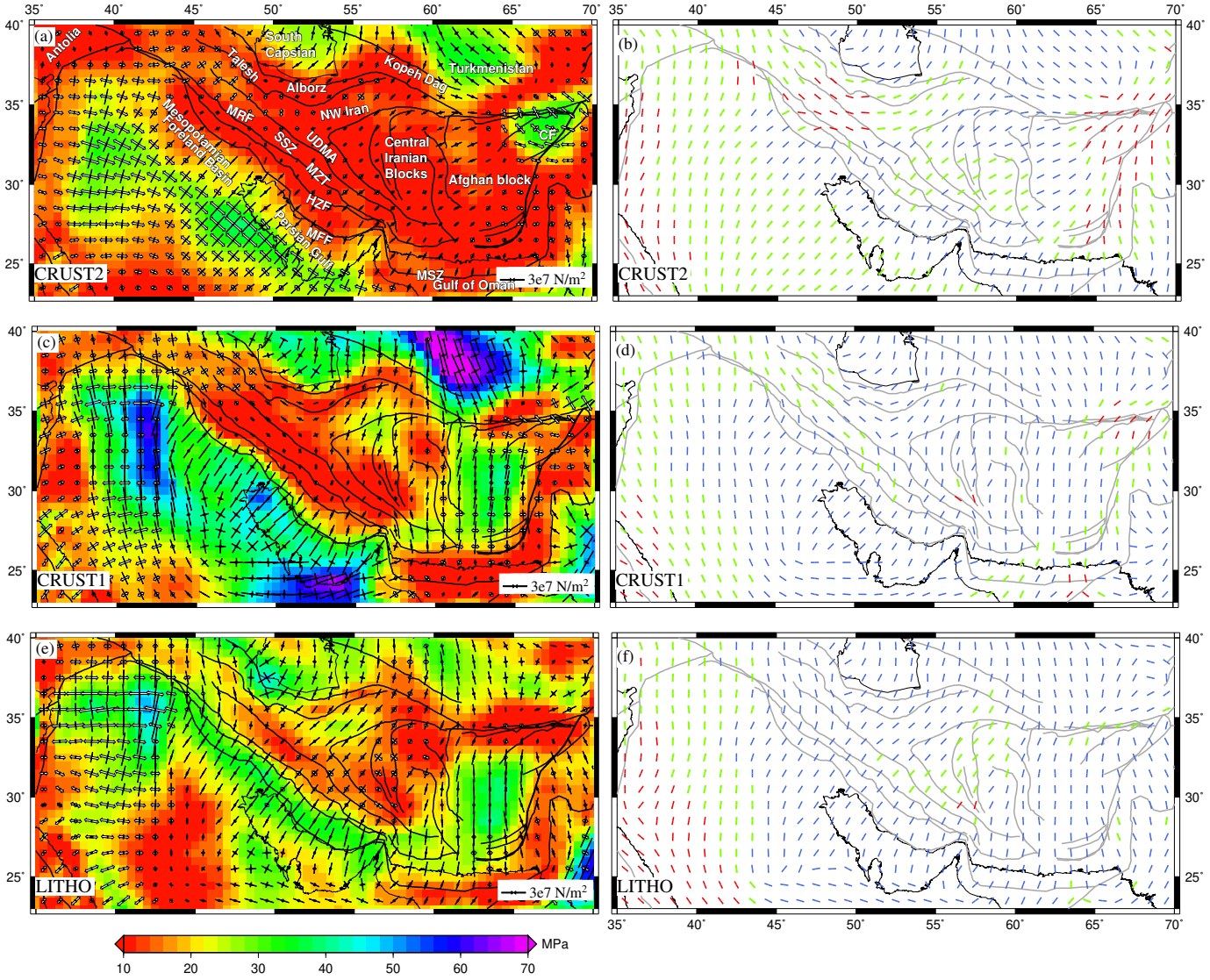
(a)
(b)
(c)
(d)
(e)
(f)
Anatolia
South Caspian
Turkmenistan
Kopeh Dag
Alborz
Talesh
NW Iran
MRF
SSZ
UDMA
MZT
HZF
MFF
CF
Central Iranian Blocks
Afghan block
Mesopotamian Foreland Basin
Persian Gulf
MSZ
Gulf of Oman
CRUST2
CRUST1
LITHO
3e7 N/m²
MPa
10
20
30
40
50
60
70
35°
40°
45°
50°
55°
60°
65°
70°
25°
30°
35°
40°

Figure 5:

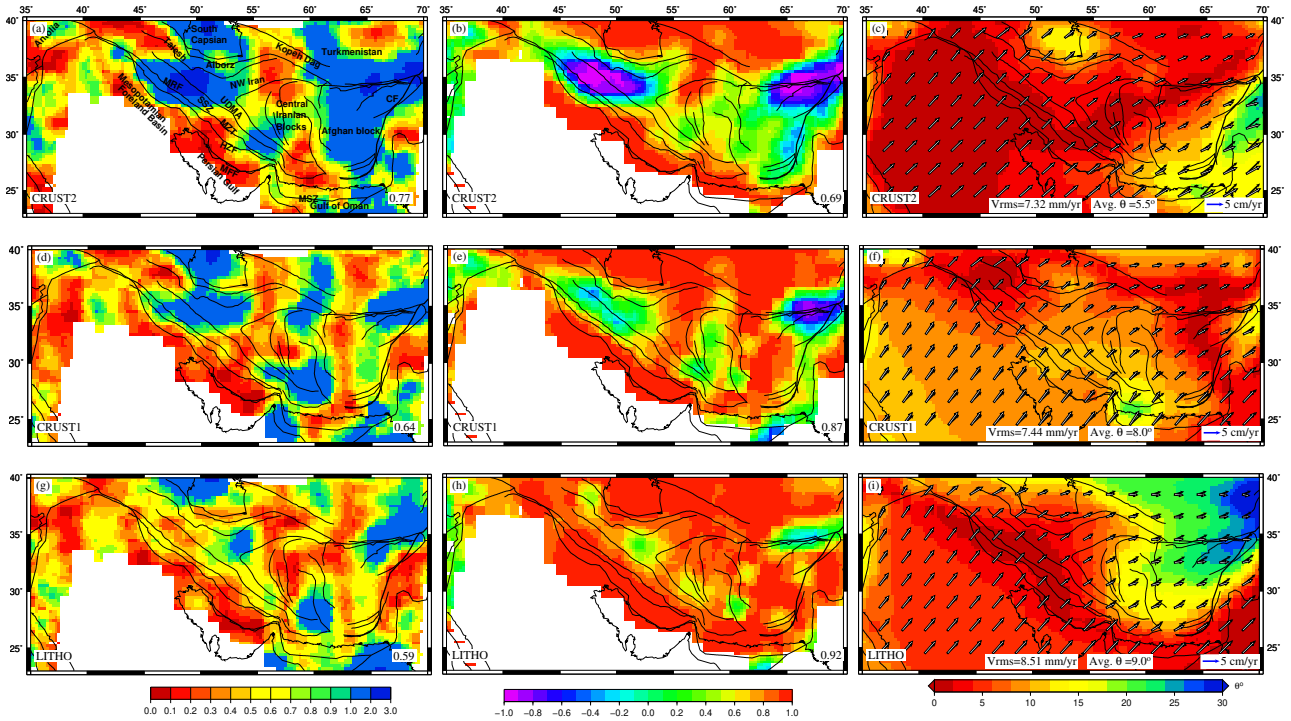
(a)
(b)
(c)
(d)
(e)
(f)
(g)
(h)
(i)
CRUST2
CRUST1
LITHO
0.77
0.69
0.64
0.87
0.59
0.92
Vrms=7.32 mm/yr
Avg. θ =5.5°
Vrms=7.44 mm/yr
Avg. θ =8.0°
Vrms=8.51 mm/yr
Avg. θ =9.0°
5 cm/yr
South Caspian
Turkmenistan
Alborz
NW Iran
Central Iranian Blocks
Afghan block
CF
MRF
SSZ
UDMA
MFZ
RRF
MSZ
Gulf of Oman
Makran Basin
Makran Wedge
Kopeh Dagh
Amu Dar
Tarim
0.0 0.1 0.2 0.3 0.4 0.5 0.6 0.7 0.8 0.9 1.0 2.0 3.0
−1.0 −0.8 −0.6 −0.4 −0.2 0.0 0.2 0.4 0.6 0.8 1.0
0 5 10 15 20 25 30 θ°

Figure 6:

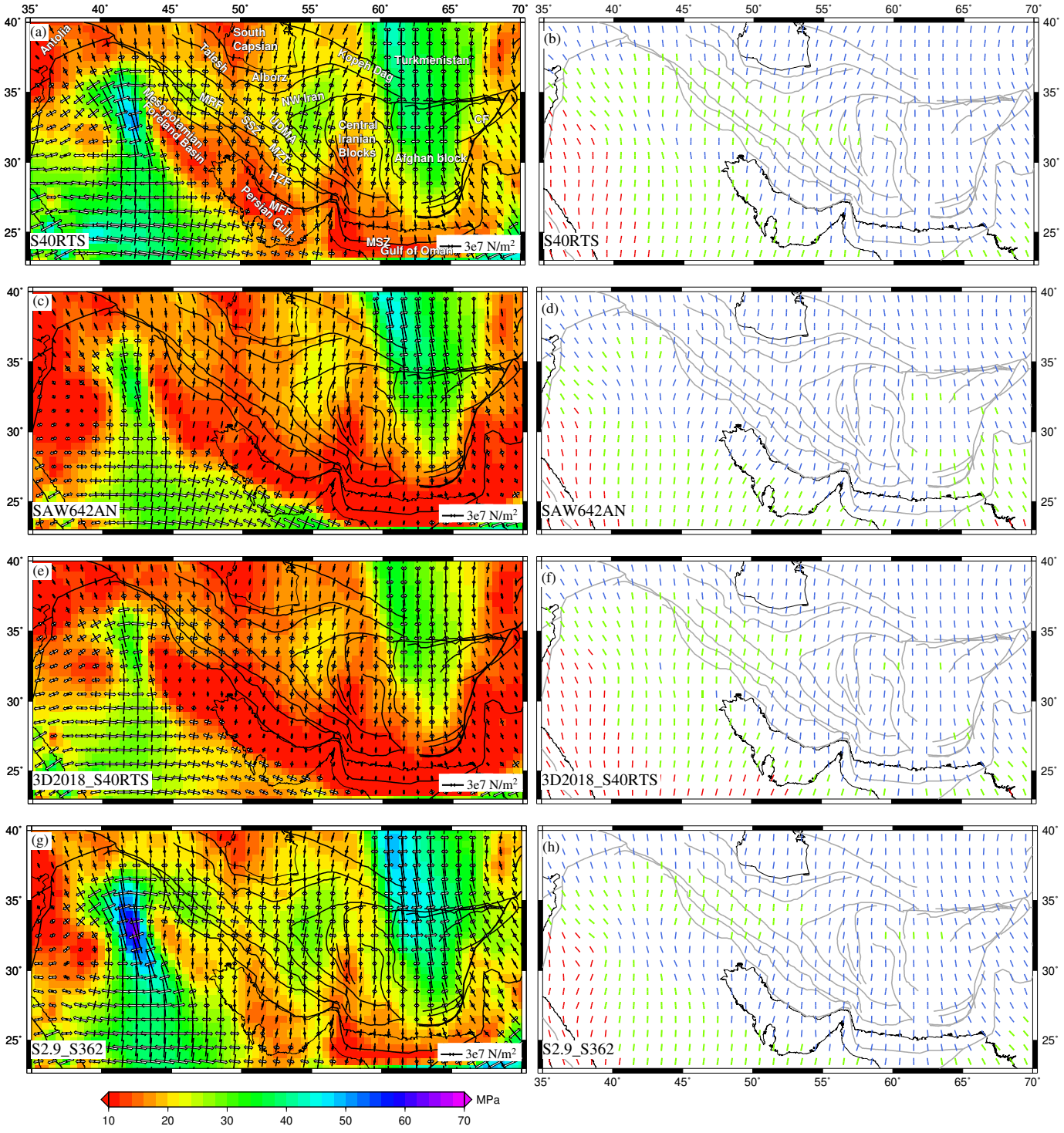
(a)
S40RTS
(b)
S40RTS
(c)
SAW642AN
(d)
SAW642AN
(e)
3D2018_S40RTS
(f)
3D2018_S40RTS
(g)
S2.9_S362
(h)
S2.9_S362
3e7 N/m²
Anatolia
South Caspian
Turkmenistan
Kopeh Dagh
Alborz
Zagros
Mesopotamian and Basin
NW Iran
Central Iranian Blocks
Afghan block
CF
MFF
HZF
MZF
SSF
ZDMA
Persian Gulf
MSZ
Gulf of Oman
MPa
10
20
30
40
50
60
70

Figure 7:

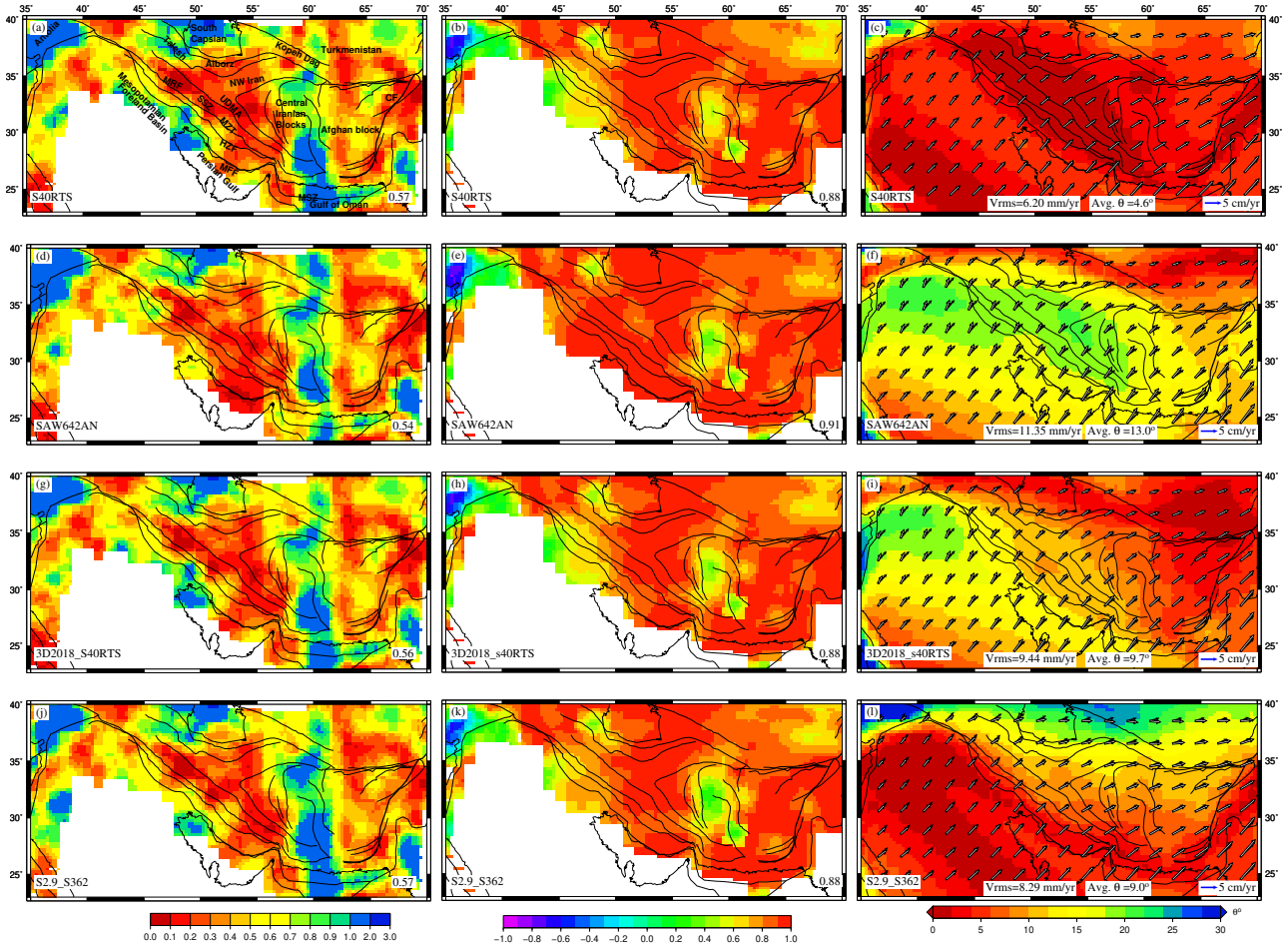
(a)
(b)
(c)
(d)
(e)
(f)
(g)
(h)
(i)
(j)
(k)
(l)
South Caspian
Turkmenistan
Kopeh Dagh
Alborz
NW Iran
Central Iranian Blocks
Afghan block
CF
MRF
SSZ
UDMA
HFF
MFF
Persian Gulf
MSZ
Gulf of Oman
Arabia
Zagros
Mesopotamian Foreland Basin
S40RTS
SAW642AN
3D2018_S40RTS
3D2018_s40RTS
S2.9_S362
0.57
0.88
0.54
0.91
0.56
Vrms=6.20 mm/yr
Avg. θ =4.6°
Vrms=11.35 mm/yr
Avg. θ =13.0°
Vrms=9.44 mm/yr
Avg. θ =9.7°
Vrms=8.29 mm/yr
Avg. θ =9.0°
5 cm/yr
0.0 0.1 0.2 0.3 0.4 0.5 0.6 0.7 0.8 0.9 1.0 2.0 3.0
−1.0 −0.8 −0.6 −0.4 −0.2 0.0 0.2 0.4 0.6 0.8 1.0
θ°
0 5 10 15 20 25 30

Figure 8:

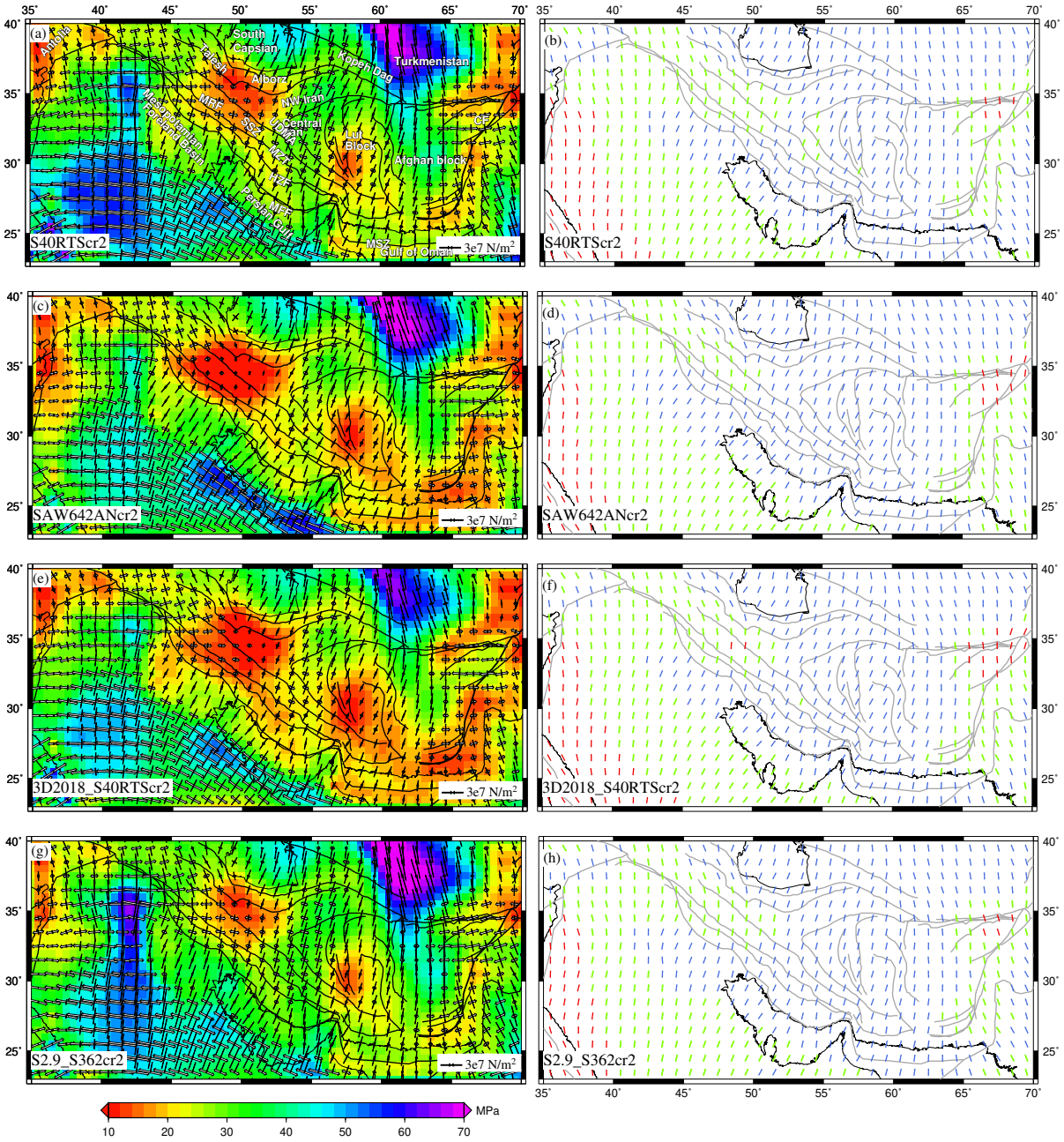
(a)
(b)
(c)
(d)
(e)
(f)
(g)
(h)
South Caspian
Turkmenistan
Alborz
Kopeh Dag
Kura
Central Iran
Lut Block
Afghan block
Zagros
MFF
MZT
MZRF
MZ2
MZ1
Persian Gulf
MSZ
Gulf of Oman
S40RTScr2
SAW642ANcr2
3D2018_S40RTScr2
S2.9_S362cr2
3e7 N/m2
MPa
10
20
30
40
50
60
70

Figure 9:

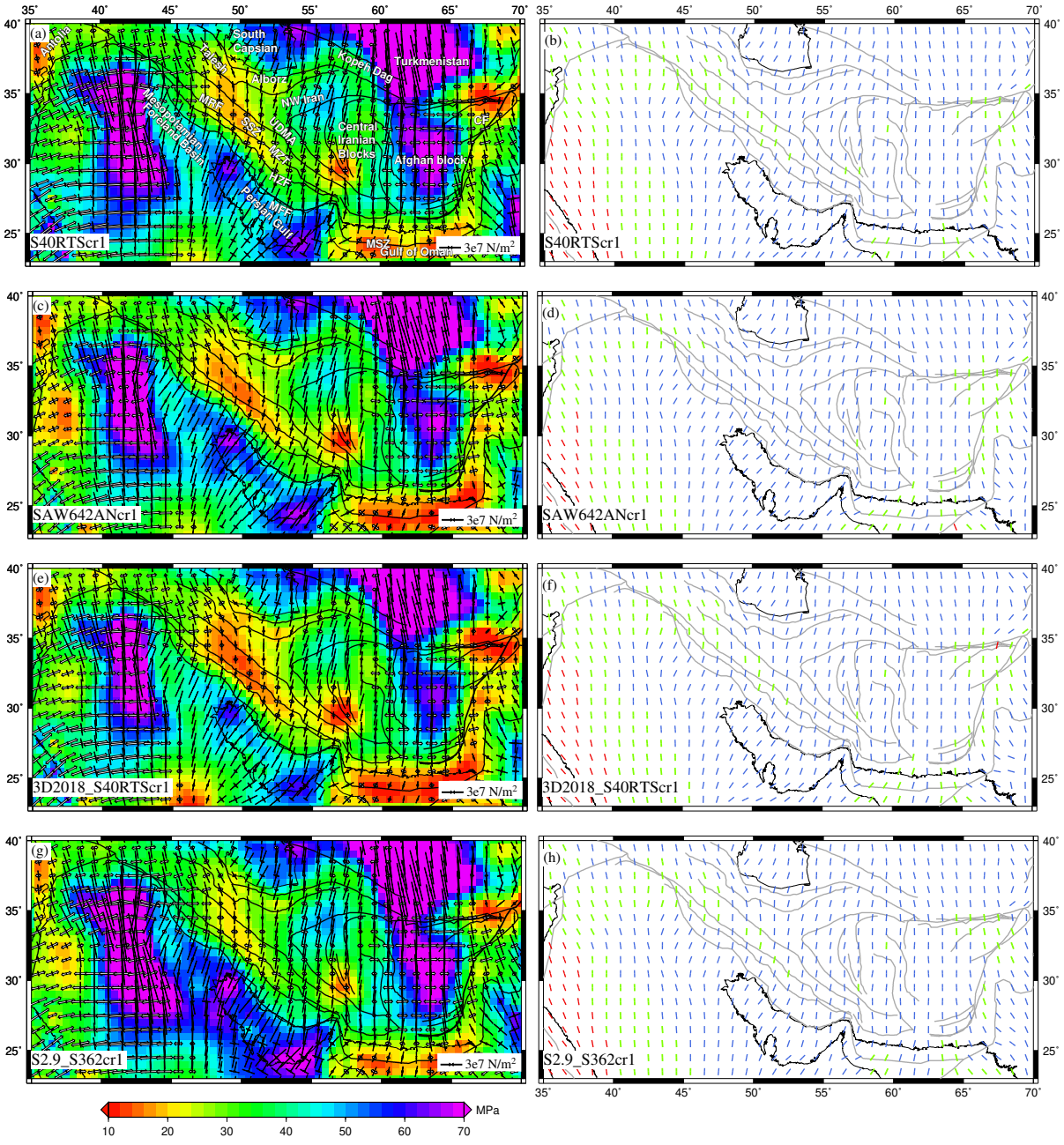
(a)
(b)
(c)
(d)
(e)
(f)
(g)
(h)
South Caspian
Turkmenistan
Kopeh Dag
Alborz
NWIran
Zagros
Mesopotamian Foredeep Basin
SSZ
UDMA
HZF
MFF
Persian Gulf
Central Iranian Blocks
Afghan block
MSZ
Gulf of Oman
S40RTScr1
SAW642ANcr1
3D2018_S40RTScr1
S2.9_S362cr1
3e7 N/m²
MPa
10
20
30
40
50
60
70

Figure 10:

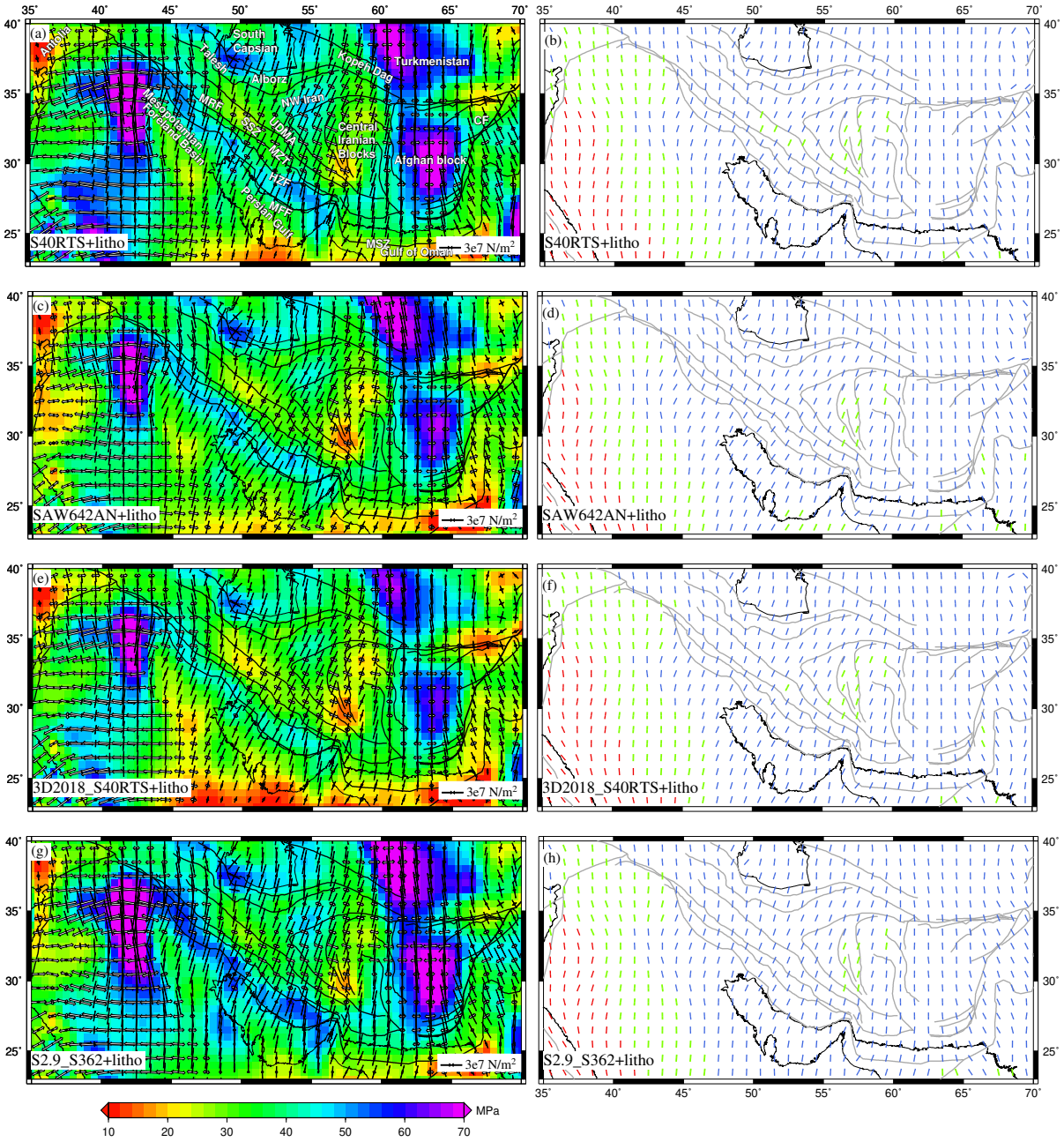
(a)
(b)
(c)
(d)
(e)
(f)
(g)
(h)
South Caspian
Turkmenistan
Alborz
Kopeh Dag
NW Iran
Central Iranian Blocks
Afghan block
CE
Makran
Zagros
MFF
HZF
MZT
SSZ
DDMA
Persian Gulf
MSZ
Gulf of Oman
S40RTS+litho
SAW642AN+litho
3D2018_S40RTS+litho
S2.9_S362+litho
3e7 N/m$^2$
MPa
10
20
30
40
50
60
70
35˚
40˚
45˚
50˚
55˚
60˚
65˚
70˚
25˚
30˚

Figure 11:

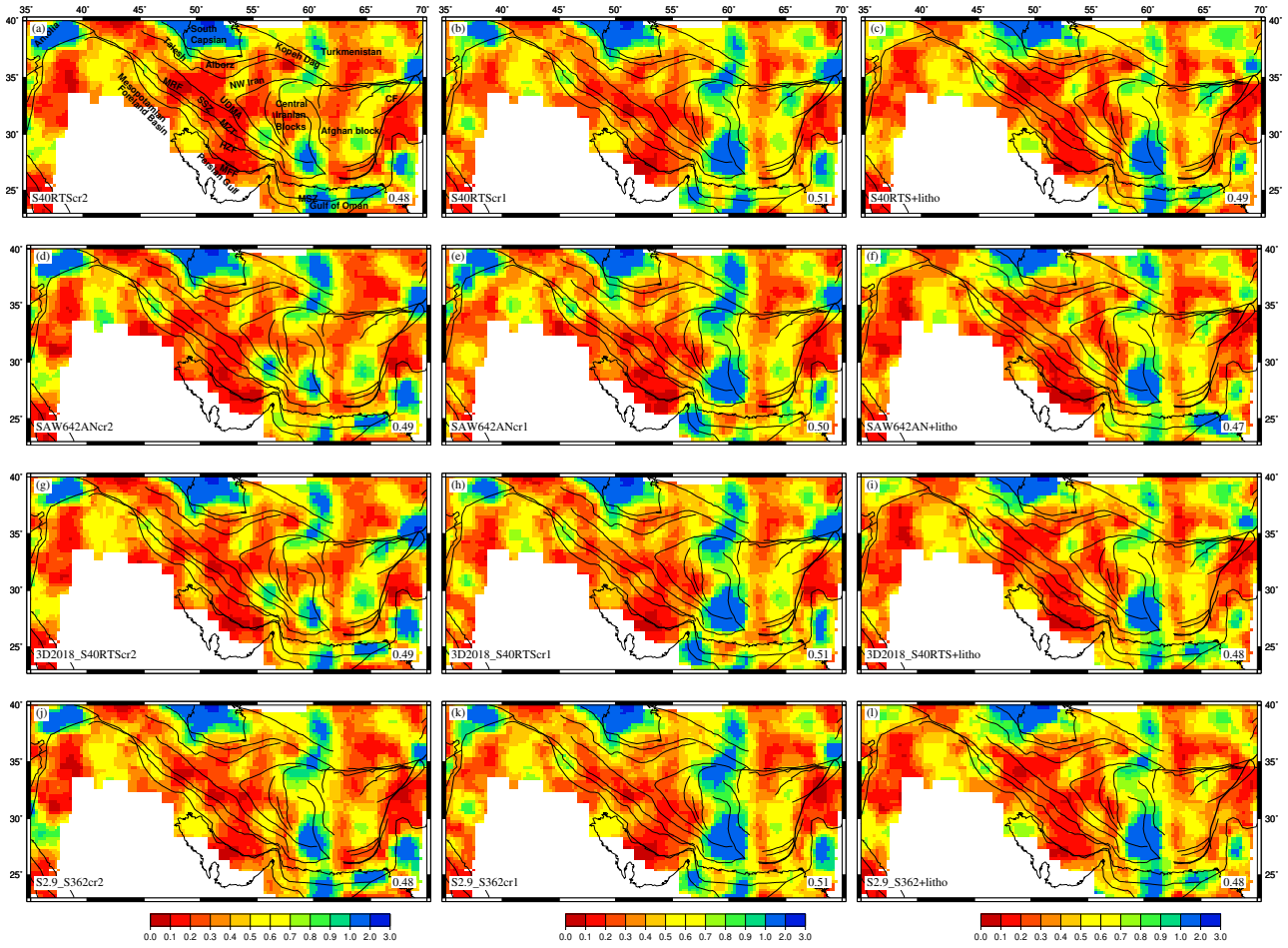
(a)
(b)
(c)
(d)
(e)
(f)
(g)
(h)
(i)
(j)
(k)
(l)
S40RTScr2 0.48
S40RTScr1 0.51
S40RTS+litho 0.49
SAW642ANcr2 0.49
SAW642ANcr1 0.50
SAW642AN+litho 0.47
3D2018_S40RTScr2 0.49
3D2018_S40RTScr1 0.51
3D2018_S40RTS+litho 0.48
S2.9_S362cr2 0.48
S2.9_S362cr1 0.51
S2.9_S362+litho 0.48
South Caspian
Turkmenistan
Alborz
NW Iran
Central Iranian Blocks
Afghan block
CF
MZT
SSZ
UDMA
MZF
RRF
MFF
Persian Gulf
MSZ
Gulf of Oman
Mesopotamian Foreland Basin
Zagros
Kopeh Dagh
Arabia
0.0 0.1 0.2 0.3 0.4 0.5 0.6 0.7 0.8 0.9 1.0 2.0 3.0

Figure 12:

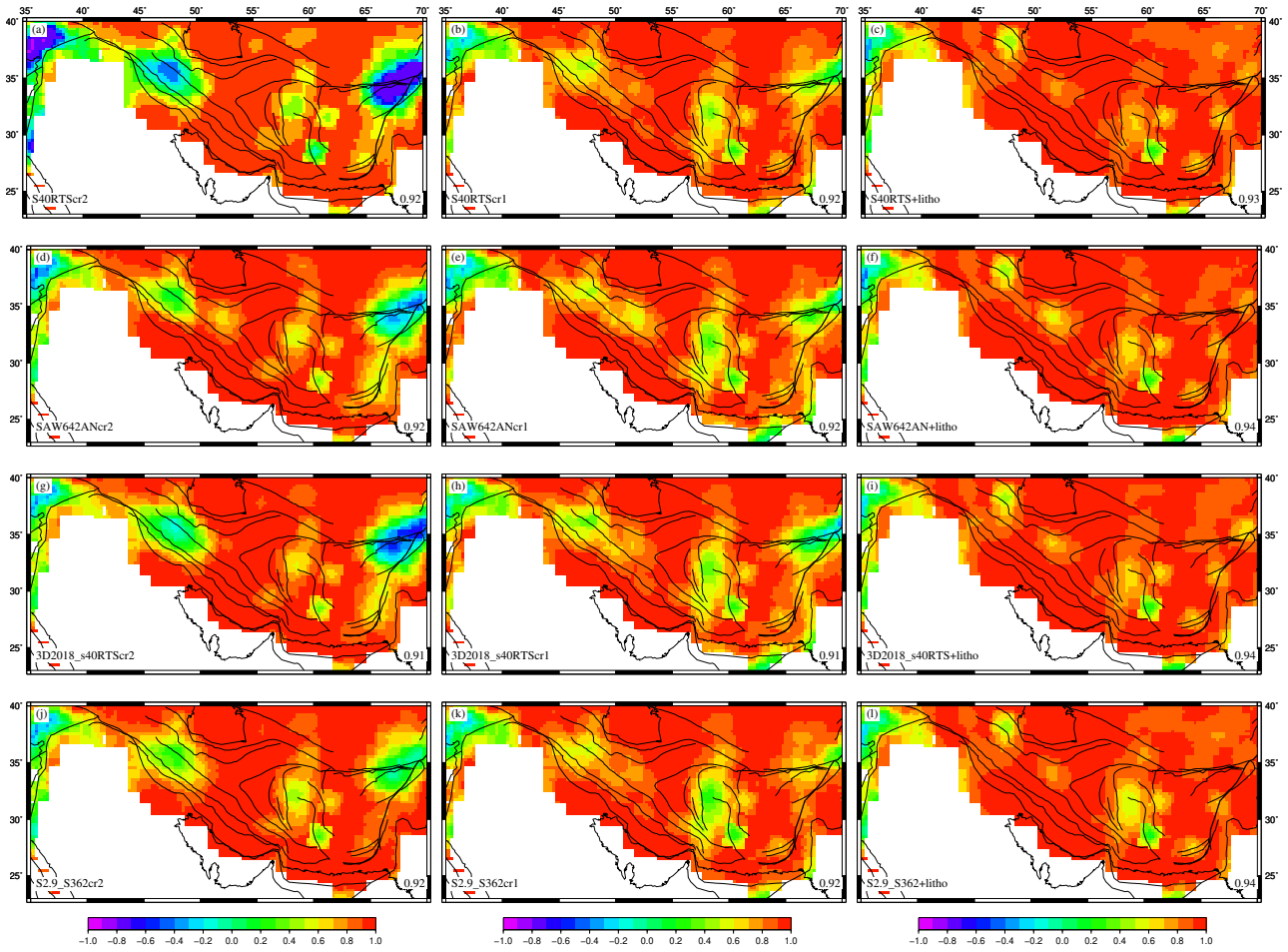
(a)
S40RTScr2
0.92
(b)
S40RTScr1
0.92
(c)
S40RTS+litho
0.93
(d)
SAW642ANcr2
0.92
(e)
SAW642ANcr1
0.92
(f)
SAW642AN+litho
0.94
(g)
3D2018_s40RTScr2
0.91
(h)
3D2018_s40RTScr1
0.91
(i)
3D2018_s40RTS+litho
0.94
(j)
S2.9_S362cr2
0.92
(k)
S2.9_S362cr1
0.92
(l)
S2.9_S362+litho
0.94
−1.0 −0.8 −0.6 −0.4 −0.2 0.0 0.2 0.4 0.6 0.8 1.0

Figure 13:

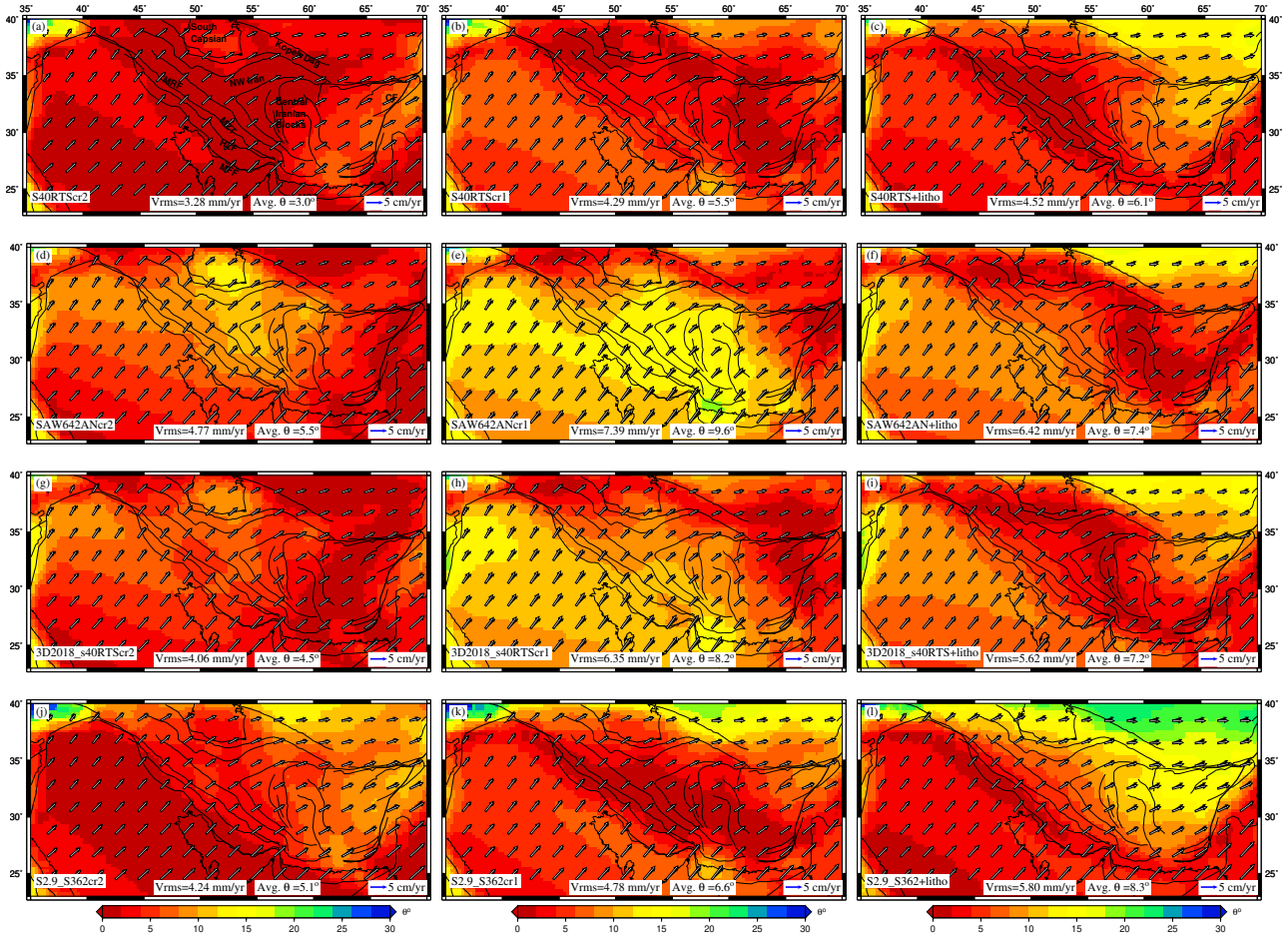
(a)
South Caspian
Tarim
NW Iran
Central Iranian Blocks
CF
S40RTScr2
Vrms=3.28 mm/yr
Avg. θ =3.0°
5 cm/yr
(b)
S40RTScr1
Vrms=4.29 mm/yr
Avg. θ =5.5°
5 cm/yr
(c)
S40RTS+litho
Vrms=4.52 mm/yr
Avg. θ =6.1°
5 cm/yr
(d)
SAW642ANcr2
Vrms=4.77 mm/yr
Avg. θ =5.5°
5 cm/yr
(e)
SAW642ANcr1
Vrms=7.39 mm/yr
Avg. θ =9.6°
5 cm/yr
(f)
SAW642AN+litho
Vrms=6.42 mm/yr
Avg. θ =7.4°
5 cm/yr
(g)
3D2018_s40RTScr2
Vrms=4.06 mm/yr
Avg. θ =4.5°
5 cm/yr
(h)
3D2018_s40RTScr1
Vrms=6.35 mm/yr
Avg. θ =8.2°
5 cm/yr
(i)
3D2018_s40RTS+litho
Vrms=5.62 mm/yr
Avg. θ =7.2°
5 cm/yr
(j)
S2.9_S362cr2
Vrms=4.24 mm/yr
Avg. θ =5.1°
5 cm/yr
(k)
S2.9_S362cr1
Vrms=4.78 mm/yr
Avg. θ =6.6°
5 cm/yr
(l)
S2.9_S362+litho
Vrms=5.80 mm/yr
Avg. θ =8.3°
5 cm/yr
θ°
0 5 10 15 20 25 30

Figure 14:

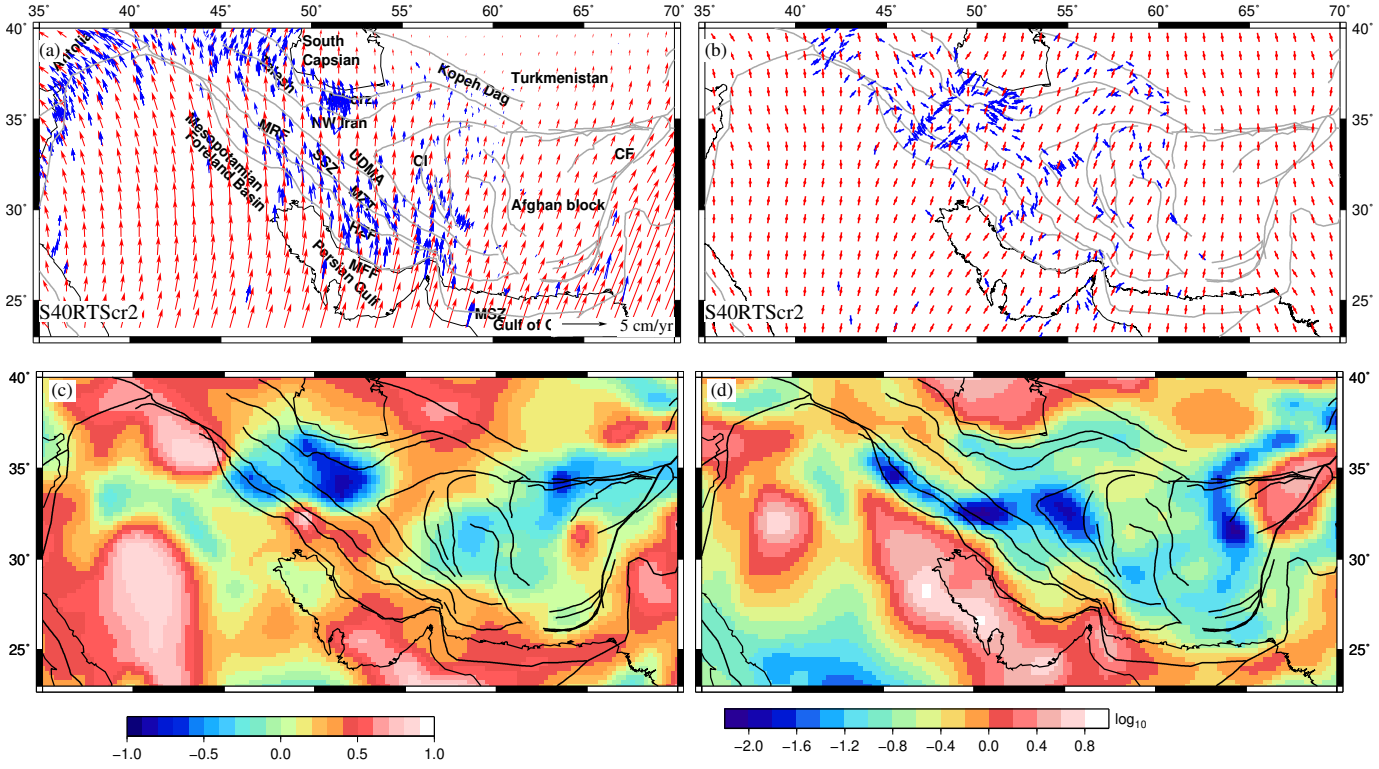
(a)
(b)
(c)
(d)
S40RTScr2
S40RTScr2
South Capsian
Turkmenistan
Kopeh Dag
NW Iran
MRF
SSZ
DDMA
CI
CF
Afghan block
MFF
Persian Gulf
MSZ
Mesopotamian Foreland Basin
5 cm/yr
−1.0 −0.5 0.0 0.5 1.0
−2.0 −1.6 −1.2 −0.8 −0.4 0.0 0.4 0.8
log10

# Numerical modelling of stresses and deformation in Zagros-Iranian plateau region

Srishti Singh[1] and Radheshyam Yadav[1]

[1]*CSIR-National Geophysical Research Institute, Hyderabad, India-500007*

## Key Points

- We have computed stresses and deformation of Zagros-Iran region with finite element modelling.
- Lithospheric stresses play an important role in the east of Iran.
- The joint models of lithosphere and mantle convection are able to explain various deformation indicators in the study area.

**Abstract**

Zagros Orogeny System resulted due to collision of the Arabian with Eurasia. The region has the ocean-continent subduction and continent-continent collision; and convergence velocity shows variation from east to west. Therefore, this region shows the complex tectonic stress and a wide range of diffuse or localized deformation between both plates. The in-situ stress and GPS data are very limited in this region, therefore, we performed a numerical simulation of the stresses causing deformation in the Zagros-Iran region. The deviatoric stresses resulting from the variations in lithospheric density and thickness; and those from shear tractions at the base of lithosphere due to mantle convection were computed using thin-sheet approximation. Surface observations of strain rates, $SH_{max}$, plate velocities etc. are explained using the joint models of lithosphere and mantle, suggesting a good coupling between lithosphere and mantle in most parts of Zagros and Iran. However, the deformation in east of Iran is caused primarily by lithospheric stresses. Plate motion of Arabian plate is found to vary along the Zagros belt from north-northeast in south-east of Zagros, north in central Zagros to slight northwest in northwestern Zagros. The out put of this study can be used in seismic hazards estimations.

***Keywords-*** Stress field, Gravitational Potential Energy, Mantle convection, Zagros, collision

# Plain Language Summary

We used numerical models to study the stresses causing deformation in the Zagros-Iran region. The stresses are generated due to variations in the density and topography of the lithosphere, which were computed through Gravitational potential energy (GPE) difference. Mantle convection produces shear tractions that are also an important source of stresses causing deformation. Different models of crustal structure and density of lithosphere give varying GPE, thus leading to different interpretations of the type of deformation in the study area. On the other hand, all mantle convection models in our study predicted consistent deviatoric stresses and were able to explain most observations of $SH_{max}$, plate velocities, and strain rates. Despite this, the lithosphere plays an important role in driving deformation, especially in the east of Iran. Overall, the lithospheric stresses when combined with those from mantle convection gave the best fit to the observed data.

# 1 Introduction

Zagros mountains are a part of Alpine-Himalayan belts that originated due to Arabian plate colliding with southern boundary of Eurasia. This collision resulted in closing of the Neotethys Ocean. The Zagros mountains extend from the eastern part of the Anatolia for over 1500 km in the NW-SE direction till the Makran subduction zone, showing large-scale diffuse deformation. Though there has been an increase in the influx of various studies trying to constrain the active deformation and kinematics of Zagros orogen (Allen et al., 2011; Reilinger et al., 2010; Le Dortz et al., 2009; Vernant et al., 2004; Walker, 2006), there are debates about various processes in this region, e.g. the timing of collision. Various authors (Jolivet & Faccenna, 2000; Agard et al., 2005; Vincent et al., 2005; Ballato et al., 2011) have suggested that collision onset time to be in Late Eocene to Oligocene; however, Ghalamghash et al. (2009); Mazhari et al. (2009) have argued Late Palaeocene or Early Eocene for the onset of collision. The Zagros and its foreland area have a great source of natural resources like petroleum. The study area consists of the ocean-continent subduction as well as the continental collisions. The convergence rate of the Arabian plate relative to the Eurasia varies from east to west. These complex structures and convergence velocity variation made the variable tectonic stress and deformation. The geophysical, geological and geodesy studies show that these areas are seismic active based on the earthquake data, fault slip rates and GPS velocities, which is related to the complex stress field in this region. Therefore, the world stress map (WSM) provides in-situ stress measurement and the compilation from the focal mechanism, hydrofracturing, and borehole breakout. However, the in-situ stress (WSM) and GPS velocity data (ArRajehi et al., 2010; Bayer et al., 2006; Frohling & Szeliga, 2016; Khorrami et al., 2019; Masson et al., 2006, 2007; Raeesi et al., 2017; Reilinger & McClusky, 2011; Vernant et al., 2004) are

very limited and sparsely distributed in this region; therefore, there is need for a numerical simulation study to comprehend the knowledge.

Although numerical modelling of tectonic stress and deformation was conducted in two approaches (1) using 2D and 3D geometrical structure, plate boundary forces like ridge push, slab pull and continents collision forces and rheological properties like Young's modulus, Poisson's ratio, viscosity, density etc. (Dyksterhuis & Müller, 2008; Coblentz et al., 1994; Koptev & Ershov, 2010; Richardson et al., 1976; Yadav & Tiwari, 2018), and, (2) considering Gravitational Potential energy and shear tractions from mantle convection with thin sheet approximation (Bird, 1998; Lithgow-Bertelloni & Guynn, 2004; Flesch et al., 2001; Ghosh & Holt, 2012; Singh & Ghosh, 2020). Stress studies showed that it's classified by the first, second and third order on the spatial scale (Zoback, 1992; Heidbach et al., 2007). The first-order stresses are originated due to the plate boundaries force like ridge push, slab pull and continental collisional; and second order stress by the rifting, isostasy and deglaciation. Moreover, third-order stress are caused by local sources like interaction faults systems, topography and density heterogeneity.

There are numerical studies conducted for tectonic stresses and deformation in Zagro-Iranian region (Austermann & Iaffaldano, 2013; Md & Ryuichi, 2010; François et al., 2014; Khodaverdian et al., 2015; Vernant & Chéry, 2006; Yamato et al., 2011). Md & Ryuichi (2010) modelled the maximum horizontal compressive stress ($SH_{max}$) orientations and showed N-S/NNE-SSW oriented $SH_{max}$ in Lurestan and eastern Zagros Simple Folded Belt, whereas they were aligned in NW-SE directions around Main Recent fault (MRF) and in northern High Zagros Faults (HZF). Sobouti & Arkani-Hamed (1996) reproduced observed faulting patterns by considering highly rigid central Iran and South Caspian Sea using a viscous thin-sheet approximation. Further, the kinematic model by Khodaverdian et al. (2015) procided constraints on fault slip rates, plate velocities and seismicity of the Iranian Plateau. The previous models did not include the mantle convections derived shear tractions for computation of deformation and stress in the Zagros-Iran regions.

In this study, we investigate the stress and deformation in Zagros-Iranian Plateau region to constrain the forces acting in this region with gravitational potential energy (GPE) and shear traction of mantle tractions. We will use a thin viscous sheet model based on Flesch et al. (2001) to compute various deformation parameters such as deviatoric stresses, strain rates, most compressive principal stress (SHmax), and plate velocities within the Zagros-Iran region.

# 2 Tectonic and Geology

The rise of Zagros mountain belt is a direct consequence of continental collision between Arabia and Eurasia. Zagros are located at the northeastern margin of the Arabian plate, trending in southwest

direction (Figure 1). It is bounded by the Main Zagros thrust (MZT) in northeast, while it joins the Tauras mountains in southern Turkey in the northwest. In the southeast, N-S trending Minab-Zandan fault zone separates Zagros from the Makran range. Outer Zagros are the young folded mountains in the southwest parts of the orogeny (Falcon, 1974; Sattarzadeh et al., 2002). High Zagros fault (HZF) separates highly deformed metamorphic rocks of inner Zagros from Simply folded mountains of outer Zagros (Hatzfeld & Molnar, 2010; Hatzfeld et al., 2010). Inner Zagros are bounded by MZT in northeast and are dominated by thrust faulting, possibly due to compression during the Late Cretaceous (Alavi, 1980). The northwestern Zagros are separated from central Zagros by a north-south trending strike-slip zone of deformation, known as Kazerun Fault System (KFS) (Authemayou et al., 2005).

Zagros mountains were formed between 35 and 23 Ma due to the convergence of Arabian platform beneath central Iranian crust. Arabian plate moves towards Eurasia with a plate velocity of 22-35 mm/yr (DeMets et al., 1990; McClusky et al., 2000; Jackson et al., 2002; Reilinger et al., 2006) in N-S to NNE direction. Zagros muntain belt is also accompanied by a zone of widespread deformation in the form of the high plateaus of Iran. Numerous earthquakes occur in these high terrains due to sustained tectonic activities; hence, these areas are prone to large seismic hazards.

During the last few decades, various geophysical surveys (receiver functions, deep seismic, GPS and tomographic studies) have been carried out in the Zagros-Iran region to investigate the deformation in this region. The southeastern Zagros accomodate the convergence between Arabia and Eurasia by pure shortening occuring through high-angle ($30^\circ - 60^\circ$) reverse faults that are prependicular to the belt (Hessami et al., 2006; Irandoust et al., 2022; Walpersdorf et al., 2006). On the other hand, oblique convergence in central and northern Zagros is partitioned into a strike-slip component that is accomodated on MRF and shortening occuring across the belt (Jackson et al., 2002; Talebian & Jackson, 2002). Zagros is separated from Makran subduction zone (MSZ) by Minab-Zendan-Palami (MZP) fault ($54^\circ - 58^\circ E$), which is a right-lateral strike-slip fault (Bayer et al., 2006). East of MZP shows significant shortening that is accomodated through the subduction in MSZ. Due to the difference between convergence rates, a shearing occurs in eastern Iran which is accomodated by the N-S trending faults bounding the Lut block. In northern Iran, fold and thrust belt of Alborz accomodates a quarter of Arabia-Eurasia convergence Irandoust et al. (2022). The oblique convergence in eastern Alborz is also partitioned into shortening at the southern boundary and a left-lateral component across the mountain belt (Irandoust et al., 2022; Khorrami et al., 2019; Tatar & Hatzfeld, 2009). Alborz mountains extend into Talesh in west which show thrust faulting on nearly flat faults. Kopeh-Dagh range in northeast accomodates the Arabia-Eurasia convergence through N-S shortening on major thrust faults in south.

# 3 Modelling

## 3.1 Equations

To model the stresses causing deformation in the Zagros-Iranian plateau due to Arabia-Eurasia collision, we solve three-dimensional (3D) force balance equations, considering the thin sheet approximation.

$$\frac{\partial \sigma_{ij}}{\partial x_j} + \rho g_i = 0 \tag{1}$$

Here $\sigma_{ij}$, $x_j$, $\rho$, and $g_i$ indicate the $ij^{th}$ component of the total stress tensor, $j^{th}$ coordinate axis, density and acceleration due to gravity respectively (England & Molnar, 1997; Ghosh et al., 2013b).

In the above equation, total stress, $\sigma_{ij}$ is substituted by deviatoric stress using the following relation:

$$\tau_{ij} = \sigma_{ij} - \frac{1}{3}\sigma_{kk}\delta_{ij} \tag{2}$$

In the above equation, the Kronecker delta and mean stress are denoted by $\delta_{ij}$ and $\frac{1}{3}\sigma_{kk}$ respectively. The force balance equation (1) is integrated up to the base of lithospheric sheet (L), resulting in following full horizontal force balance equations:

$$\frac{\partial \overline{\tau}_{xx}}{\partial x} - \frac{\partial \overline{\tau}_{zz}}{\partial x} + \frac{\partial \overline{\tau}_{xy}}{\partial y} = -\frac{\partial \overline{\sigma}_{zz}}{\partial x} + \tau_{xz}(L) \tag{3}$$

$$\frac{\partial \overline{\tau}_{yx}}{\partial x} + \frac{\partial \overline{\tau}_{yy}}{\partial y} - \frac{\partial \overline{\tau}_{zz}}{\partial y} = -\frac{\partial \overline{\sigma}_{zz}}{\partial y} + \tau_{yz}(L) \tag{4}$$

In equation (3) and (4), the over bars indicate integration over depth. Both equations (3 and 4) contain the first term representing horizontal gradients of GPE per unit area in right hand side. On the other hand, the shear tractions at the lithosphere base ($L$) arising due to mantle convection are denoted by $\tau_{xz}(L)$ and $\tau_{yz}(L)$ (Ghosh et al., 2009).

Both of the force balance equations (3 & 4) were solved using finite element technique (Flesch et al., 2001; Ghosh et al., 2009, 2013b; Singh & Ghosh, 2019, 2020). After solving these equations, we obtained the horizontal deviatoric stresses, $SH_{max}$, strain rates as well as plate velocities and compared them with observations.

The quantitative comparison between predicted and observed $SH_{max}$ axes (Figure 3a) was performed by computing the misfit given by $sin\theta(1+R)$ (Ghosh et al., 2013a; Singh & Ghosh, 2019, 2020), where R represents the quantitative difference between stress regimes of observed and predicted $SH_{max}$, while $\theta$ denotes the angular difference between both. Hence, this misfit accounts for both the angular and regime misfits with values lying between 0 and 3.

The correlation between predicted deviatoric stresses and GSRM strain rates (Figure 3b) (Flesch et al., 2007; Ghosh et al., 2013b; Singh & Ghosh, 2019, 2020) is given by following equation:

$$-1 \leq \sum_{areas} (\varepsilon.\tau)\Delta S / \left( \sqrt{\sum_{areas} (E^2)\Delta S} * \sqrt{\sum_{areas} (T^2)\Delta S} \right) \leq 1 \quad (5)$$

where $E = \sqrt{\dot{\varepsilon}_{\phi\phi}^2 + \dot{\varepsilon}_{\theta\theta}^2 + \dot{\varepsilon}_{rr}^2 + \dot{\varepsilon}_{\phi\theta}^2 + \dot{\varepsilon}_{\theta\phi}^2} = \sqrt{2\dot{\varepsilon}_{\phi\phi}^2 + 2\dot{\varepsilon}_{\phi\phi}\dot{\varepsilon}_{\theta\theta} + 2\dot{\varepsilon}_{\theta\theta}^2 + 2\dot{\varepsilon}_{\phi\theta}^2}$, $T = \sqrt{\tau_{\phi\phi}^2 + \tau_{\theta\theta}^2 + \tau_{rr}^2 + \tau_{\phi\theta}^2 + \tau_{\theta\phi}^2} = \sqrt{2\tau_{\phi\phi}^2 + 2\tau_{\phi\phi}\tau_{\theta\theta} + 2\tau_{\theta\theta}^2 + 2\tau_{\phi\theta}^2}$, and $\varepsilon.\tau = 2\dot{\varepsilon}_{\phi\phi}\tau_{\phi\phi} + \dot{\varepsilon}_{\phi\phi}\tau_{\theta\theta} + \dot{\varepsilon}_{\theta\theta}\tau_{\phi\phi} + 2\dot{\varepsilon}_{\theta\theta}\tau_{\theta\theta} + 2\dot{\varepsilon}_{\phi\theta}\tau_{\phi\theta}$. In the above equation, the second invariants of the strain rate and stress tensors are denoted by $E$ and $T$. GSRM strain rates, area and predicted deviatoric stresses are represented by $\dot{\varepsilon}_{ij}$, $\Delta S$, and $\tau_{ij}$ respectively. To constrain the plate valocities, we compute RMS as well as angular misfit between observed and predicted plate velcoities.

## 3.2 Crustal Models

In the right hand side of equations (3 & 4), the first term represents the vertically integrated vertical stress. It is computed and integrated from the top of variable topography up to depth L (100 km) (England & Molnar, 1997; Flesch et al., 2001; Ghosh et al., 2013b; Singh & Ghosh, 2019, 2020) using following relation:

$$\overline{\sigma}_{zz} = -\int_{-h}^{L} \left[ \int_{-h}^{z} \rho(z') g dz' \right] dz = -\int_{-h}^{L} (L - z)\rho(z) g dz \quad (6)$$

where $\rho(z)$, $L$ and $h$ denote density, the depth to the lithosphere base (100 km) and topographic elevation respectively. $z$ & $z'$ are variables of integration and $g$ represents the acceleration due to gravity.

The right hand side of equation 6 is given by negative of GPE per unit area. To calculate GPE and the stresses associated with it, we used three different global crustal models, CRUST2.0, CRUST1.0 and LITHO1.0. The upper crust thickness lies within 15-20 km in the Zagros-Iran region for CRUST2 model (Figure 2a). However, the thickness of the upper crust in the Zagros-Iranian region is much higher for CRUST1 and LITHO ($>$ 25 km) (Figure 2b & c). The Zagros-Iran region has a thicker middle crust ($>$ 20 km) in case of both CRUST2 and LITHO models (Figure 2d & f), while CRUST1 shows a much thinner middle crust ($<$ 12 km) in this region (Figure 2e). The lower crust in the Zagros-Iran region is found to be very thin ($<$ 10 km) for all three models (Figure 2g-i).

The density variations in the study area are minimal for CRUST2 model. CRUST2 also shows the highest average density in all three layers ($>$2.7 $g/cm^3$) (Figure 2j,m,p). CRUST1 also indicates an average density of $\sim 2.72/cm^3$ in the Zagros-Iran region for the upper crust (Figure 2k). The middle and lower crustal layers of CRUST1 show average densities of $2.80 g/cm^3$ and $\sim 2.85 g/cm^3$, respectively (Figure 2n,q). LITHO model shows the lowest average density in the study area for all three layers

(Figure 2l,o,r). The upper crust of LITHO models shows an average density of $2.65 g/cm^3$. Central Iran block has relatively denser upper crust ($\sim 2.75 g/cm^3$), while the density decreases to $\sim 2.62 - 2.64 g/cm^3$ near Zagros region. Similar patterns of density variations are observed in the middle and lower crust of LITHO model ((Figure 2o,r). Such differences in thickness and density data lead to varying GPE values, and hence subsequently, different stresses.

## 3.3 Mantle Convection

We ran mantle convection models using HC (Hager & O'Connell, 1981). HC is a semi-analytical mantle convection code that uses density anomalies derived from seismic tomography models and radial viscosity as inputs. Here, we considered four global mantle convection models, S40RTS (Ritsema et al., 2011), SAW642AN (Mégnin & Romanowicz, 2000), 3D2018_S40RTS and S2.9_S362 to infer the mantle density anomalies. 3D2018_S40RTS is a merged model of SV wave upper mantle tomography model, 3D2018_Sv given by Debayle et al. (2016), and S40RTS. S2.9 is a global tomography model of upper mantle with higher resolution which is given by Kustowski et al. (2008b). We merged this model with the global shear wave velocity model, S362ANI (Kustowski et al., 2008a) to obtain merged tomography model of S2.9_S362. The radial viscosity model, GHW13 which is the best viscosity structure given by Ghosh et al. (2013b) was used in our study to run mantle convection models.

## 3.4 Data

To have better constraints on our models, we also estimated $SH_{max}$(most compressive horizontal principal axes) orientations as well as plate velocities. Various deformation indicators such as $SH_{max}$ orientations from the World Stress Map (WSM) (Heidbach et al., 2016), strain rates and plate velocities from Global Strain Rate Model (Kreemer et al., 2014) were used to perform a quatitative comparison with our predicted results (Figure 3).

WSM data is a global database of the crustal stress field obtained from various sources such as focal mechanism; geophysical logs of borehole breakouts and drilled induced fractures; engineering methods such as hydraulic fractures and overcoring; and geological indicators that are obtained from fault slip analysis and volcanic alignments. These data have been assigned quality ranks from A to E based on the accuracy range. A-type data suggests that the standard deviations of $SH_{max}$ orientations are within $\pm 15^\circ$ range, $\pm 20^\circ$ for B-type, $\pm 25^\circ$ for C-type and $\pm 40^\circ$ for D-type. However, E-type indicates the data records are either incomplete or from non-reliable sources or the accuracy is $> \pm 40^\circ$. Our study uses A-C quality stress data records (Figure 3a). Observed $SH_{max}$ axes are aligned in NNE-SSW directions in Zagros with dominant thrust faulting. NW and Central Iran shows some strike-slip mode of deformation

with NE-SW compressional directions.

The strain rates and plate velocities are taken from GSRM v2.1 model (Kreemer et al., 2014) (Figure 3b). GSRM v2.1 provides a global data set of strain rates and plate motions that are determined using $\sim 22,500$ geodetic plate velocities. Higher strain rates are observed along simple folded mountains ($\sim 40-100\times10^{-9}/yr$). Most of Iran shows strain rates in between $4-10\times10^{-9}/yr$. The plate motions used in our study for comparing with predicted velocities are given in a no-net-rotation (NNR) frame interpolated on a $1^{\circ}\times1^{\circ}$ grid. The velocity vectors show an eastward motion in the study area, which becomes nearly E-W in Afghan Block (Figure 3b).

# 4 Results

## 4.1 Stress and deformation due to GPE

Three crustal models (CRUST1.0, CRUST2.0 and LITHO1.0) were used to compute GPE within the study region. The second invariant of stress computed using GPE lies within $\sim$10-12 MPa along the Zagros for CRUST2 and CRUST1 models (Figure 4a,c). LITHO model predicts larger stress magnitudes along Zagros (Figure 4e). NE-SW compressional stresses are observed along the frontal faults of Zagros (MFF) (Figure 1a,c). The central part of Zagros thrust faults (MZT) shows the strike-slip mode of faulting for nearly all three models (Figure 4 & 4b,d & f). The strike-slip regime further extends into Sanandaj-Sirjan Zone (SSZ) while lies north of MZT for CRUST2 and LITHO model (Figure 4b,f), while it transitions to thrust type of deformation in the north of MZT for CRUST1 (Figure 4d). The Urmia-Dokhtar Magmatic Arc (UDMA) and central Iran also show strike-slip mode of faulting for CRUST2 and LITHO. The north of MRF shows tension for CRUST2 model, while CRUST1 predicts this area to be predominantly strike-slip. On the other hand, the entire region shows significant compression for LITHO model.

We compared predicted $SH_{max}$ from our three GPE only models to observed $SH_{max}$ orientations and type obtained from WSM (Heidbach et al., 2016) by computing Regime misfit (Figure 5, left panel). The average misfit is lowest for LITHO model with a value of 0.59 (Figure 5g), while CRUST2 model shows the highest average misfit of 0.77 (Figure 5a). High misfits ($2-3$) are observed in North of MRF and Tehran for CRUST2, while lowest ($<1$) in case of LITHO, suggesting that the dominant mode of faulting in this area is possibly thrust as opposed to normal deformation predicted by CRUST2. In central Iran, $SH_{max}$ misfit is low ($<1$) when the dominant mode of deformation is strike-slip as predicted LITHO model.

On calculating the correlation between the predicted deviatoric stresses and GSRM strain rates, the LITHO model shows the highest average correlation (0.92) (Figure 5, middle panel). The correlation

is found to be extremely poor ($\sim -1$) for CRUST2 model in the north of MRF (Figure 5b). Such poor correlation suggests that the predicted stresses differ entirely from those causing deformation. For example, anti-correlation in north of MRF suggests that the dominant mode of deformation in this area might be thrust rather than normal faulting. Again, the correlation coefficient is less than 0.2 in the central Iranian Block for CRUST2 and CRUST1 models (Figure 5b,e), while LITHO model shows a better correlation suggesting the strike-slip type of deformation to be more prominent in central Iran (Figure 5h).

We predicted the plate velocities for all three models in the NNR frame and compared them with observed plate velocities obtained from Kreemer et al. (2014) (Figure 5 right panel). CRUST2 gives the least RMS error (7.32 mm/yr) and lowest angular misfit (5.5°) (Figure 5c). LITHO model shows high misfits ($> 20°$) between observed and predicted velocities in the east of the central Iran (i.e. Afghan Block)(Figure 5i). Both CRUST2 and LITHO models predict the plate velocities very close to observed ones in the Zagros mountains, as shown by nearly zero angular misfits along Zagros (Figure 5c & i). CRUST1 performs average in predicting the plate velocities in the study area (Figure 5f).

## 4.2 Stress and deformation due to Mantle Convection

The deviatoric stresses predicted using all four mantle convection models are found to be mostly compressonal along MFF (Figure 6). All models, except for SAW642AN, predict the strike-slip mode of faulting in NW parts of Zagros with nearly E-W oriented extensional axes and N-S compressional axes (Figure 6a,e & g). On the other hand, SAW642AN shows predominant compression within this area (Figure 6e). S40RTS, 3D2018_Sv, and S2.9_S362 show strike-slip deformation in NW parts of SSZ, UDMA and NW Iran. Central Iran is predicted to have mostly compressional stresses by all models except for S40RTS. Thrust type of deformation is predicted in Afghan Block by all models with some intermittent strike-slip deformation. SINGH_SAW model predicts the whole Afghan Block in the strike-slip regime (Figure 6g-h). S40RTS and S2.9_S362 predict higher stress magnitude in NW parts of the Zagros Orogeny system and Central Iran compared to other models.

The misfit between observed and predicted $SH_{max}$ is found to be much lower for mantle convection models (0.54-0.57) (Figure 7 left panel), than those of GPE only models (Figure 5 left panel), evidently showing the importance of mantle flow. The lowest average misfit is observed for SAW642AN (0.54) (Figure 7d). Though the misfit increases in the east, Lut block and, near MSZ. The correlation of predicted deviatoric stresses with GSRM strain rates improves over GPE only models (Figure 7 middle panel), with SAW642AN yielding the highest correlation coefficient (0.91) (Figure 7e). Correlation drops below 0.4 parts of central Iran. S40RTS performs predicts the plate velocities closest to observed one, out of all models, with the least RMS error ( 6.20 mm/yr) between predicted and observed plate

velocities (Figure 7c). On the other hand, SAW642AN and 3D2018_S40RTS models show high misfits (rms error $\sim 10 mm/yr$), as they are unable to match observed plate velocities in Zagros-Iran plateau, both in orientations and magnitude (Figures 7f & i).

As discussed above, mantle convection models perform better in predicting deviatoric stresses in the study area. However, the error in predicting plate velocities is higher than in GPE only models. GPE only models perform slightly better in predicting the orientation and magnitude of velocity vectors. Thus, we add the deviatoric stresses predicted from GPE differences and Mantle convection models to constrain the stress field in Zagros-Iranian plateau that may account for both forces.

## 4.3 Stress and deformation by GPE and Mantle convection

Adding mantle contributions to GPE only models led to significant changes in total deviatoric stresses for all models (Figure 8,9,10). There is a significant increase in total stress magnitude of the entire study area; except for north of MRF and SE of central Iran, which show slightly lower stresses ($<$ 16 MPa) for combined models of CRUST2 and mantle convection (Figure 8). These models show predominant compression in most of Zagros, SSZ, UDMA, NW and central Iran, except for the strike-slip type of deformation in NW parts. The joint models of CRUST1 and mantle convection predict higher stresses ($>$ 25 MPa) in NW Iran and at MFF (Figure 9). Interestingly, the stresses drop below 20 MPa towards the north of HZF, MRF till the south Capsian. The combined models of CRUST1 and mantle convection show compressional stresses are dominant in the study area, with occasional strike-slip faulting in the north-west (Figure 9 right panel). The stresses predicted by combined models of LITHO and mantle convection models are higher in magnitude than other models in the study area ($>$ 25 MPa) (Figure 10). S40RTS+litho and S2.9_S362+litho models show high stresses in Zagros ($>$50 MPa)(Figure 10a,g).

The combined models show a lower misfit between observed and predicted $SH_{max}$ (Figure 11), especially when compared to GPE only models (Figure 5 left panel). SAW642AN+litho showed the lowest average misfit of 0.47 (Figure 11f). Interestingly, SAW642ANcr2 and 3D2018_S40RTScr2 show low misfits in the Zagros-Iranian plateau region, despite not having the lowest average misfit (Figure 11d & g). The higher misfits in NW Iran and SE of the central Iran block observed for GPE only models, get reduced significantly due to the addition of mantle derived stresses, referring to the importance of mantle convection in these areas.

As we look at the correlation between predicted stress tensors and GSRM strain rate tensors, the overall correlation is better for combined models (Figure 12), especially for combined models of LITHO and mantle convection (Figure 12 right panel). A high average correlation coefficient of 0.94 is observed for SAW642AN+litho, 3D2018_S40RTS+litho as well as S2.9_S362+litho (Figures 12f, i & l). Despite an overall improvement in correlation between observed strain tensors and predicted deviatoric stresses,

the correlation is found to be much poor in areas such as NW parts of Zagros and east of central Iranian block, for combined models of mantle convection and GPE only models of CRUST2 & CRUST1 (Figure 12 left and middle panels). In NW Zagros, mantle only models are found to perform much better, as they show better correlation (Figure 7 middle panel), thus suggesting mantle derived stresses are needed to be much higher than those from GPE to explain the observed deformation in these areas.

Again the combined models of GPE and mantle tractions give lower rms errors, when predicted plate velocities are compared to the observed ones. S40RTScr2 shows least rms error (3.28 mm/yr) and least average angular misfit (3.0°) between predicted and observed plate velocities (Figure 13a). Relatively the combined models of S40RTS/S2.9_S362 and GPE perform much better than other models in predicting the orientation and magnitudes of plate velocities. Significant misfits are observed for SAW642ANcr1 and 3D2018_S40RTScr1 models.

# 5 Discussion

The Zagros-Iranian plateau region is formed due to the convergence of Arabian plate towards Eurasia. Zagros mountain belt demarcates the southwestern boundary of the deformation zone, whereas, it is bounded by the Makran subduction zone in the southeast and by Afghan Block in the east. Kopet-Dagh and Arborz act as this region's northeastern and northern boundaries (Irandoust et al., 2022). We modeled the stresses and deformation parameters in the study area by solving the force balance equation using the finite element method for a global grid of $1^\circ \times 1^\circ$ resolutions, considering two primary sources of stresses; GPE and mantle tractions. GPE was calculated using the thickness and density variation from the different global models like CRUST1, CRUST2 and LITHO. The shear tractions were computed from density derived mantle convection model.

The magnitude of stresses due to GPE variations was below 15 MPa in the Iranian plateau for CRUST2 and CRUST1 models (Figure 4a & c). However, LITHO model predicted higher stresses ($> 30$ MPa) with predominant compression in parts of the Zagros-Iran region and Afghan block. Most of the convergence of Arabian and Eurasian plates has been accommodated through shortening across Zagros (Irandoust et al., 2022; Khodaverdian et al., 2015). Walpersdorf et al. (2006); Hessami et al. (2006) suggested nearly pure N-S shortening of $8 \pm 2 mm/yr$ in southeastern Zagros. The convergence occurs perpendicular to the Simply folded mountains and is restricted to the shore of Persian Gulf. Earthquake focal mechanisms also show reverse faulting within this area (Berberian, 1995; Hatzfeld et al., 2010; Hatzfeld & Molnar, 2010; Irandoust et al., 2022). In our study, LITHO model predicts thrust mode of faulting within Zagros, which is consistent with these results. In NW Zagros, Hatzfeld et al. (2010); Hatzfeld & Molnar (2010); Jackson & McKenzie (1984); Khorrami et al. (2019); Talebian & Jackson

(2002) and various others have suggested partitioning of deformation. The oblique shortening is partitioned into strike-slip faulting that is accommodated by MRF, while shortening occurs perpendicular to the the mountain belt (Hatzfeld et al., 2010; Hatzfeld & Molnar, 2010; Jackson & McKenzie, 1984; Khorrami et al., 2019; Talebian & Jackson, 2002). On considering lithospheric models only, we predicted normal mode of faulting to be dominant in this area for CRUST2. On the other hand, CRUST1 model predicted strike-slip components in the northern segment of MRF, while LITHO showed thrust type of deformation in this area. Interestingly, the misfits of predicted parameters with various observations of $SH_{max}$, strain rates and plate velocities were found to be lowest for LITHO model, thus arguing for thrust type of deformation in this area. SSZ in north of MZT consists of various thrust systems (Alavi, 1994). CRUST1 predicts thrust mode of faulting in this region, while CRUST2 and LITHO models show intermittent strike-slip type of faulting. Alborz as well as Kopet Dagh in north has also been subjected to reverse faulting (Allen et al., 2003; Hatzfeld & Molnar, 2010; Hollingsworth et al., 2010; Irandoust et al., 2022; Khodaverdian et al., 2015), which has also been shown by CRUST1 and LITHO models. Models predicting thrust in Talesh mountains show low misfits to observation suggesting thrusting of the mountain range over the basin with slip vectors directed towards the South Caspian Sea (Irandoust et al., 2022). The N-S convergence in Kopeh-Dagh range is predicted by LITHO model considering contribution from lithospheric density and topographic variations only. The shearing between Central Iran and Afghan Block caused due to varying rates of shortening across the Zagros, Alborz and Caucasus, is accommodated by strike-slip faults near Lut block boundaries (Khorrami et al., 2019; Vernant et al., 2004; Walpersdorf et al., 2014). Again, LITHO model predicted similar strike-slip deformation in these areas; however, CRUST2 and CRUST1 failed to do so.

The stresses predicted using basal tractions were mostly compressional in southeastern Zagros owing to the convergence of Arabia-Eurasia (Figure 6). However, all models, except SAW642AN predicted strike-slip type of deformation in the northwestern Zagros (MRF), which concurs with the results from various studies (Hatzfeld et al., 2010; Hatzfeld & Molnar, 2010; Jackson & McKenzie, 1984; Khorrami et al., 2019; Talebian & Jackson, 2002). The mantle derived stress parameters showed a better fit to observables than those from GPE variations (Figures 7 left and middle panel), though the correlation dropped below 0.5 in Central Iran. Here, mantle convection models predicted compressional type of deformation, while Baniadam et al. (2019); Khorrami et al. (2019) suggested that strike-slip faulting along the fault system bounding Lut Block. The velocity misfits were very high for all models except S40RTS (Figure 7 right panel). Although we used four tomography models to compute the mantle-derived stresses, the stress regimes for all models are found to be similar, with varying magnitudes. Such results suggest that nearly all four seismic tomography models are relatively consistent in predicting the stresses in this region.

Adding the GPE derived stresses to those from mantle to obtain the total lithospheric stress field showed a notable improvement in constraining the observed deformation parameters. The final stress regimes also varied significantly depending on particular combinations of GPE and mantle convection models. All joint models of CRUST2 and mantle tractions showed lower magnitudes of stresses ($< 15$ MPa) in north of MRF, Tehran and southern Lut block. The stresses showed an obvious increase in these areas for other models. Significantly higher stresses ($> 30$ MPa) were also observed near the collisional front (MFF) for all models. On comparing with observations, combined models of CRUST2 and mantle tractions showed significant improvement in fit, except in areas north of MRF and Tehran. CRUST1 model when added with mantle contribution, predicted thrust faulting along the faults bounding Lut Block, leading to poor correlation ($< 0.5$). On the other hand, combined LITHO and mantle convection models gave a much better fit in this area, as they predicted strike-slip faulting. The use of different mantle convection models is much less sensitive in the Iran-Zagros region, as most models can match various surface observables reasonably well.

On running various models and comparing the stresses in Zagros-Iran, we try to explain the relative roles of GPE and mantle tractions in causing observed deformation. The contributions from both sources vary significantly among different models. However, these variations arise mainly from GPE only models, which may be due to uncertainties in crustal models of this area. Another interesting observation from this study is that the role of GPE in the study region may not be that significant, as mantle derived stresses were able to explain many of the deformation indicators. To get a quantitative constraint on the best model, we computed a total error as given below:

$$Total\,error = SH_{max}\,error + 1 - C_{strain} + V_{rms} \tag{7}$$

$SH_{max}$ error in the above equation is calculated as mentioned in section 3.4, while $C_{strain}$ is the correlation computed using equation 6. $V_{rms}$ is the rms error between predicted and observed velocities. The total errors calculated using equation 7 have been tabulated in Table S1. S40RTScr2 is found to have lowest error.

We also calculated plate velocities with respect to the Eurasian plate (Figure 14) and compared them with observed GPS velocities relative to Eurasia. The GPS velocities were obtained from various studies conducted in the study area (ArRajehi et al., 2010; Bayer et al., 2006; Frohling & Szeliga, 2016; Khorrami et al., 2019; Masson et al., 2006, 2007; Raeesi et al., 2017; Reilinger & McClusky, 2011; Vernant et al., 2004). GPS measurements show a northward convergence rate of $\sim 22 mm/yr$ for Arabia relative to Eurasia (Reilinger et al., 2006; Vernant et al., 2004), however, it varies significantly along the Zagros. The southeastern Zagros show the highest convergence rates of $\sim 25$ mm/yr oriented in

north-northeast directions. GPS vectors are oriented northward in Central Zagros, which transitions north-northwest in NW parts of Zagros with the lowest convergence rates of $\sim$ 18 mm/yr (Hatzfeld & Molnar, 2010; Hatzfeld et al., 2010; Khorrami et al., 2019). Vernant et al. (2004) suggested that MSZ accommodates most of the shortening ($19.5 \pm 2$ mm/yr) in the east of $58^{\circ}E$, while fold and thrust belts of Zagros, Alborz and Caucasus collectively accomodate the shortening in west of $58^{\circ}E$. GPS velocities in east of Iran (Afghan Block) are very small in magnitude. To the west, velocities increase showing westward rotation of Antolia Khorrami et al. (2019); Reilinger et al. (2006). The northern part of Iran shows that GPS vectors are aligned towards the northeast. We found that the combined model of S40RTS and CRUST2 can approximately match the GPS velocities (Figure 14a). Predicted plate velocities with respect to the fixed Eurasian plate show a northward movement of 2-3 cm/yr in southeastern Zagros. The plate moves in NNE direction east of central Zagros (53° E). On the other hand, west of 53° E shows a movement in NNW direction, becoming much more prominent in the north. However, the convergence rates in east of Iran i.e. Lut Block as well as Afghan Block, is predicted to be much higher ($\sim 1 - 2cm/yr$) than those suggested by various observations. Plate velocities predicted by joint models, S40RTScr1 and S40RTS+litho show nearly N-S contraction of of very high magnitudes (4-5 cm/yr) throughout the region (Figure S1), which suggests much higher rates of deformation than those suggested by above mentioned studies.

We also used shear wave splitting measurements to further study the deformation in the Zagros-Iran region by comparing them with $SH_{max}$ (Figure 14b). The fast polarization directions (FPDs) are the indicators of seismic anisotropy. We consider two primary causes of seismic anisotropy; induced by stress and due to structure of the region (Yang et al., 2018). If the FPDs are parallel to $SH_{max}$ orientations, it suggests that anisotropy is associated with stress. On the other hand, latter kind of anisotropy is related with the alignment of fault, fast axes of minerals that may cause polarization, and sedimentary bedding planes. The FPDs in our study were obtained from Sadeghi-Bagherabadi et al. (2018); Kaviani et al. (2009, 2021). The FPDs are subparallel to $SH_{max}$ orientations in NW Zagros, Arabian plate, northern Iran and MSZ. Such a correlation between both indicates that anisotropy in this region may be stress induced. In NW Zagros, Sadeghi-Bagherabadi et al. (2018) also showed FPDs parallel to the strike of the fault, suggesting seismic anisotropy mainly reflect the deformation in the lithospheric mantle. Again, FPDs are subparallel to the strike of range in northeastern Iran, eastern Kopeh Dagh and central Alborz indicating structure-induced anisotropy caused by strong shearing along the strike-slip faults (Gao et al., 2022; Kaviani et al., 2021).

To explore the relative roles of lithospheric and mantle derived stresses, we compared the deviatoric stresses from CRUST2 to those from S40RTS. We performed a correlation between both stresses by using equation 5 and found a high correlation ($> 0.5$) near MSZ and central Zagros (Figure 14c).

The correlation degrades north of the simply folded mountains and NW Iran. The stresses are anti-correlated in parts of northwestern parts of higher Zagros, north of MRF and Tehran, as CRUST2 predicted NNE-SSW tension (Figure 4b) as opposed to the strike-slip faulting predicted by S40RTS (Figure 6b). Lut Block also shows a slight anticorrelation between stresses ($\sim -0.5$), as the stresses predicted by CRUST2 are very low. The log of the ratio of second invariants of deviatoric stresses from GPE variations ($T_1$) to that of mantle tractions ($T_2$) is plotted in Figure 14d. Positive values of logarithmic ratio suggests the dominance of GPE derived stresses over mantle ones, as observed in the south of the collisional boundary (MFF). The ratio is negative in most parts of the Iranian plateau and Zagros, indicating that the magnitude of mantle derived stresses are higher than those from GPE, especially in higher Zagros and central Iran (Figure 14d).

# 6 Conclusion

The Zagros-Iranian plateau region has large deformations along and across the collision zones. Therefore, we conduct numerical simulation studies for stress and deformations. The stresses predicted in this region were primarily compressional, with magnitudes lower than 30 MPa. The southeastern boundary of Zagros to be under high stress which is also reflected by higher convergence rates. Mantle convection models are able to constrain most observations in Iranian plateau. However, the misfits with observations are much larger in east of Iran, when only mantle contributions are considered. The combined models of lithospheric and mantle-derived stresses can give a better fit to surface observables in most of the area, suggesting a good lithosphere-mantle coupling, except for east of Iran. The fit between both predicted and observed data increases after considering mantle derived stresses. The shearing in those areas is predicted by lithospheric models, though variation in lithospheric and density structure given by these models lead to varying degree of misfits. Hence, there is a need for better contraint on lithospheric structure in this area.

The mantle derived stresses were found to be much higher than lithospheric stresses, thus the overall stress regimes predicted by combined models were more biased towards the compressional type of stresses. This caused our combined models to predict thrust mode of faulting in most cases, especially when lithospheric derived stresses were computed from CRUST1 and LITHO models. CRUST2 model predicted more extensional stress in Iranian plateau, which in turn balanced the effect of compressional stresses predicted by mantle convection models; hence leading to prominance of strike-slip model of faulting northwestern parts of study region. The rate of convergence of Arbia relative to a fixed Eurasia was found to vary along the Zagros orogeny in a similar way to GPS measurements.

# Open Research Section

We used three models, namely CRUST1.0, CRUST2.0, and LITHO1.0, for obtaining the data of crustal and lithospheric structure, which are required as inputs in finite element models. We downloaded these three models and the seismic tomography models used in mantle convection codes from the Incorporated Research Institutions for Seismology (IRIS) Earth Model Collaboration repository (`http://ds.iris.edu/ds/products/emc-earthmodels/`). The strain rate model, GSRMv2.1 was obtained from `http://geodesy.unr.edu/GSRM/`. World Stress Map Website (`https://www.world-stress-map.org/`) provides the $SH_{max}$ orientations and type of faulting, which were used to perform a quantitative comparison with predicted results. GPS velocities relative to Eurasia were taken from ArRajehi et al. (2010); Bayer et al. (2006); Frohling & Szeliga (2016); Khorrami et al. (2019); Masson et al. (2006, 2007); Raeesi et al. (2017); Reilinger & McClusky (2011); Vernant et al. (2004). We also used seismic anisotropy data from Sadeghi-Bagherabadi et al. (2018); Kaviani et al. (2009, 2021).

# Acknowledgments

We are grateful to Dr. Attreyee Ghosh for sharing the codes for finite element modelling of stresses. We thank the director CSIR-NGRI for permission to publish this work (Ref. No. NGRI/Lib/2022/ Pub-110). This article is published as a part of MLP-FBR-003(AM) Project. The figures of this article are generated from gmt.

# References

Agard, P., Omrani, J., Jolivet, L., & Mouthereau, F. (2005). Convergence history across Zagros (Iran): constraints from collisional and earlier deformation. *International journal of earth sciences*, *94*(3), 401–419.

Alavi, M. (1980). Tectonostratigraphic evolution of the Zagrosides of Iran. *Geology*, *8*(3), 144–149.

Alavi, M. (1994). Tectonics of the Zagros orogenic belt of Iran: new data and interpretations. *Tectonophysics*, *229*(3-4), 211–238.

Allen, M., Ghassemi, M., Shahrabi, M., & Qorashi, M. (2003). Accommodation of late Cenozoic oblique shortening in the Alborz range, northern Iran. *Journal of structural geology*, *25*(5), 659–672.

Allen, M.B., Kheirkhah, M., Emami, M.H., & Jones, S.J. (2011). Right-lateral shear across Iran and

kinematic change in the Arabia—Eurasia collision zone. *Geophysical Journal International*, *184*(2), 555–574.

ArRajehi, A., McClusky, S., Reilinger, R., Daoud, M., Alchalbi, A., Ergintav, S., Gomez, F., Sholan, J., Bou-Rabee, F., Ogubazghi, G., et al. (2010). Geodetic constraints on present-day motion of the Arabian Plate: Implications for Red Sea and Gulf of Aden rifting. *Tectonics*, *29*(3).

Austermann, J. & Iaffaldano, G. (2013). The role of the Zagros orogeny in slowing down Arabia-Eurasia convergence since˜ 5 Ma. *Tectonics*, *32*(3), 351–363.

Authemayou, C., Bellier, O., Chardon, D., Malekzade, Z., & Abassi, M. (2005). Role of the Kazerun fault system in active deformation of the Zagros fold-and-thrust belt (Iran). *Comptes Rendus Geoscience*, *337*(5), 539–545.

Ballato, P., Uba, C.E., Landgraf, A., Strecker, M.R., Sudo, M., Stockli, D.F., Friedrich, A., & Tabatabaei, S.H. (2011). Arabia-Eurasia continental collision: Insights from late Tertiary foreland-basin evolution in the Alborz Mountains, northern Iran. *Bulletin*, *123*(1-2), 106–131.

Baniadam, F., Shabanian, E., & Bellier, O. (2019). The kinematics of the Dasht-e Bayaz earthquake fault during Pliocene-Quaternary: implications for the tectonics of eastern Central Iran. *Tectonophysics*, *772*, 228218.

Bayer, R., Chery, J., Tatar, M., Vernant, P., Abbassi, M., Masson, F., Nilforoushan, F., Doerflinger, E., Regard, V., & Bellier, O. (2006). Active deformation in Zagros—Makran transition zone inferred from GPS measurements. *Geophysical Journal International*, *165*(1), 373–381.

Berberian, M. (1995). Master "blind" thrust faults hidden under the Zagros folds: active basement tectonics and surface morphotectonics. *Tectonophysics*, *241*(3-4), 193–224.

Bird, P. (1998). Testing hypotheses on plate-driving mechanisms with global lithosphere models including topography, thermal structure, and faults. *Journal of Geophysical Research: Solid Earth*, *103*(B5), 10115–10129.

Coblentz, D., Richardson, R.M., & Sandiford, M. (1994). On the gravitational potential of the Earth's lithosphere. *Tectonics*, *13*(4), 929–945.

Debayle, E., Dubuffet, F., & Durand, S. (2016). An automatically updated S-wave model of the upper mantle and the depth extent of azimuthal anisotropy. *Geophysical Research Letters*, *43*(2), 674–682.

DeMets, C., Gordon, R.G., Argus, D., & Stein, S. (1990). Current plate motions. *Geophysical journal international*, *101*(2), 425–478.

Dyksterhuis, S. & Müller, R. (2008). Cause and evolution of intraplate orogeny in Australia. *Geology*, *36*(6), 495–498.

England, P. & Molnar, P. (1997). Active deformation of Asia: From kinematics to dynamics. *Science*, *278*(5338), 647–650.

Falcon, N.L. (1974). Southern Iran: Zagros Mountains. *Geological Society, London, Special Publications*, *4*(1), 199–211.

Flesch, L.M., Haines, A.J., & Holt, W.E. (2001). Dynamics of the India-Eurasia collision zone. *Journal of Geophysical Research*, *106*(B8), 16435–16460.

Flesch, L.M., Holt, W.E., Haines, A.J., Wen, L., & Shen-Tu, B. (2007). The dynamics of western North America: stress magnitudes and the relative role of gravitational potential energy, plate interaction at the boundary and basal tractions. *Geophysical Journal International*, *169*(3), 866–896.

François, T., Burov, E., Agard, P., & Meyer, B. (2014). Buildup of a dynamically supported orogenic plateau: Numerical modeling of the Zagros/Central Iran case study. *Geochemistry, Geophysics, Geosystems*, *15*(6), 2632–2654.

Frohling, E. & Szeliga, W. (2016). GPS constraints on interplate locking within the Makran subduction zone. *Geophysical Supplements to the Monthly Notices of the Royal Astronomical Society*, *205*(1), 67–76.

Gao, Y., Chen, L., Talebian, M., Wu, Z., Wang, X., Lan, H., Ai, Y., Jiang, M., Hou, G., Khatib, M.M., et al. (2022). Nature and structural heterogeneities of the lithosphere control the continental deformation in the northeastern and eastern Iranian plateau as revealed by shear-wave splitting observations. *Earth and Planetary Science Letters*, *578*, 117284.

Ghalamghash, J., Bouchez, J., Vosoughi-Abedini, M., & Nédélec, A. (2009). The Urumieh Plutonic Complex (NW Iran): Record of the geodynamic evolution of the Sanandaj–Sirjan zone during Cretaceous times–Part II: Magnetic fabrics and plate tectonic reconstruction. *Journal of Asian Earth Sciences*, *36*(4-5), 303–317.

Ghosh, A., Becker, T.W., & Humphreys, E.D. (2013a). Dynamics of the North American continent. *Geophysical Journal International*, *194*(2), 651–669.

Ghosh, A. & Holt, W.E. (2012). Plate motions and stresses from global dynamic models. *Science*, *335*(6070), 838–843.

Ghosh, A., Holt, W.E., & Flesch, L.M. (2009). Contribution of gravitational potential energy differences to the global stress field. *Geophysical Journal International*, *179*(2), 787–812.

Ghosh, A., Holt, W.E., & Wen, L. (2013b). Predicting the lithospheric stress field and plate motions by joint modeling of lithosphere and mantle dynamics. *Journal of Geophysical Research: Solid Earth*, *118*(1), 346–368.

Hager, B.H. & O'Connell, R.J. (1981). A simple global model of plate dynamics and mantle convection. *Journal of Geophysical Research*, *86*(B6), 4843–4867.

Hatzfeld, D., Authemayou, C., van der Beek, P., Bellier, O., Lavé, J., Oveisi, B., Tatar, M., Tavakoli, F., Walpersdorf, A., & Yamini-Fard, F. (2010). The kinematics of the Zagros mountains (Iran). *Geological Society, London, Special Publications*, *330*(1), 19–42.

Hatzfeld, D. & Molnar, P. (2010). Comparisons of the kinematics and deep structures of the Zagros and Himalaya and of the Iranian and Tibetan plateaus and geodynamic implications. *Reviews of Geophysics*, *48*(2).

Heidbach, O., Rajabi, M., Reiter, K., & Ziegler, M. (2016). WSM Team (2016): World Stress Map Database Release 2016. *GFZ Data Services*, doi:http://doi.org/10.5880/WSM.2016.001.

Heidbach, O., Reinecker, J., Tingay, M., Müller, B., Sperner, B., Fuchs, K., & Wenzel, F. (2007). Plate boundary forces are not enough: Second-and third-order stress patterns highlighted in the World Stress Map database. *Tectonics*, *26*(6), doi:10.1029/2007TC002133.

Hessami, K., Nilforoushan, F., & Talbot, C.J. (2006). Active deformation within the Zagros Mountains deduced from GPS measurements. *Journal of the Geological Society*, *163*(1), 143–148.

Hollingsworth, J., Fattahi, M., Walker, R., Talebian, M., Bahroudi, A., Bolourchi, M.J., Jackson, J., & Copley, A. (2010). Oroclinal bending, distributed thrust and strike-slip faulting, and the accommodation of Arabia–Eurasia convergence in NE Iran since the Oligocene. *Geophysical Journal International*, *181*(3), 1214–1246.

Irandoust, M.A., Priestley, K., & Sobouti, F. (2022). High-resolution Lithospheric Structure of the Zagros Collision Zone and Iranian Plateau. *Journal of Geophysical Research: Solid Earth*, *127*(11), e2022JB025009, doi:https://doi.org/10.1029/2022JB025009.

Jackson, J. & McKenzie, D. (1984). Active tectonics of the Alpine—Himalayan Belt between western Turkey and Pakistan. *Geophysical Journal International*, *77*(1), 185–264.

585 Jackson, J., Priestley, K., Allen, M., & Berberian, M. (2002). Active tectonics of the south Caspian
586 basin. *Geophysical Journal International*, *148*(2), 214–245.

587 Jolivet, L. & Faccenna, C. (2000). Mediterranean extension and the Africa-Eurasia collision. *Tectonics*,
588 *19*(6), 1095–1106.

589 Kaviani, A., Hatzfeld, D., Paul, A., Tatar, M., & Priestley, K. (2009). Shear-wave splitting, lithospheric
590 anisotropy, and mantle deformation beneath the Arabia–Eurasia collision zone in Iran. *Earth and*
591 *Planetary Science Letters*, *286*(3-4), 371–378.

592 Kaviani, A., Mahmoodabadi, M., Rümpker, G., Pilia, S., Tatar, M., Nilfouroushan, F., Yamini-Fard,
593 F., Moradi, A., & Ali, M.Y. (2021). Mantle-flow diversion beneath the Iranian plateau induced by
594 Zagros' lithospheric keel. *Scientific reports*, *11*(1), 1–12.

595 Khodaverdian, A., Zafarani, H., & Rahimian, M. (2015). Long term fault slip rates, distributed defor-
596 mation rates and forecast of seismicity in the Iranian Plateau. *Tectonics*, *34*(10), 2190–2220.

597 Khorrami, F., Vernant, P., Masson, F., Nilfouroushan, F., Mousavi, Z., Nankali, H., Saadat, S.A.,
598 Walpersdorf, A., Hosseini, S., Tavakoli, P., et al. (2019). An up-to-date crustal deformation map
599 of Iran using integrated campaign-mode and permanent GPS velocities. *Geophysical Journal Inter-*
600 *national*, *217*(2), 832–843.

601 Koptev, A. & Ershov, A. (2010). The role of the gravitational potential of the lithosphere in the formation
602 of a global stress field. *Izvestiya, Physics of the Solid Earth*, *46*(12), 1080–1094.

603 Kreemer, C., Blewitt, G., & Klein, E.C. (2014). A geodetic plate motion and Global Strain Rate Model.
604 *Geochemistry, Geophysics, Geosystems*, *15*(10), 3849–3889.

605 Kustowski, B., Ekström, G., & Dziewoński, A. (2008a). Anisotropic shear-wave velocity structure of
606 the Earth's mantle: A global model. *Journal of Geophysical Research: Solid Earth*, *113*(B6).

607 Kustowski, B., Ekström, G., & Dziewoński, A. (2008b). The shear-wave velocity structure in the upper
608 mantle beneath Eurasia. *Geophysical Journal International*, *174*(3), 978–992.

609 Le Dortz, K., Meyer, B., Sébrier, M., Nazari, H., Braucher, R., Fattahi, M., Benedetti, L., Foroutan, M.,
610 Siame, L., Bourlès, D., et al. (2009). Holocene right-slip rate determined by cosmogenic and OSL
611 dating on the Anar fault, Central Iran. *Geophysical Journal International*, *179*(2), 700–710.

612 Lithgow-Bertelloni, C. & Guynn, J.H. (2004). Origin of the lithospheric stress field. *Journal of Geo-*
613 *physical Research: Solid Earth*, *109*(B1), doi:10.1029/2003JB002467.

Masson, F., Anvari, M., Djamour, Y., Walpersdorf, A., Tavakoli, F., Daignieres, M., Nankali, H., & Van Gorp, S. (2007). Large-scale velocity field and strain tensor in Iran inferred from GPS measurements: new insight for the present-day deformation pattern within NE Iran. *Geophysical Journal International*, *170*(1), 436–440.

Masson, F., Djamour, Y., Van Gorp, S., Chéry, J., Tatar, M., Tavakoli, F., Nankali, H., & Vernant, P. (2006). Extension in NW Iran driven by the motion of the South Caspian Basin. *Earth and Planetary Science Letters*, *252*(1-2), 180–188.

Mazhari, S., Bea, F., Amini, S., Ghalamghash, J., Molina, J., Montero, P., Scarrow, J., & Williams, I. (2009). The Eocene bimodal Piranshahr massif of the Sanandaj–Sirjan Zone, NW Iran: a marker of the end of the collision in the Zagros orogen. *Journal of the Geological Society*, *166*(1), 53–69.

McClusky, S., Balassanian, S., Barka, A., Demir, C., Ergintav, S., Georgiev, I., Gurkan, O., Hamburger, M., Hurst, K., Kahle, H., et al. (2000). Global Positioning System constraints on plate kinematics and dynamics in the eastern Mediterranean and Caucasus. *Journal of Geophysical Research: Solid Earth*, *105*(B3), 5695–5719.

Md, S.I. & Ryuichi, S. (2010). Neotectonic stress field and deformation pattern within the Zagros and its adjoining area: An approach from finite element modeling. *Journal of Geology and Mining Research*, *2*(7), 170–182.

Mégnin, C. & Romanowicz, B. (2000). The three-dimensional shear velocity structure of the mantle from the inversion of body, surface and higher-mode waveforms. *Geophysical Journal International*, *143*(3), 709–728.

Raeesi, M., Zarifi, Z., Nilfouroushan, F., Boroujeni, S.A., & Tiampo, K. (2017). Quantitative analysis of seismicity in Iran. *Pure and Applied Geophysics*, *174*(3), 793–833.

Reilinger, R. & McClusky, S. (2011). Nubia–Arabia–Eurasia plate motions and the dynamics of Mediterranean and Middle East tectonics. *Geophysical Journal International*, *186*(3), 971–979.

Reilinger, R., McClusky, S., Paradissis, D., Ergintav, S., & Vernant, P. (2010). Geodetic constraints on the tectonic evolution of the Aegean region and strain accumulation along the Hellenic subduction zone. *Tectonophysics*, *488*(1-4), 22–30.

Reilinger, R., McClusky, S., Vernant, P., Lawrence, S., Ergintav, S., Cakmak, R., Ozener, H., Kadirov, F., Guliev, I., Stepanyan, R., Nadariya, M., Hahubia, G., Mahmoud, S., Sakr, K., ArRajehi, A., Paradissis,

643 D., Al-Aydrus, A., Prilepin, M., Guseva, T., Evren, E., Dmitrotsa, A., Filikov, S.V., Gomez, F., Al-
644 Ghazzi, R., & Karamm, G. (2006). GPS constraints on continental deformation in the Africa-Arabia-
645 Eurasia continental collision zone and implications for the dynamics of plate interactions. *Journal of*
646 *Geophysical Research: Solid Earth*, *111*(B5), doi:10.1029/2005JB004051.

647 Richardson, R.M., Solomon, S.C., & Sleep, N.H. (1976). Intraplate stress as an indicator of plate tectonic
648 driving forces. *Journal of geophysical research*, *81*(11), 1847–1856.

649 Ritsema, J., Deuss, A.A., Van Heijst, H.J., & Woodhouse, J.H. (2011). S40RTS: a degree-40 shear-
650 velocity model for the mantle from new Rayleigh wave dispersion, teleseismic traveltime and normal-
651 mode splitting function measurements. *Geophysical Journal International*, *184*(3), 1223–1236.

652 Sadeghi-Bagherabadi, A., Sobouti, F., Ghods, A., Motaghi, K., Talebian, M., Chen, L., Jiang, M., Ai, Y.,
653 & He, Y. (2018). Upper mantle anisotropy and deformation beneath the major thrust-and-fold belts of
654 Zagros and Alborz and the Iranian Plateau. *Geophysical Journal International*, *214*(3), 1913–1918.

655 Sattarzadeh, Y., Cosgrove, J.W., & Vita-Finzi, C. (2002). The geometry of structures in the Zagros cover
656 rocks and its neotectonic implications. *Geological Society, London, Special Publications*, *195*(1),
657 205–217.

658 Singh, S. & Ghosh, A. (2019). Surface motions and continental deformation in the Indian plate and
659 the India-Eurasia collision zone. *Journal of Geophysical Research: Solid Earth*, *124*, doi:10.1029/
660 2018JB017289.

661 Singh, S. & Ghosh, A. (2020). The role of crustal models in the dynamics of the India–Eurasia collision
662 zone. *Geophysical Journal International*, *223*(1), 111–131.

663 Sobouti, F. & Arkani-Hamed, J. (1996). Numerical modelling of the deformation of the Iranian plateau.
664 *Geophysical Journal International*, *126*(3), 805–818.

665 Talebian, M. & Jackson, J. (2002). Offset on the Main Recent Fault of NW Iran and implications for
666 the late Cenozoic tectonics of the Arabia–Eurasia collision zone. *Geophysical Journal International*,
667 *150*(2), 422–439.

668 Tatar, M. & Hatzfeld, D. (2009). Microseismic evidence of slip partitioning for the Rudbar-Tarom earth-
669 quake (Ms 7.7) of 1990 June 20 in NW Iran. *Geophysical Journal International*, *176*(2), 529–541.

670 Vernant, P. & Chéry, J. (2006). Mechanical modelling of oblique convergence in the Zagros, Iran. *Geo-*
671 *physical Journal International*, *165*(3), 991–1002.

Vernant, P., Nilforoushan, F., Hatzfeld, D., Abbassi, M., Vigny, C., Masson, F., Nankali, H., Martinod, J., Ashtiani, A., Bayer, R., et al. (2004). Present-day crustal deformation and plate kinematics in the Middle East constrained by GPS measurements in Iran and northern Oman. *Geophysical Journal International*, *157*(1), 381–398.

Vincent, S.J., Allen, M.B., Ismail-Zadeh, A.D., Flecker, R., Foland, K.A., & Simmons, M.D. (2005). Insights from the Talysh of Azerbaijan into the Paleogene evolution of the South Caspian region. *Geological Society of America Bulletin*, *117*(11-12), 1513–1533.

Walker, R.T. (2006). A remote sensing study of active folding and faulting in southern Kerman province, SE Iran. *Journal of Structural Geology*, *28*(4), 654–668.

Walpersdorf, A., Hatzfeld, D., Nankali, H., Tavakoli, F., Nilforoushan, F., Tatar, M., Vernant, P., Chéry, J., & Masson, F. (2006). Difference in the GPS deformation pattern of North and Central Zagros (Iran). *Geophysical Journal International*, *167*(3), 1077–1088.

Walpersdorf, A., Manighetti, I., Mousavi, Z., Tavakoli, F., Vergnolle, M., Jadidi, A., Hatzfeld, D., Aghamohammadi, A., Bigot, A., Djamour, Y., et al. (2014). Present-day kinematics and fault slip rates in eastern Iran, derived from 11 years of GPS data. *Journal of Geophysical Research: Solid Earth*, *119*(2), 1359–1383.

Yadav, R. & Tiwari, V. (2018). Numerical simulation of present day tectonic stress across the Indian subcontinent. *International Journal of Earth Sciences*, *107*(7), 2449–2462.

Yamato, P., Kaus, B.J., Mouthereau, F., & Castelltort, S. (2011). Dynamic constraints on the crustal-scale rheology of the Zagros fold belt, Iran. *Geology*, *39*(9), 815–818.

Yang, Y., Liang, C., Fang, L., Su, J., & Hua, Q. (2018). A comprehensive analysis on the stress field and seismic anisotropy in eastern Tibet. *Tectonics*, *37*(6), 1648–1657.

Zoback, M.L. (1992). First-and second-order patterns of stress in the lithosphere: The World Stress Map Project. *Journal of Geophysical Research: Solid Earth*, *97*(B8), 11703–11728.

**Figure 1:** Tectonic overview of Central Eurasia. Abbreviations: CF: Chaman Fault; MSZ: Makran Subduction Zone; MZT: Main Zagros Thrust; HZF: High Zagros Fault; MFF: Mountain Front Fault; SSZ: Sanandaj Sirjan Zone; UDMA: Urumieh-Dokhtar Arc; MRF: Main Recent Fault.

**Figure 2:** Thickness and density variations of different crustal layers in all three crustal and lithospheric models.

**Figure 3:** (a) Most compressive horizontal principal axes ($SH_{max}$) from WSM (Heidbach et al., 2016). Red indicates normal fault regime, blue indicates thrust regime, whereas green denotes strike-slip regime, (b) Observed plate velocities in a no-net-rotation frame of reference from Kreemer et al. (2014) plotted on top of second invariant of strain rate tensors obtained from Kreemer et al. (2014) plotted on $1^\circ \times 1^\circ$ grid.

**Figure 4:** (Left Panel) Deviatoric stresses predicted from GPE variations, plotted on top of their second invariants. The compressional stresses are denoted by solid black arrows, while white arrows show tensional stresses. $SH_{max}$ axes predicted from GPE variations are plotted in right panel. Red denotes tensional regime, blue is for thrust and green for strike-slip regime.

**Figure 5:** (Left Panel) Total misfit between observed and predicted $SH_{max}$ from GPE variations. Correlation coefficients between strain rate tensors obtained from Kreemer et al. (2014) and deviatoric stresses predicted using GPE variations are shown in middle panel, with average regional correlation coefficients given on bottom right of each figure. (Right panel) Observed velocities (black) and predicted plate velocities(white) from GPE variations in NNR frame, plotted on the top of angular misfit between both.

**Figure 6:** (Left Panel) Deviatoric stresses predicted using mantle tractions derived from various tomography models for GHW13 viscosity structure, plotted on second invariant of deviatoric stresses. The white arrows denote tensional stresses, and black arrows indicate compressional stresses. $SH_{max}$ predicted from mantle tractions are shown in right panel. Red denotes tensional regime, blue is for thrust and green is for strike-slip regime.

**Figure 7:** Parameters predicted from mantle tractions and their comparisons with observables. (Left panel) Total misfit between $SH_{max}$ obtained from WSM (Heidbach et al., 2016) and those predicted using mantle tractions derived from various tomography models using GHW13 viscosity structure. Correlation coefficients between strain rate tensors obtained from Kreemer et al. (2014) and deviatoric stresses predicted using basal tractions are shown in middle panel, with average regional correlation coefficients given on bottom right of each figure. (Right pannel) Observed velocities (black) and plate velocities predicted using mantle tractions (white) in NNR frame plotted on the top of angular deviation between both.

**Figure 8:** (Left panel) Deviatoric stresses predicted using combined effects of GPE computed from CRUST2 and mantle tractions derived from various tomography models plotted on top of their second invariants. The white arrows denote tensional stresses, and black arrows indicate compressional stresses. The right panel shows $SH_{max}$ predicted from these models. The red lines denote tensional regime, blue is for thrust and green is for strike-slip regime.

**Figure 9:** (Left panel) Deviatoric stresses (a-d) predicted using combined effects of GPE computed from CRUST1 and mantle tractions derived from various tomography models plotted on top of their second invariants. The white arrows denote tensional stresses, and black arrows indicate compressional stresses. The right panel shows $SH_{max}$ predicted from these models. The red lines denote tensional regime, blue is for thrust and green is for strike-slip regime.

**Figure 10:** (Left panel) Deviatoric stresses (a-d) predicted using combined effects of GPE computed from LITHO and mantle tractions derived from various tomography models plotted on top of their second invariants. The white arrows denote tensional stresses, and black arrows indicate compressional stresses. The right panel shows $SH_{max}$ predicted from these models. The red lines denote tensional regime, blue is for thrust and green is for strike-slip regime.

**Figure 11:** Total misfit between observed $SH_{max}$ from WSM (Heidbach et al., 2016) and $SH_{max}$ predicted using combined effects of GPE computed from different crustal models and mantle tractions derived from various tomography models.

**Figure 12:** Correlation coefficients between strain rate tensors from Kreemer et al. (2014) and deviatoric stress tensors predicted using combined effects of GPE computed from different crustal models and mantle tractions derived from various tomography models. Average correlation coefficient is given in right lower corner of the figure.

**Figure 13:** Plate velocities predicted using combined effects of GPE computed from different crustal models and mantle tractions derived from various tomography models plotted on top of angular misfit ($\theta$). Black arrows represent observed NNR velocities (Kreemer et al., 2014) and white ones denote predicted velocities.

**Figure 14:** Predicted parameters of best fit model, S40RTScr2. (a) GPS (blue) and predicted (red) plate velocities with respect to a fixed Eurasian plate, (b) FPDs and $SH_{max}$ are plotted for the best fit model, (c) Correlation between deviatoric stresses predicted from GPE and mantle convection models, and (d) ratio ($T_1/T_2$) of second invariant of deviatoric stresses from GPE ($T_1$) to those from mantle tractions ($T_2$).

Figure 1:

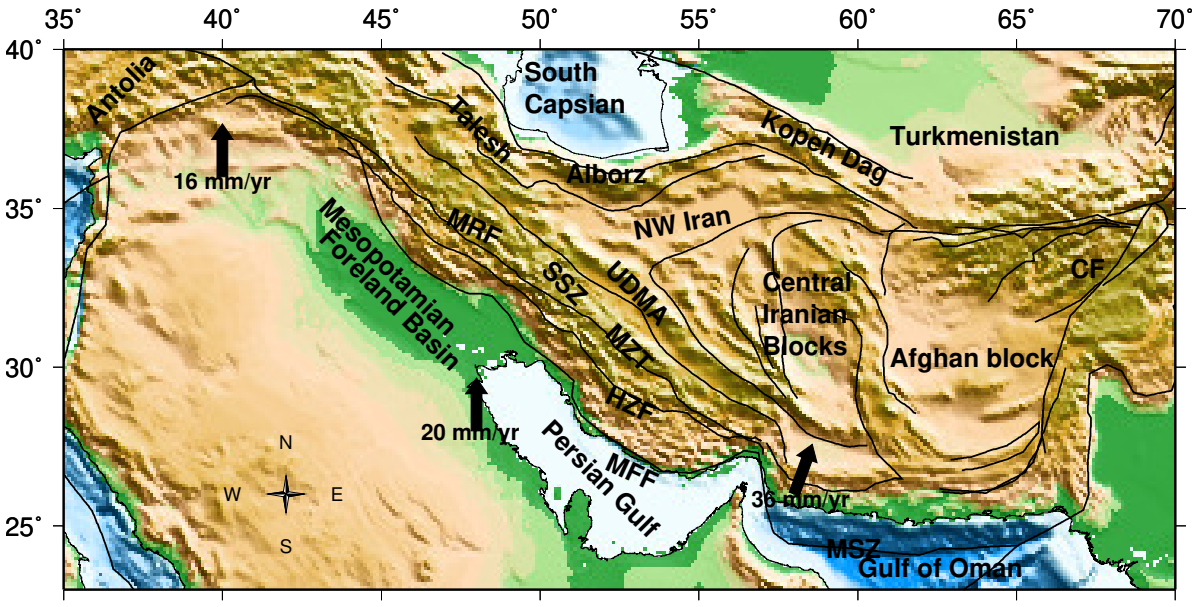
35˚
40˚
45˚
50˚
55˚
60˚
65˚
70˚
40˚
35˚
30˚
25˚
Anatolia
16 mm/yr
Talesh
South
Capsian
Alborz
Kopeh Dag
Turkmenistan
MRF
NW Iran
Mesopotamian
Foreland Basin
SSZ
UDMA
MZT
HZF
CF
Central
Iranian
Blocks
Afghan block
20 mm/yr
Persian Gulf
MFF
36 mm/yr
MSZ
Gulf of Oman
N
W
E
S

Figure 2:

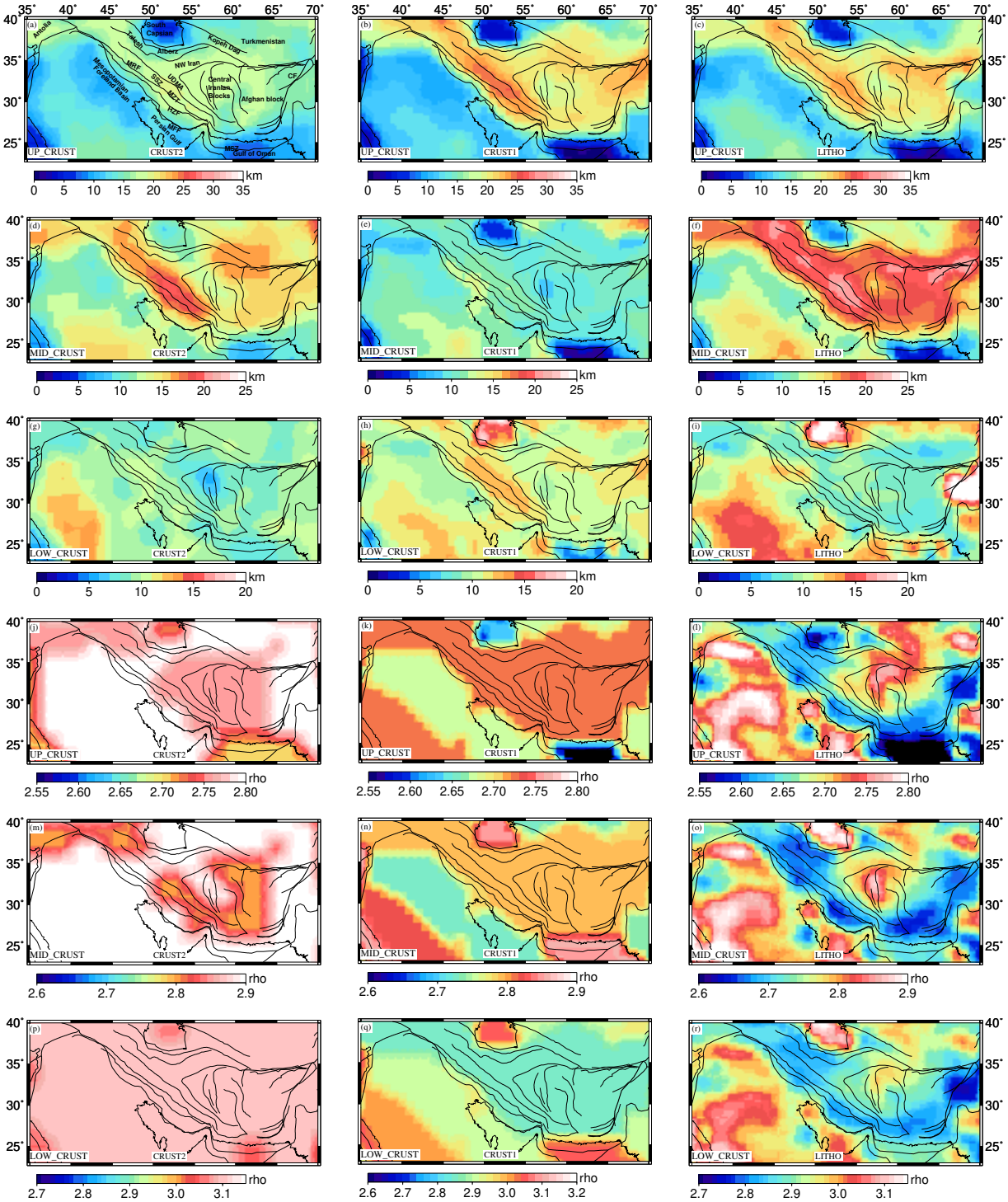
(a)
(b)
(c)
(d)
(e)
(f)
(g)
(h)
(i)
(j)
(k)
(l)
(m)
(n)
(o)
(p)
(q)
(r)
South Caspian
Turkmenistan
Alborz
NW Iran
Central Iranian Blocks
Afghan block
CF
MBF
SSZ
MZT
YDF
Persian Gulf
MSZ
Gulf of Oman
UP_CRUST
MID_CRUST
LOW_CRUST
CRUST1
CRUST2
LITHO
km
rho

Figure 3:

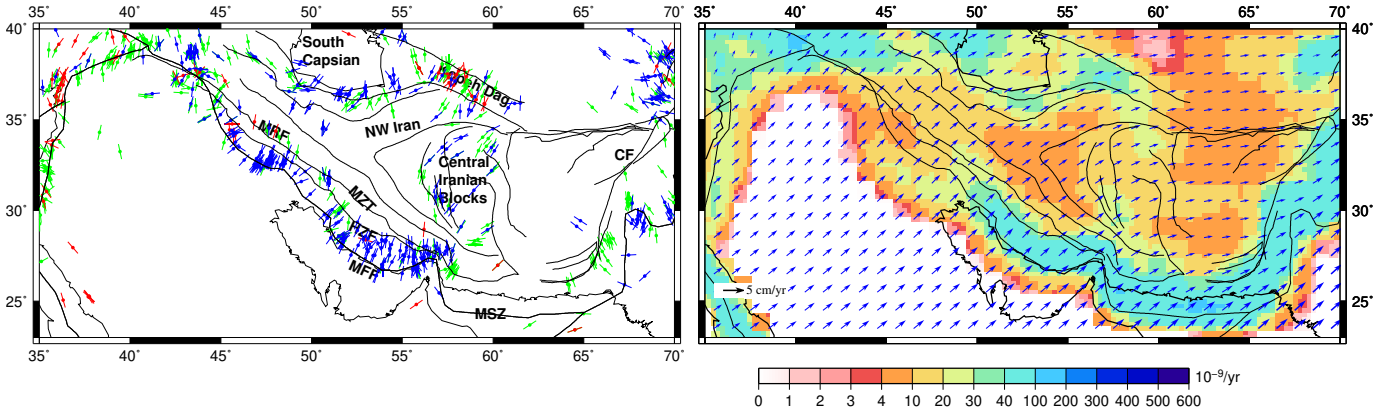
35˚
40˚
45˚
50˚
55˚
60˚
65˚
70˚
25˚
30˚
35˚
40˚
South Capsian
Kopeh Dag
NW Iran
MRF
Central Iranian Blocks
CF
MZT
HZT
MFR
MSZ
5 cm/yr
0 1 2 3 4 10 20 30 40 100 200 300 400 500 600
10⁻⁹/yr

Figure 4:

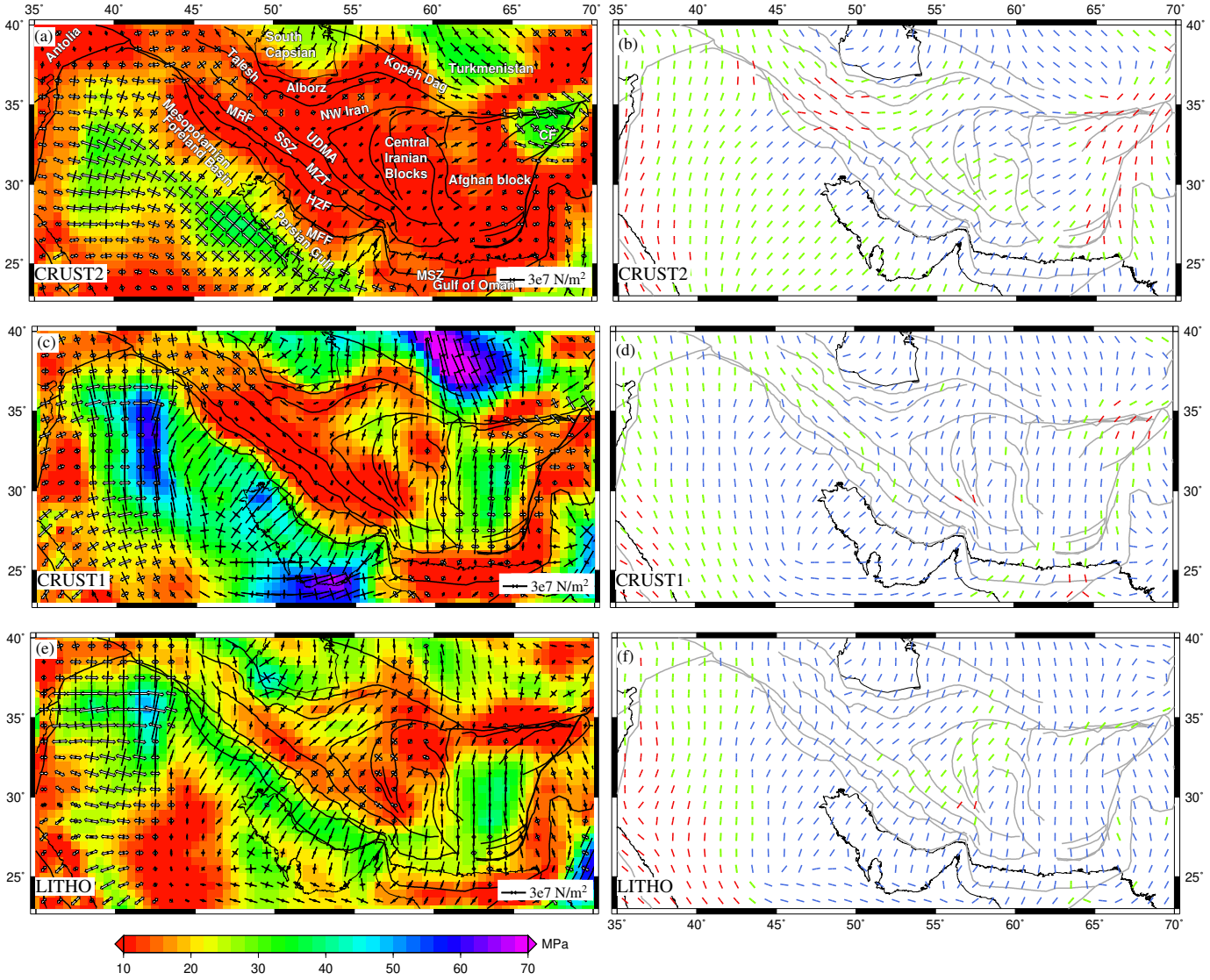
(a)
(b)
(c)
(d)
(e)
(f)
Anatolia
South Caspian
Turkmenistan
Kopeh Dag
Alborz
Talesh
NW Iran
MRF
SSZ
UDMA
MZT
HZF
MFF
CF
Central Iranian Blocks
Afghan block
Mesopotamian Foreland Basin
Persian Gulf
MSZ
Gulf of Oman
CRUST2
CRUST1
LITHO
3e7 N/m²
MPa
10
20
30
40
50
60
70
35°
40°
45°
50°
55°
60°
65°
70°
25°
30°
35°
40°

Figure 5:

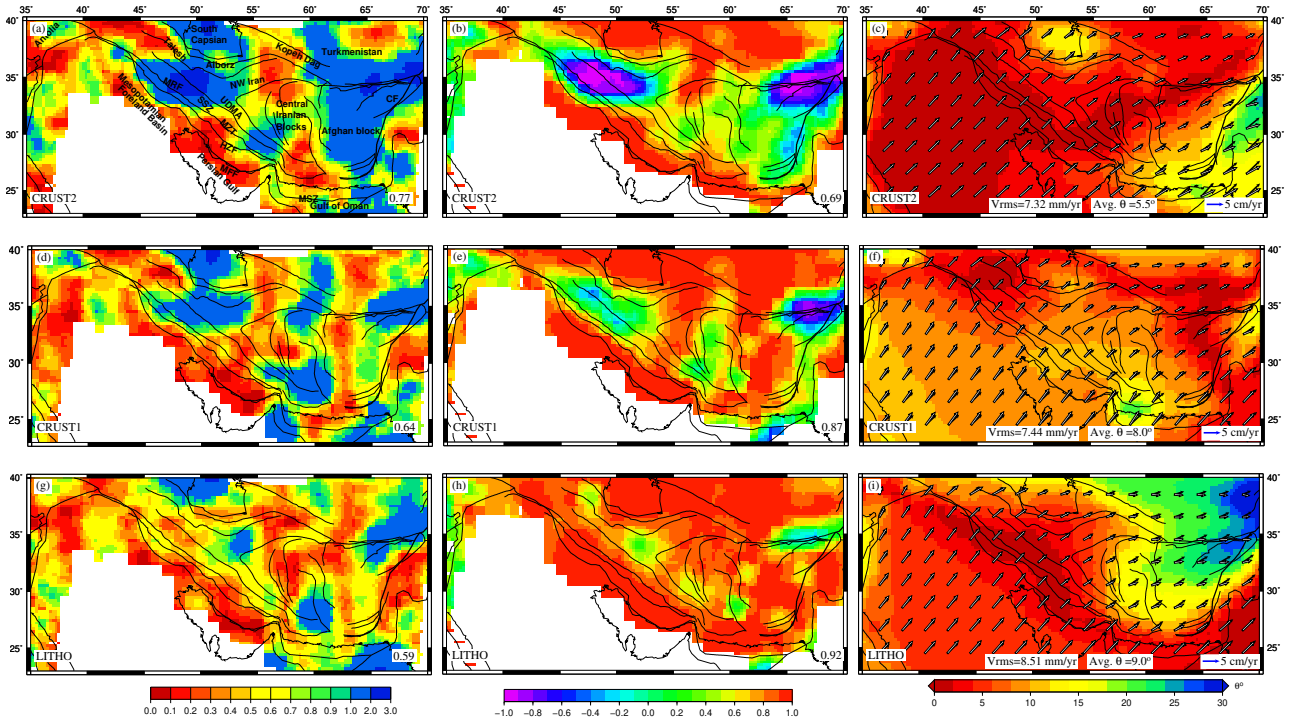
(a)
(b)
(c)
(d)
(e)
(f)
(g)
(h)
(i)
CRUST2
CRUST1
LITHO
0.77
0.69
0.64
0.87
0.59
0.92
Vrms=7.32 mm/yr
Avg. θ =5.5°
Vrms=7.44 mm/yr
Avg. θ =8.0°
Vrms=8.51 mm/yr
Avg. θ =9.0°
5 cm/yr
South Caspian
Turkmenistan
Alborz
NW Iran
Central Iranian Blocks
Afghan block
CF
MRF
SSZ
UDMA
MFZ
RRF
MSZ
Gulf of Oman
Makran Basin
Makran Wedge
Kopeh Dagh
Amu Dar
Tarim
0.0 0.1 0.2 0.3 0.4 0.5 0.6 0.7 0.8 0.9 1.0 2.0 3.0
−1.0 −0.8 −0.6 −0.4 −0.2 0.0 0.2 0.4 0.6 0.8 1.0
0 5 10 15 20 25 30 θ°

Figure 6:

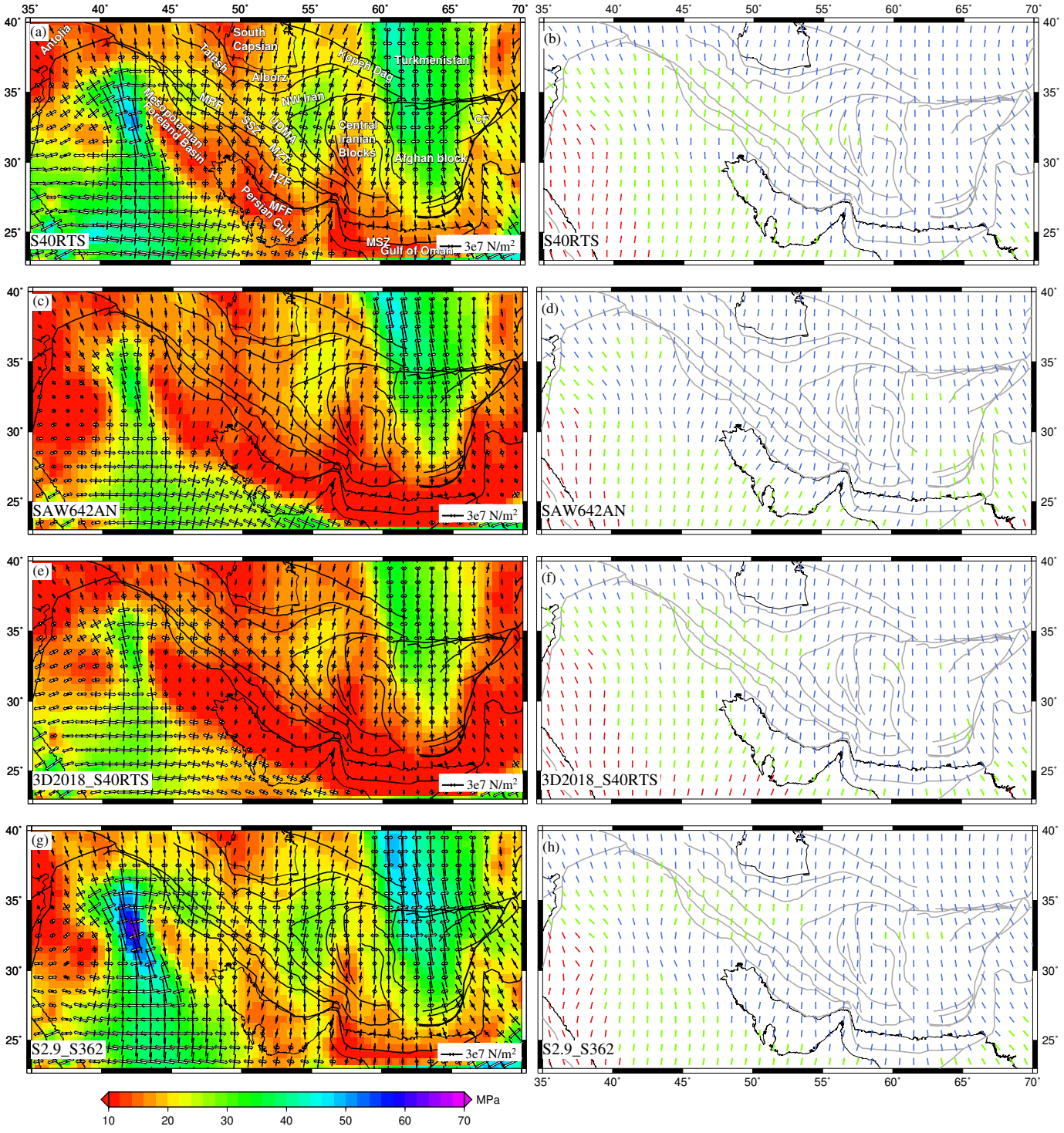
(a)
S40RTS
(b)
S40RTS
(c)
SAW642AN
(d)
SAW642AN
(e)
3D2018_S40RTS
(f)
3D2018_S40RTS
(g)
S2.9_S362
(h)
S2.9_S362
3e7 N/m²
Anatolia
South Caspian
Turkmenistan
Kopeh Dagh
Alborz
Zagros
Mesopotamian and Basin
NW Iran
Central Iranian Blocks
Afghan block
CF
MFF
HZF
MZF
SSF
ZDMA
Persian Gulf
MSZ
Gulf of Oman
MPa
10
20
30
40
50
60
70

Figure 7:

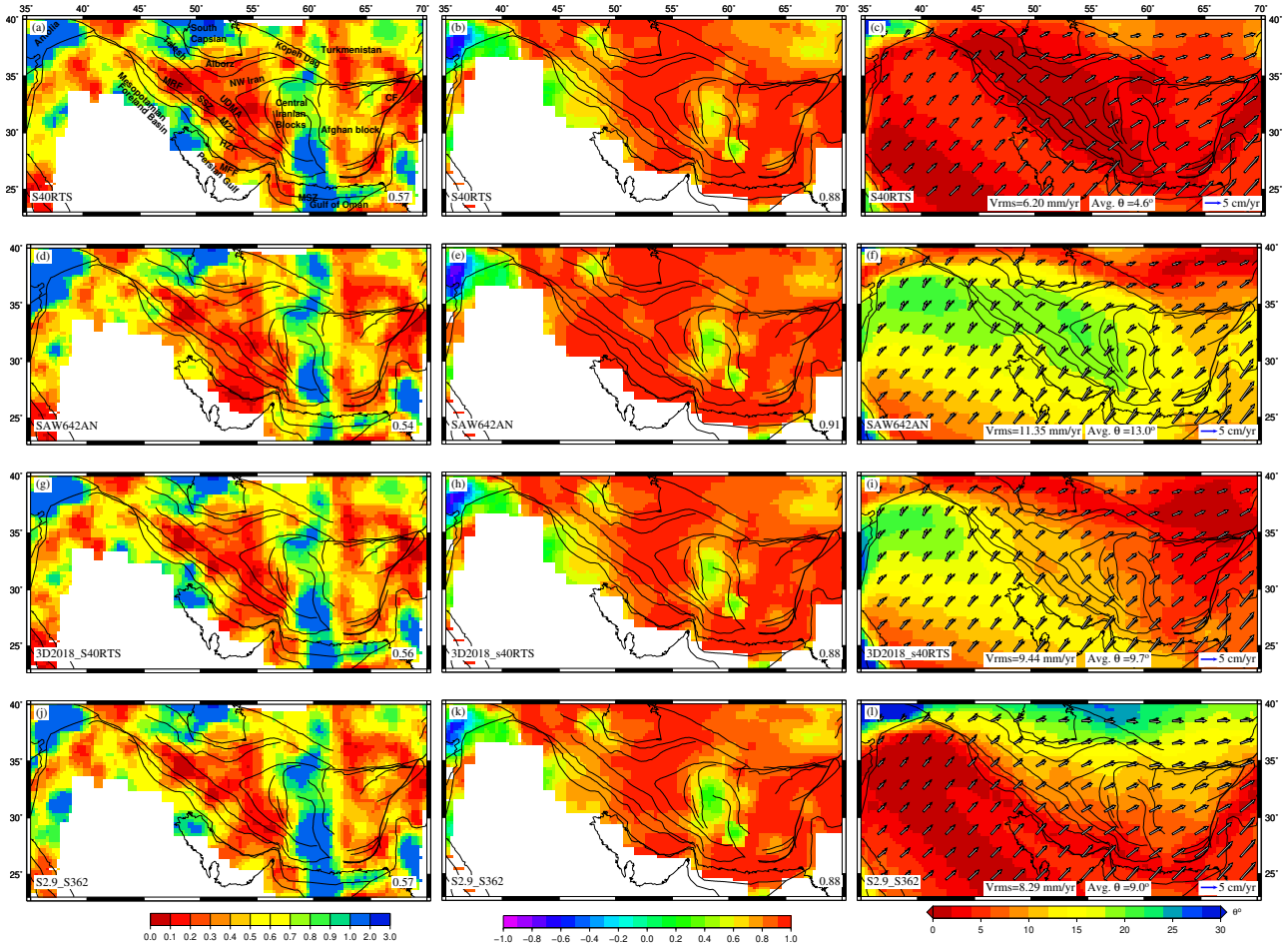
(a)
(b)
(c)
(d)
(e)
(f)
(g)
(h)
(i)
(j)
(k)
(l)
South Caspian
Turkmenistan
Kopeh Dagh
Alborz
NW Iran
Central Iranian Blocks
Afghan block
CF
MRF
SSZ
UDMA
HFF
MFF
Persian Gulf
MSZ
Gulf of Oman
Arabia
Zagros
Mesopotamian Foreland Basin
S40RTS
SAW642AN
3D2018_S40RTS
3D2018_s40RTS
S2.9_S362
0.57
0.88
0.54
0.91
0.56
Vrms=6.20 mm/yr
Avg. θ =4.6°
Vrms=11.35 mm/yr
Avg. θ =13.0°
Vrms=9.44 mm/yr
Avg. θ =9.7°
Vrms=8.29 mm/yr
Avg. θ =9.0°
5 cm/yr
0.0 0.1 0.2 0.3 0.4 0.5 0.6 0.7 0.8 0.9 1.0 2.0 3.0
−1.0 −0.8 −0.6 −0.4 −0.2 0.0 0.2 0.4 0.6 0.8 1.0
θ°
0 5 10 15 20 25 30

Figure 8:

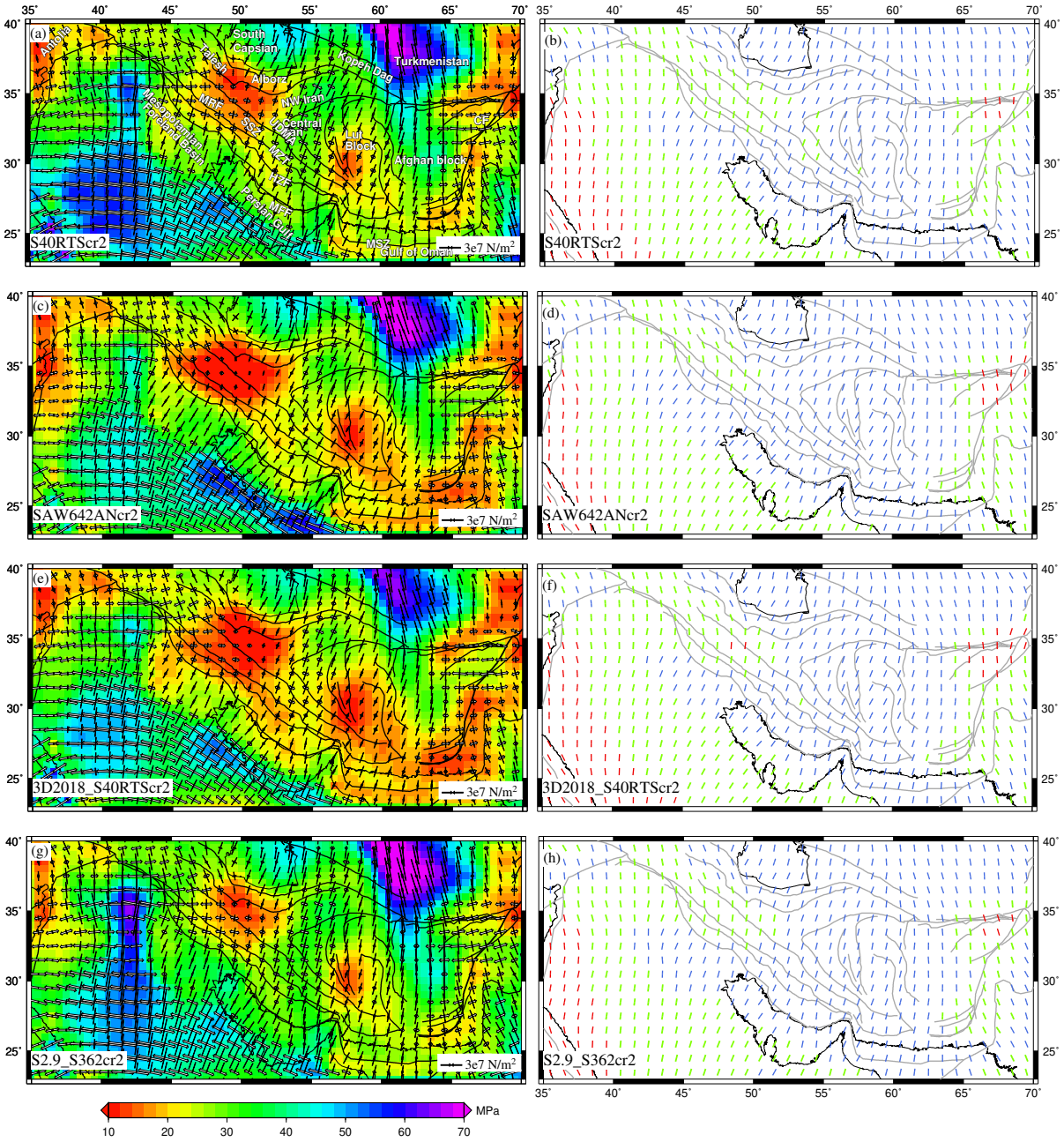
(a)
(b)
(c)
(d)
(e)
(f)
(g)
(h)
South Caspian
Turkmenistan
Alborz
Kopeh Dag
Kura
Central Iran
Lut Block
Afghan block
Zagros
MFF
MZT
MZRF
MZ2
MZ1
Persian Gulf
MSZ
Gulf of Oman
S40RTScr2
SAW642ANcr2
3D2018_S40RTScr2
S2.9_S362cr2
3e7 N/m2
MPa
10
20
30
40
50
60
70

Figure 9:

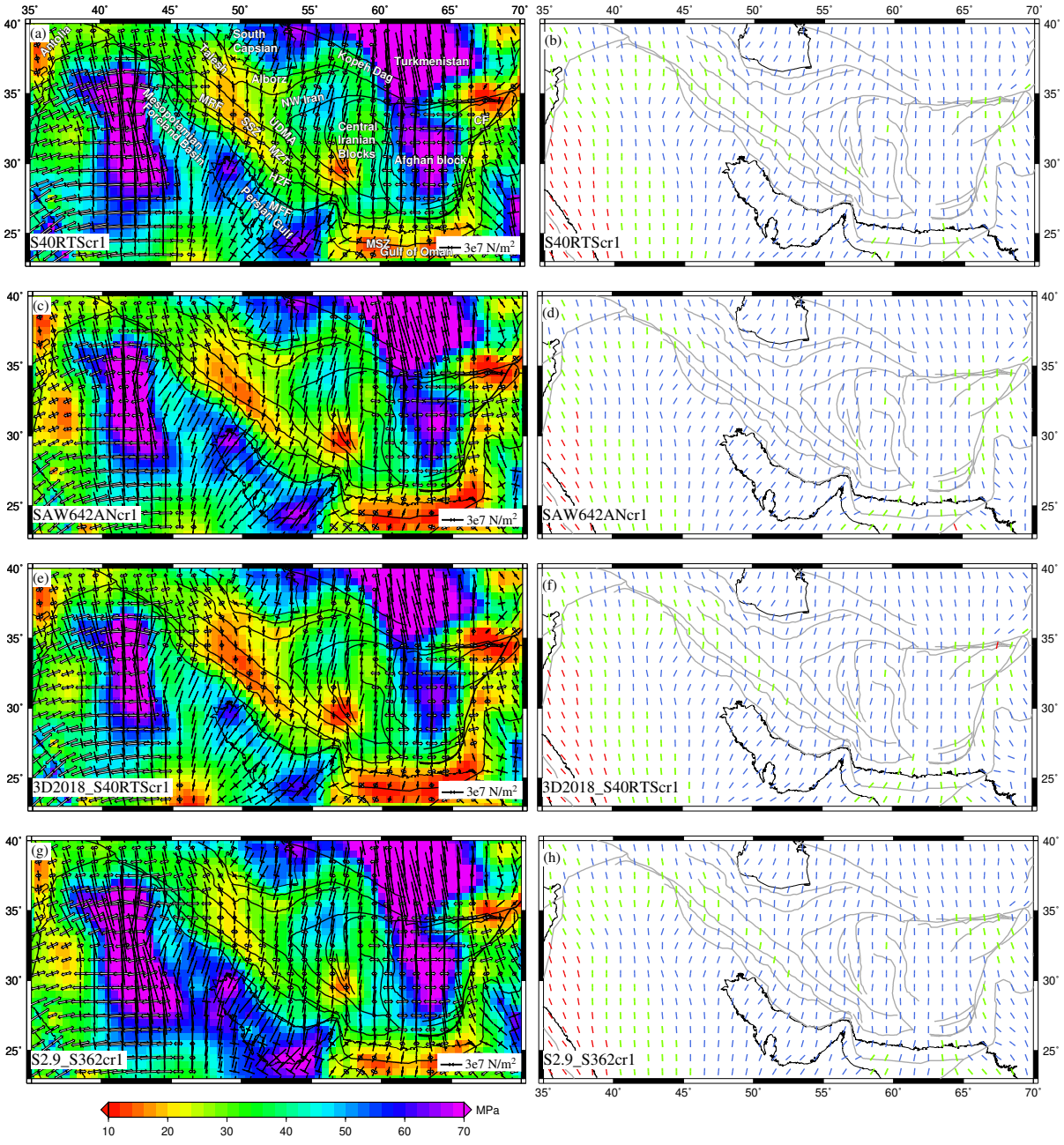
(a)
(b)
(c)
(d)
(e)
(f)
(g)
(h)
South Caspian
Turkmenistan
Kopeh Dag
Alborz
NWIran
Zagros
Mesopotamian Foredeep Basin
SSZ
UDMA
HZF
MFF
Persian Gulf
Central Iranian Blocks
Afghan block
MSZ
Gulf of Oman
S40RTScr1
SAW642ANcr1
3D2018_S40RTScr1
S2.9_S362cr1
3e7 N/m²
MPa
10
20
30
40
50
60
70

Figure 10:

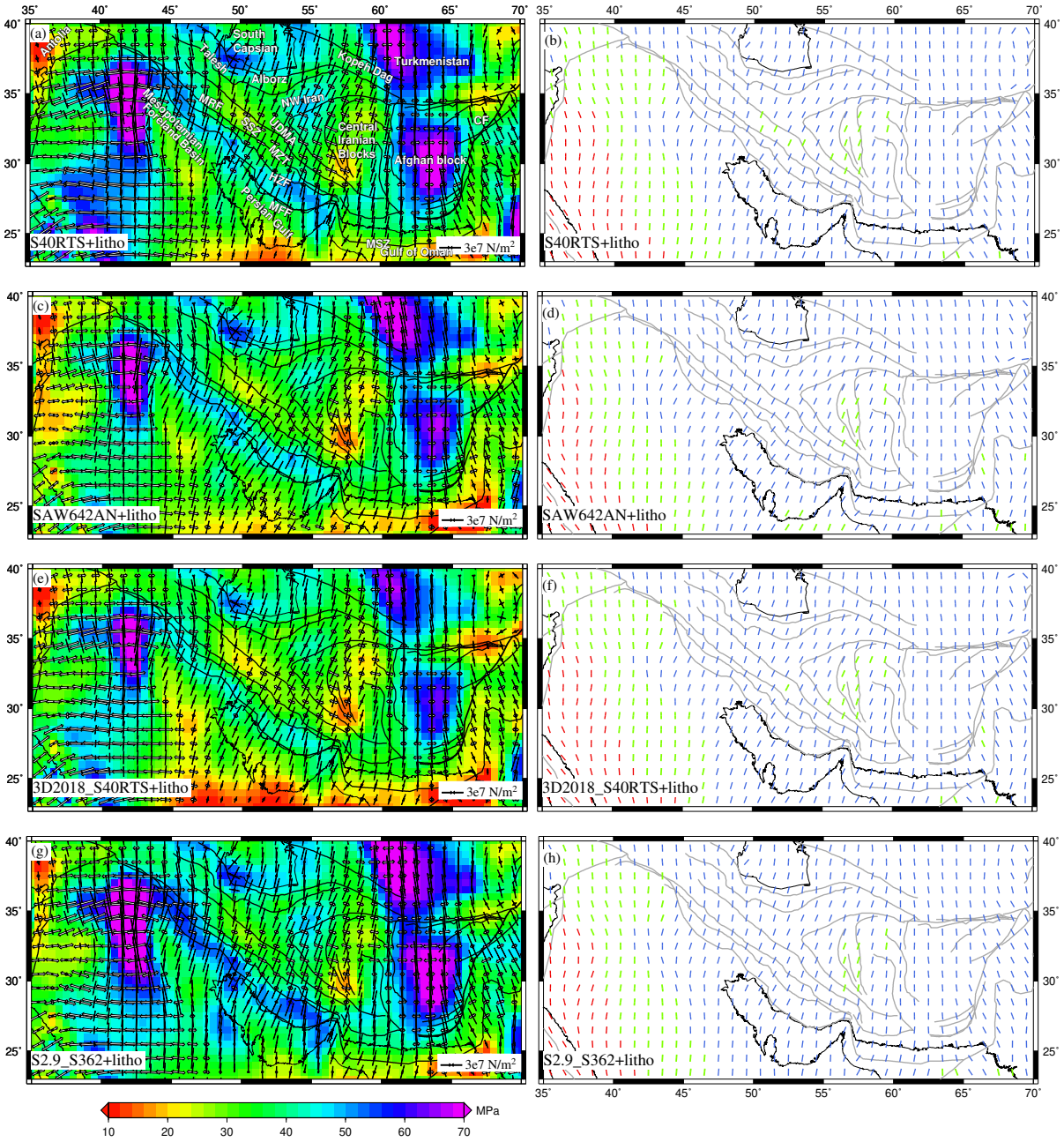
(a)
(b)
(c)
(d)
(e)
(f)
(g)
(h)
South Caspian
Turkmenistan
Alborz
Kopeh Dag
NW Iran
Central Iranian Blocks
Afghan block
CE
Makran
Zagros
MFF
HZF
MZT
SSZ
DDMA
Persian Gulf
MSZ
Gulf of Oman
S40RTS+litho
SAW642AN+litho
3D2018_S40RTS+litho
S2.9_S362+litho
3e7 N/m$^2$
MPa
10
20
30
40
50
60
70
35˚
40˚
45˚
50˚
55˚
60˚
65˚
70˚
25˚
30˚

Figure 11:

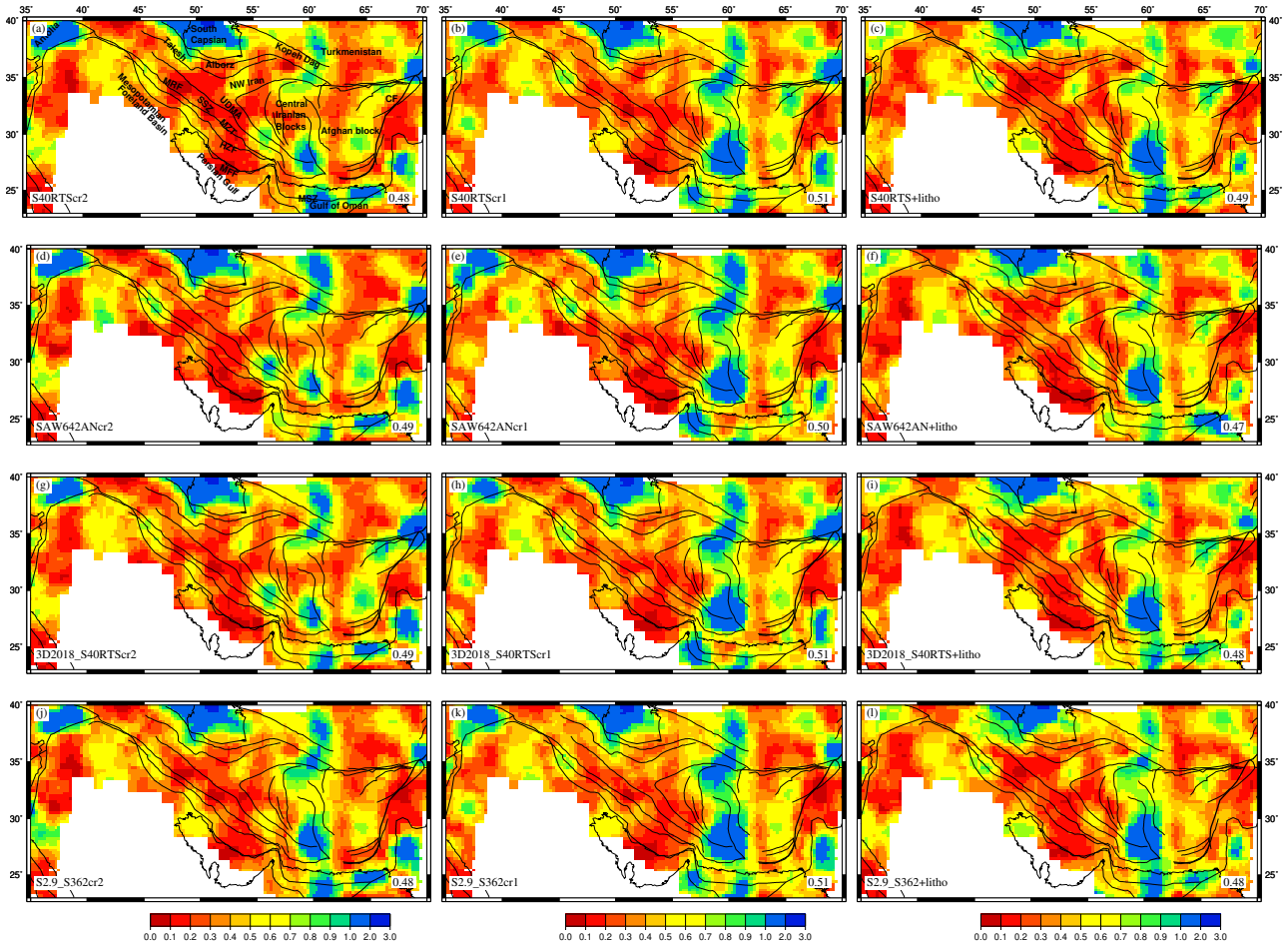
(a)
(b)
(c)
(d)
(e)
(f)
(g)
(h)
(i)
(j)
(k)
(l)
S40RTScr2 0.48
S40RTScr1 0.51
S40RTS+litho 0.49
SAW642ANcr2 0.49
SAW642ANcr1 0.50
SAW642AN+litho 0.47
3D2018_S40RTScr2 0.49
3D2018_S40RTScr1 0.51
3D2018_S40RTS+litho 0.48
S2.9_S362cr2 0.48
S2.9_S362cr1 0.51
S2.9_S362+litho 0.48
South Caspian
Turkmenistan
Alborz
NW Iran
Central Iranian Blocks
Afghan block
CF
MZT
SSZ
UDMA
MZF
RRF
MFF
Persian Gulf
MSZ
Gulf of Oman
Mesopotamian Foreland Basin
Zagros
Kopeh Dagh
Arabia
0.0 0.1 0.2 0.3 0.4 0.5 0.6 0.7 0.8 0.9 1.0 2.0 3.0

Figure 12:

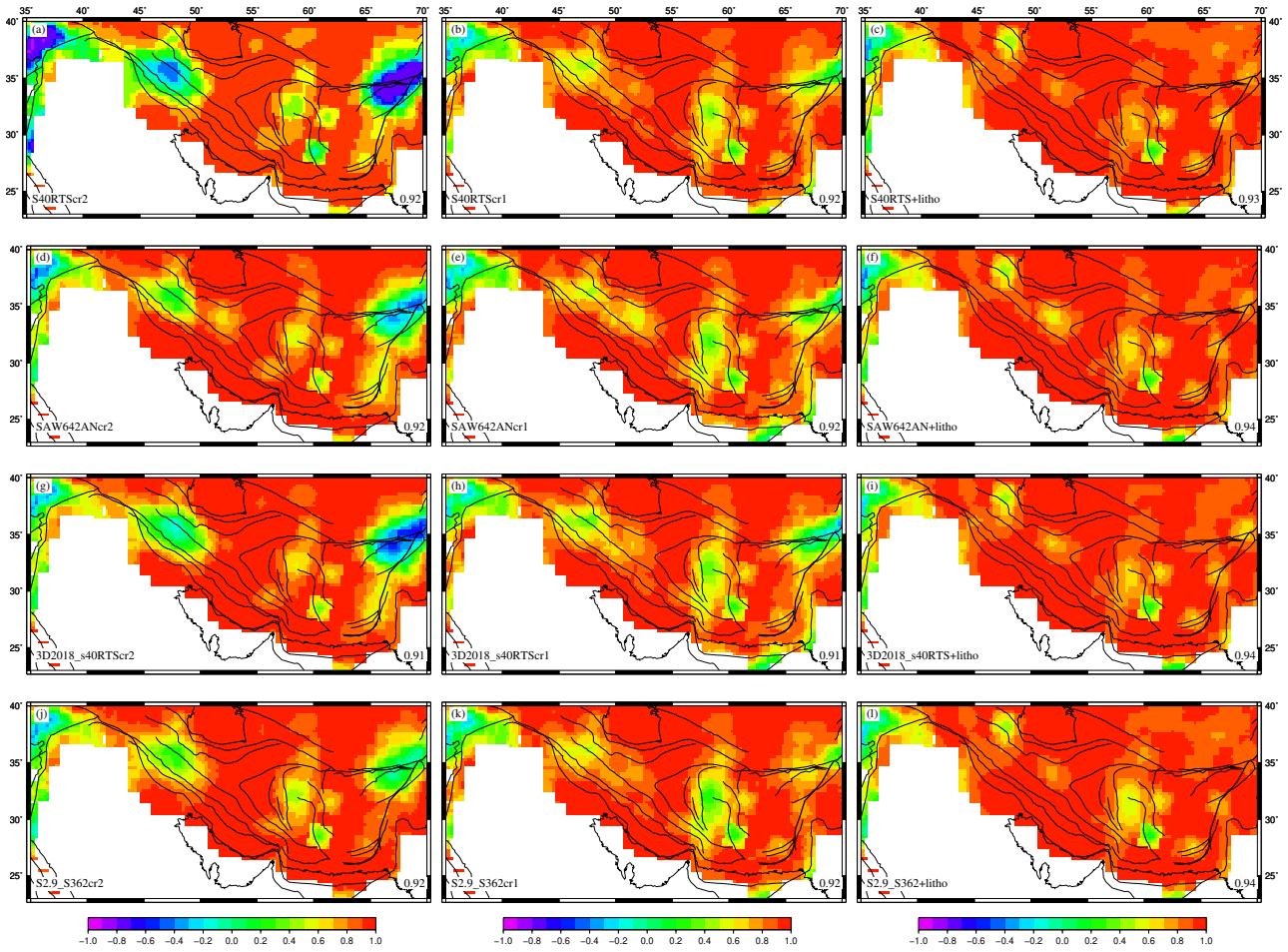
(a)
S40RTScr2
0.92
(b)
S40RTScr1
0.92
(c)
S40RTS+litho
0.93
(d)
SAW642ANcr2
0.92
(e)
SAW642ANcr1
0.92
(f)
SAW642AN+litho
0.94
(g)
3D2018_s40RTScr2
0.91
(h)
3D2018_s40RTScr1
0.91
(i)
3D2018_s40RTS+litho
0.94
(j)
S2.9_S362cr2
0.92
(k)
S2.9_S362cr1
0.92
(l)
S2.9_S362+litho
0.94
−1.0 −0.8 −0.6 −0.4 −0.2 0.0 0.2 0.4 0.6 0.8 1.0

Figure 13:

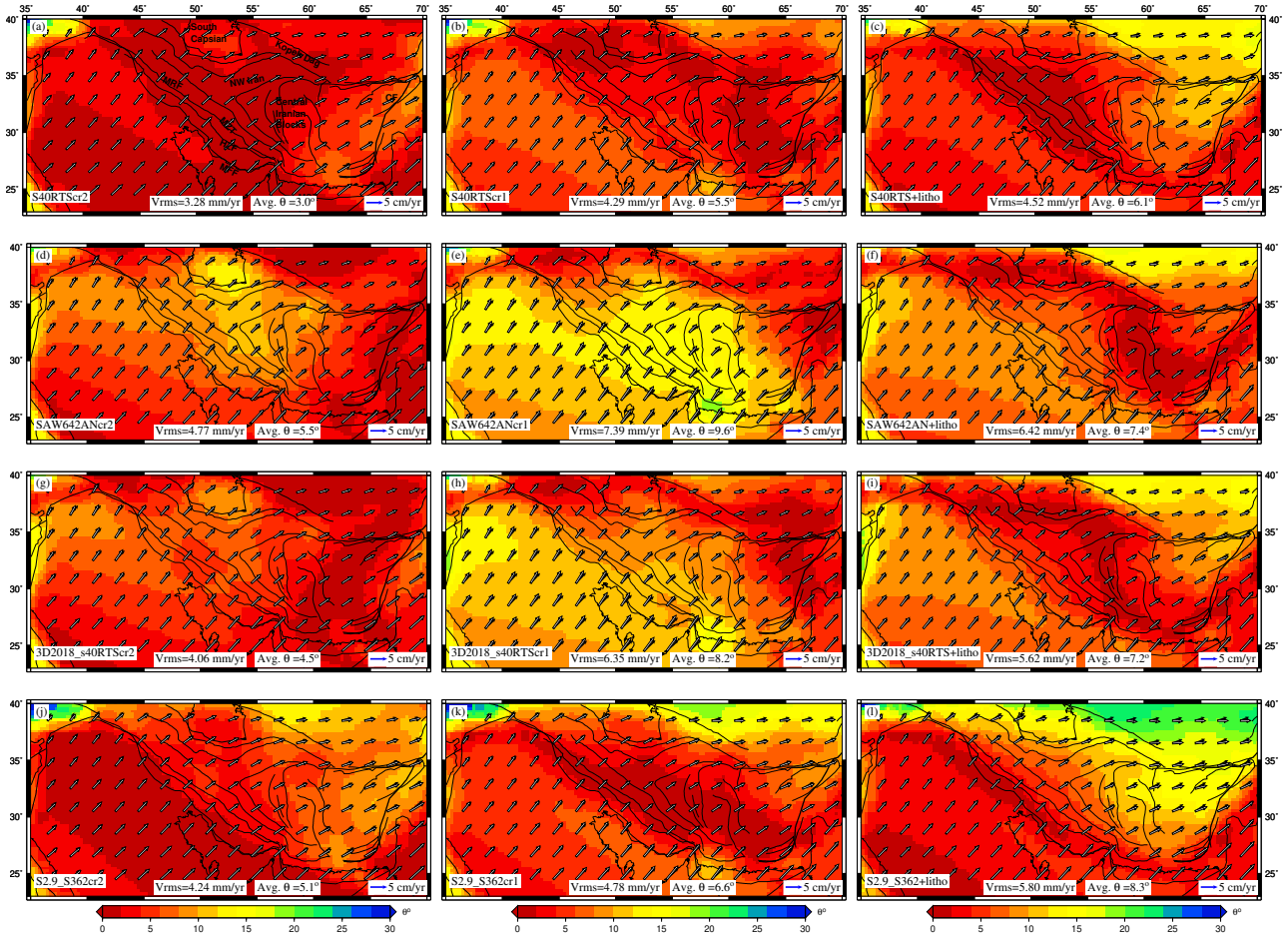
(a)
South Caspian
Tarim
NW Iran
Central Iranian Blocks
CF
S40RTScr2
Vrms=3.28 mm/yr
Avg. θ =3.0°
5 cm/yr
(b)
S40RTScr1
Vrms=4.29 mm/yr
Avg. θ =5.5°
5 cm/yr
(c)
S40RTS+litho
Vrms=4.52 mm/yr
Avg. θ =6.1°
5 cm/yr
(d)
SAW642ANcr2
Vrms=4.77 mm/yr
Avg. θ =5.5°
5 cm/yr
(e)
SAW642ANcr1
Vrms=7.39 mm/yr
Avg. θ =9.6°
5 cm/yr
(f)
SAW642AN+litho
Vrms=6.42 mm/yr
Avg. θ =7.4°
5 cm/yr
(g)
3D2018_s40RTScr2
Vrms=4.06 mm/yr
Avg. θ =4.5°
5 cm/yr
(h)
3D2018_s40RTScr1
Vrms=6.35 mm/yr
Avg. θ =8.2°
5 cm/yr
(i)
3D2018_s40RTS+litho
Vrms=5.62 mm/yr
Avg. θ =7.2°
5 cm/yr
(j)
S2.9_S362cr2
Vrms=4.24 mm/yr
Avg. θ =5.1°
5 cm/yr
(k)
S2.9_S362cr1
Vrms=4.78 mm/yr
Avg. θ =6.6°
5 cm/yr
(l)
S2.9_S362+litho
Vrms=5.80 mm/yr
Avg. θ =8.3°
5 cm/yr
θ°
0 5 10 15 20 25 30

Figure 14:

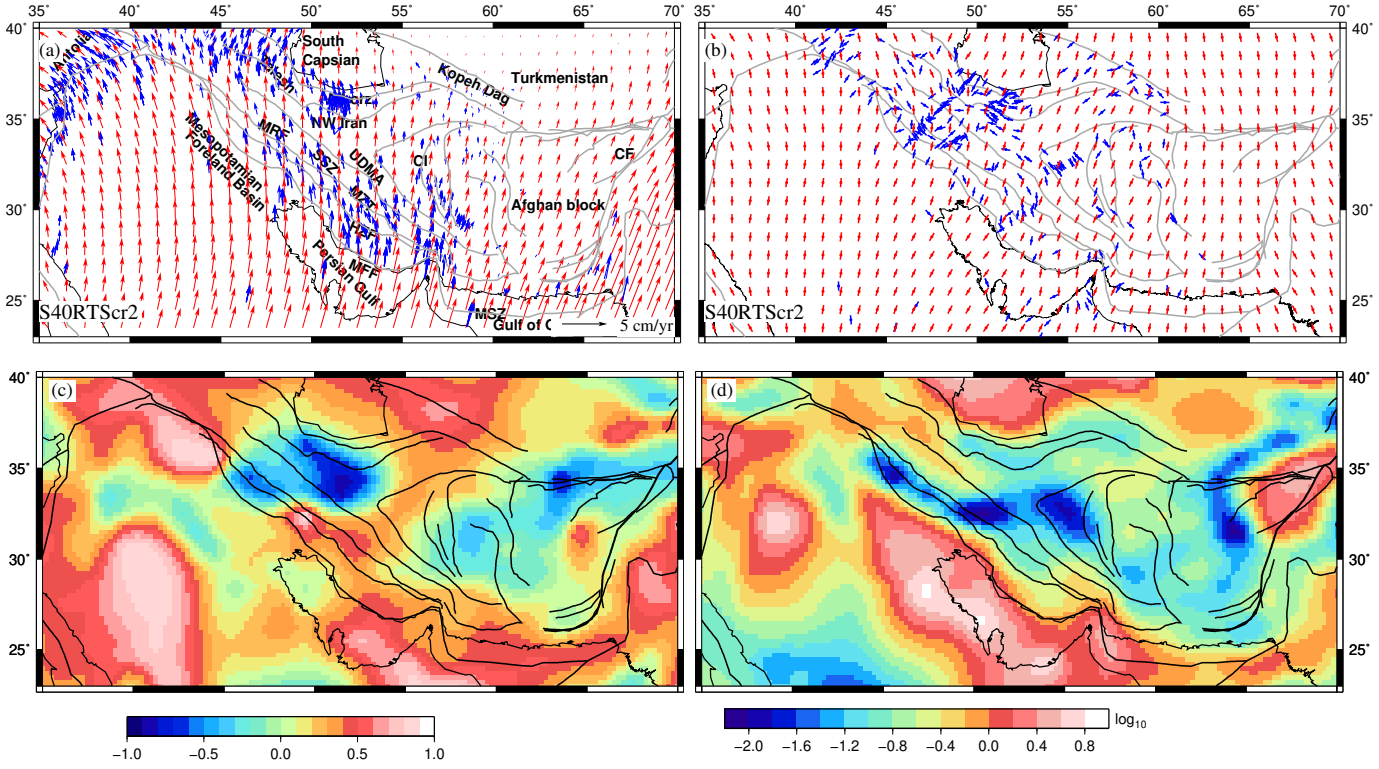
(a)
(b)
(c)
(d)
S40RTScr2
S40RTScr2
South Capsian
Turkmenistan
Kopeh Dag
NW Iran
MRF
SSZ
DDMA
CI
CF
Afghan block
MFF
Persian Gulf
MSZ
Mesopotamian Foreland Basin
5 cm/yr
−1.0 −0.5 0.0 0.5 1.0
−2.0 −1.6 −1.2 −0.8 −0.4 0.0 0.4 0.8
log10

Figure S1:

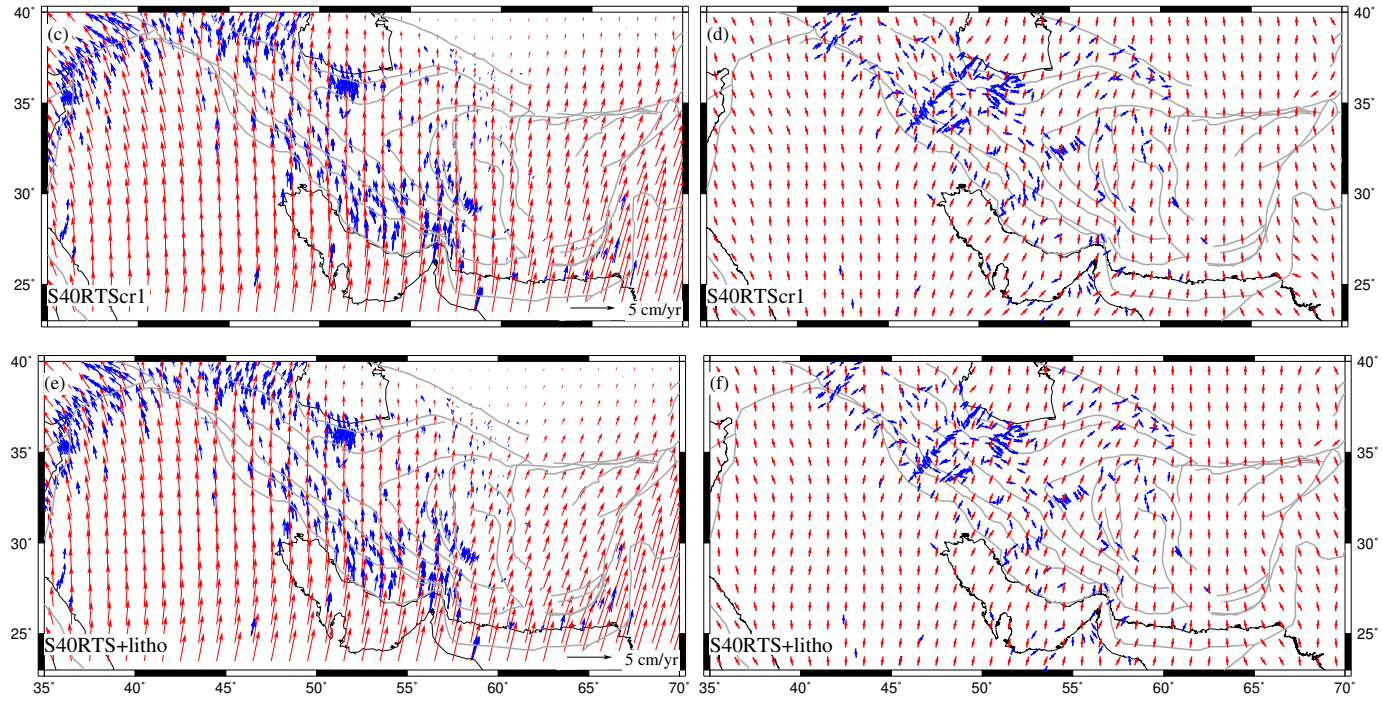
(c)
S40RTScr1
5 cm/yr
(d)
S40RTScr1
(e)
S40RTS+litho
5 cm/yr
(f)
S40RTS+litho
40˚
35˚
30˚
25˚
35˚
40˚
45˚
50˚
55˚
60˚
65˚
70˚

Figure S2: